

**Evaluation of Oscillatory
Velocities Measured by a Triple
Axis Coherent Doppler Velocity
Profiler (CDVP) in the Delta
Flume 2001 Experiment**

**B.D. Moate, P.S. Bell
and P.D. Thorne**

September 2007



Contents

<i>Section</i>	<i>Page</i>
1 Introduction	1
2 Background, data processing, and modelling	2
2.1 Experimental overview	2
2.2 Operating principles of the 3-axis CDVP	3
2.3 Influences on near-bed recorded velocities	4
2.3.1 Bed location	4
2.3.2 Thickness of the wave bottom boundary layer	5
2.3.3 Comparison of sampling volume sizes	6
2.4 Pre-processing of recorded velocities	7
2.4.1 Despiking	7
2.4.2 Rotation	8
2.5 Modelling Root Mean Square (RMS) velocities	9
3 Results	11
3.1 Bed height and thickness of the wave bottom boundary layer	11
3.2 Detected velocity spikes	11
3.3 Comparison of modelled and measured RMS velocities	12
3.3.1 ECMs	12
3.3.2 ADVs	12
3.3.3 CDVP	13
3.4 Comparison of velocity series in the time and frequency domains	15
3.4.1 Comparison of CDVP with ADV velocities	15
3.4.2 Comparison of CDVP with ECM velocities	16
3.5 Affect of suspended sediment concentrations on CDVP performance	18
4 Discussion, and classification of CDVP flume test records	20
5 Conclusions	22
6 Acknowledgements	23
7 References	23
8 Tables	25
9 Figures	32

1 Introduction

Acoustic instrumentation has been increasingly used to measure the velocity components of hydrodynamic flows over the last 2 decades (Christensen, 1983; Zedel *et al*, 1996; Voulgaris and Trowbridge, 1998; Zedel and Hay, 2002; Betteridge *et al*, 2005). One of the main advantages of acoustic instruments over other measurement techniques, is the ability to non-intrusively measure all three velocity components. A trade-off exists however, between the two dominant types of acoustic instruments available, with Acoustic Doppler Current Profilers (ADCPs) providing simultaneous spatial profiles of non-located velocities, and with Acoustic Doppler Velocimeters (ADV) providing collocated velocities though with no profiling capability. Recently, the concept of bi-static triple axis acoustic profiling instruments has been realised, which have the potential to bridge the gap between ADCPs and ADVs, enabling simultaneous collocated profiles of all three velocity components to be measured non-intrusively, at both high spatial and temporal resolution (Zedel and Hay, 2002; Betteridge *et al*, 2003; Betteridge *et al*, 2005). Such measurements are suitable for studying turbulent velocities at centimetric resolution in the near-bed zone, and are therefore of interest in turbulence and sediment transport studies.

The purpose of this report is to provide an assessment of the reliability of the velocities recorded by a prototype triple axis Coherent Doppler Velocity Profiler (CDVP) during a series of controlled tests in the Delft Hydraulics Delta flume in 2001. Whilst a field evaluation of the capability of the CDVP was reported by Betteridge *et al* (2006 and 2005), some disagreement between velocities measured by the CDVP and those measured by two nearby ADVs was observed, and further assessment of the CDVP is therefore required. In addition, since the hydrodynamic and sedimentary conditions encountered in a single field study are unlikely to enclose the full range that may be experienced in coastal waters, the present study provides an extension of the previous CDVP evaluation. The main objective of this report was to clearly classify the CDVP velocities from each flume test as either relatively reliable (Category A), problematic (Category B) or unreliable (Category C).

2 Background, data processing, and modelling

2.1 Experimental overview

The large size of the Delta flume (230 m long, 5 m wide, 7 m deep) provides a controllable environment in which numerous hydrodynamic and sediment transport processes can be simulated at full scale, i.e. on spatial scales comparable to those encountered in coastal and estuarine environments (Williams *et al*, 2003). During the Delta flume 2001 tests, two different sediment beds were subjected to a range of surface wave conditions, with significant wave height gradually incremented from small (~ 0.3 m) to large (~ 1.8 m) back to small waves, to enable the evolution of bed forms to be assessed under purely oscillatory flows (see Bell and Williams, 2002). The two sediment beds differed in their particle size distribution, with one bed consisting of fine sand ($d_{50} = 0.221$ mm) and the second of medium sand ($d_{50} = 0.349$ mm). Thus, both sediment beds studied in the Delta flume tests were considerably finer than those encountered in the field evaluation study ($d_{50} = 1.2$ mm) reported by Betteridge *et al* (2006).

Velocities in the Delta flume were recorded at intra-wave timescales using two ADVs, a vertical array of 5 Electromagnetic Current Meters (ECMs), and the prototype 3-axis CDVP. The CDVP and ADVs recorded at 16 Hz, whilst the ECMs recorded at 25 Hz, and all ECM records reported here were resampled at 16Hz to enable comparison with the ADVs and CDVP. The two ADVs deployed were a Nortek ADV and a Nortek Vector ADV, and are hitherto referred to as ADV-1 and ADV-2 respectively. Both the CDVP and ADV-1 were mounted on a movable trolley attached to the instrument frame, whilst ADV-2 was just mounted on the instrument frame. ADV-2 included a temperature and pressure sensor, though the software automatically converted the measured pressures to depth using an unknown atmospheric pressure. A Druck 3 bar pressure sensor was mounted on the movable trolley, with a second located in the instrument shed to monitor atmospheric pressure. Other instruments deployed during the flume tests included a LISST, an Acoustic Backscatter System (ABS), three Wave staffs, a ripple profiler and a pump sampler for the collection of water samples. The relative positions of all instruments deployed in the flume are provided in Tables 1 to 4, with an annotated photograph of the frame presented in Figure 1.

In total, coincident time series were obtained for 61 separate tests in the Delta flume 2001 experiments (26 over the fine sand bed, and 35 over the medium sand bed). Each flume test was assigned a name constructed according to the sand bed in use (F for fine, M for medium), a sequential wave height number, and the run number for that wave height (e.g. F12-2). In this report, to simplify presentation of the evolution of parameters across flume tests, an alternative numerically unique flume test index is at times used. A mapping between the flume test names and the unique flume test indexes is provided in Table 5.

2.2 Operating principles of the 3-axis CDVP

The CDVP comprised of a transceiver aligned with the vertical axis, and two passive receivers directed at the sampling volume insonified by the transceiver. The CDVP operates on the principle that the sound emitted is backscattered, primarily by suspended sediments within the water column, and any motion in the sediments relative to the receivers causes a Doppler frequency shift in the returned signal. The Doppler frequency shift, f_D , is obtained from the rate of change of the phase of consecutive backscattered signals (Betteridge *et al*, 2006):

$$f_D = \frac{\Psi}{2\pi T} \quad (1)$$

with

$$\Psi = \left[\frac{\langle I(t)Q(t+T) - I(t+T)Q(t) \rangle}{\langle Q(t)Q(t+T) + I(t)I(t+T) \rangle} \right] \quad (2)$$

where T is the time delay between emitted pulses, $I(t)$ and $Q(t)$ are the in-phase and quadrature components of the received signal at time t , and $\langle \rangle$ represents an average over a number of consecutive pulses. The radial velocity of the scattering particles is found from:

$$v_d = \frac{c \times f_D}{2 \times f_0} \quad (3)$$

where c is the speed of sound in water and f_0 is the transmitted frequency (524 KHz). Thus, it is assumed that the average velocity of the particles within the sampling volume is a representative proxy for the velocity of the flow in which the particles are suspended.

To ensure measured velocities are non-ambiguous, the backscattered signal from a given scatterer must be received before the next acoustic ping is transmitted. The maximum unambiguous Doppler frequency shift is $\leq 0.5f_{PRF}$ (Thorne and Hanes, 2002), where f_{PRF} is the pulse repetition frequency, or the inverse of the time between consecutive pings. Hence, from Equation 3 the maximum unambiguous velocity that can be measured is a function of f_{PRF} , being 0.36 ms^{-1} for f_0 defined as above, c equal to the speed of sound in water ($\sim 1500 \text{ ms}^{-1}$) and a pulse repetition frequency of 512 Hz. By using two interleaved pulse repetition frequencies of 409.6 and 512 Hz, the maximum theoretical unambiguous velocity measurable is increased by approximately a factor of four (Betteridge *et al*, 2006), thus increasing the range of oceanographic applications for which the CDVP may be used. The radial velocities measured by the CDVP can be resolved into the orthogonal components u

(streamwise), v (crosswise) and w (vertical). The downward pointing transceiver measures the w component directly, and with w known, the measured signal by the two passive receivers can be used to derive u and v .

Acoustic instruments that rely on the backscattered signal from a suspension of scatterers are subject to a number of sources of noise (Voulgaris and Trowbridge, 1998). Doppler phase noise causes a broadening of the Doppler spectral peak, which introduces errors in the estimated radial velocities. Sources of Doppler phase noise include the residence time of particles within the sampling volume, with some particles leaving and others entering between successive acoustic pings. Particle residence time noise is proportional to the ratio of the mean velocity and the size of the sampling volume, with noise increasing as the sample volume decreases. Doppler phase noise can also be caused by beam divergence, which is dependent upon the bi-static angle between the transducer/receiver assemblage. Other potentially significant sources of measurement uncertainties include variations in total velocity due to velocity distributions, micro-scale turbulence, and velocity gradients within theinsonified sampling volume, though the later is typically only important close to the boundary layer. An additional source of measurement uncertainty exists due to the ability of the sensor to resolve the phase of the backscattered acoustic pings, and is dependent upon the velocity range of the instrument. For ADVs however, this source of noise was found to be relatively small, being of the order of only a few mms^{-1} (Voulgaris and Trowbridge, 1998). Zedel and Hay (2002) reported measurement uncertainties of 1 % and 5 % in the vertical and streamwise velocities respectively for a bi-static triple axis Doppler system (similar to the POL CDVP) deployed in a tow-tank. These errors were largely attributed however to flow disturbance and inaccuracies in the exact instrument geometry.

2.3 Influences on near-bed recorded velocities

2.3.1 Bed location

As the aim of the Delta flume 2001 experiments was to verify and quantify sediment transport processes in the near-bed zone (Bell and Williams, 2002), it was considered likely that the location of the bed could change both during and across individual flume runs, or equivalently, that the frame could sink into the bed under large waves. Consequently, as some sampling volumes were located close to the initial position of the (initially flat) flume bed (see Tables 1 to 4), the reliability of the measurements obtained from the near bed locations was considered at risk due to the potential evolution of the bed, which could bury or adversely affect these sampling locations. The distance between each sampling volume and the flume bed boundary, d_B , was therefore determined for all instruments for each flume test.

To obtain d_B , the mean position of the flume bed relative to the feet of the instrument frame ($\overline{d_F}$) was calculated for each flume test using the strong bed echo recorded by the ABS. In addition to $\overline{d_F}$ however, migration of ripple bed forms could cause the actual bed location to be one ripple amplitude ($\overline{r_A}$) higher for (on average) half of the duration of each flume test, which could therefore also significantly affect velocity records. Hence, d_B was calculated for each sampling volume as:

$$d_B = P_{SV} - (\overline{d_F} + \overline{r_A}) \quad (4)$$

where P_{SV} was the position of the each instruments sampling volume relative to the feet of the instrument frame (see Tables 1 to 4).

2.3.2 Thickness of the wave bottom boundary layer

As velocities recorded within the wave bottom boundary layer could theoretically include turbulent velocities, and therefore significantly depart from velocities predicted by linear wave theory, the positions of instrument sampling volumes relative to the wave bottom boundary layer (WBBL) was also determined. The thickness of the WBBL (δ_w) was calculated for rippled beds under oscillatory only flow, using the method outlined in Davies and Villaret (1999). Briefly, δ_w was modelled as:

$$\delta_w = 5 \times \sqrt{\frac{K_0}{\omega}} \quad (5)$$

where $\omega = 2\pi/T$, with T the wave period, and K_0 was twice the mean convective eddy viscosity. K_0 was calculated using:

$$K_0 = 0.008U_0k_S \text{ where } A_0 / k_S < 2.5 \quad (6a)$$

or,
$$K_0 = 0.00506U_0k_S \sqrt{A_0 / k_S} \text{ where } A_0 / k_S > 2.5 \quad (6b)$$

where U_0 was the wave orbital amplitude near the bed, A_0 was the wave orbital excursion amplitude near the bed ($=U_0/\omega$), and k_S was the equivalent roughness of the bed. U_0 was calculated as (Soulsby, 1997):

$$U_0 = \frac{a_w \omega}{\sinh(kh)} \quad (7)$$

where a_w was the wave amplitude, k the wavenumber ($= 2\pi/\lambda$, with λ the wavelength) and h the total water column depth. The wavenumber was obtained by solving the dispersion equation (see Section 2.5). The equivalent roughness was calculated using the expression:

$$k_S = 25 \times \eta \times \left(\frac{\eta}{\lambda_R} \right) \quad (8)$$

where η was the ripple height, and λ_R the ripple wavelength. To provide an estimate of the mean δ_w for each flume test, the peak wave period and $a_w = \frac{1}{2}H_S$ (with H_S the significant wave height) for each flume test were used in Equation 7.

2.3.3 Comparison of sampling volume sizes

As the size of a velocimeters sampling volume (S_V) can affect both the resolution and accuracy of the velocities measured (see Section 2.2), the sampling volumes of each velocimeter deployed in the Delta flume tests were quantified. For near bed recorded velocities, particle residence time noise (which increases with decreasing S_V), noise due to micro-scale turbulence within the sampling volume (which increases with increasing S_V), and velocity shear within the sampling volume (which increases with increasing S_V) are all potentially significant sources of measurement uncertainties (Voulgaris and Trowbridge, 1998). As ECM current meters measure the EM force induced by water flow through the instruments magnetic field, ECM measurements may also be affected by noise due to micro-scale turbulence and velocity shear within the instruments sampling volume, though would be unaffected by particle residence times.

The sampling volume of the Delft Hydraulics ECMs was quoted to be 6 cm in diameter in the vertical-streamwise plane, and 1 cm thick in the crosswise plane. Hence, assuming a disc shaped sampling volume, each ECM sampling volume was $\sim 28 \text{ cm}^3$. The sampling volume of ADV-2 was quoted by the manufacturer to be 1.5 cm diameter in the crosswise-streamwise plane, with the (user selectable) sampling volume height set to 0.4 cm in the vertical plane. Again, assuming a disc shaped sampling volume, this would correspond to $\sim 0.7 \text{ cm}^3$. No information was available on the sampling volume size of ADV-1, though as ADV-1 was an earlier model of ADV-2, it was expected to be fairly similar.

The sampling volume dimensions of each CDVP bin in the crosswise-streamwise plane were calculated from the beam divergence of the downward pointing vertical transducer, derived from the transducers beam pattern (presented in Figure 2). The beam divergence was calculated as the angle from the normal to the face of the transducer (i.e. 0° in the beam pattern) for which the beam directivity had fallen to -3 dB, being 2.75° . The diameter of the

sampling volume for each bin was obtained from the tangent of the beam divergence (2.75°) multiplied by the distance of the bin from the transducer face, and is presented in Table 3. The height of the CDVP sampling volumes was the same for all bins, being 4.6 cm in the vertical plane. Hence the equivalent volume of each CDVP sampling volume also varied between bins, and is also presented in Table 3.

2.4 Pre-processing of recorded velocities

2.4.1 Despiking

Time series of the raw measured velocities from all three instruments revealed the presence of numerous spurious data spikes in many records. Spikes were identified using the phase-space thresholding method of Goring and Nikora (2002), with identified spikes being replaced by linear interpolation. The phase-space thresholding method identifies spikes as those points which lie outside of an ellipsoid in three dimensional phase-space, with the three dimensions of phase-space consisting of a given velocity component (v) along with its first (\dot{v}) and second (\ddot{v}) time derivatives. Thus, identification of spikes for a given velocity component (u , v , or w) was independent of the other orthogonal components. The boundaries of the ellipsoid in each dimension of phase-space for a given velocity component were calculated as the product of the standard deviation (σ) of the velocity component in that phase-space dimension and the Universal maximum, λ_{UM} :

$$\lambda_{UM} = \sqrt{2 \text{Log}_e(n)} \quad (9)$$

with n the number of data points in the record. Thus, the ellipsoid in the v - \ddot{v} plane was given by:

$$1 = \frac{v}{\lambda_{UM} \sigma_v} + \frac{\ddot{v}}{\lambda_{UM} \sigma_{\ddot{v}}} \quad (10)$$

Following identification and replacement of spikes, the standard deviation of the modified record was thereby reduced, and successive iterations of the phase-space thresholding method therefore resulted in increasingly cleaner records. Only a finite number of iterations of the phase-space thresholding method were made in the present study, as some values replaced by linear interpolation can themselves be identified as spikes using this method, and therefore successive iterations do not remove such spikes (Goring and Nikora, 2002). Here, 8 iterations were observed to reduce the number of spikes to a constant small level in even the spikiest records.

2.4.2 Rotation

To correct the despiked current velocities for any miss-alignment of the sensors relative to the direction of main flow, measured velocities were rotated to be aligned with the principle axes of variance. The angle of the principle axes to the measured velocities, θ_p , was calculated from (Emery and Thomson, 1997):

$$\mathcal{G}_p = \frac{1}{2} \tan^{-1} \left[\frac{2\overline{v'_1 v'_2}}{\overline{v'^2_1 - v'^2_2}} \right] \quad (11)$$

where overbars denote the record mean, and v'_1 and v'_2 were two orthogonal components of fluctuating velocity (e.g. u' and w'). Fluctuating velocity was defined as the difference between the measured velocity at time t , and the record mean for that component:

$$v'(t) = v(t) - \bar{v} \quad (12)$$

The measured velocities were thus rotated by the angle θ_p via the transformation matrix (Emery and Thomson, 1997):

$$\begin{pmatrix} v_{1r} \\ v_{2r} \end{pmatrix} = \begin{pmatrix} \cos \mathcal{G}_p & \sin \mathcal{G}_p \\ -\sin \mathcal{G}_p & \cos \mathcal{G}_p \end{pmatrix} \begin{pmatrix} v_1 \\ v_2 \end{pmatrix} \quad (13)$$

where the r subscript denotes a rotated velocity component. All components of measured velocity were rotated following Equations 11 – 13 by obtaining θ_p for each Cartesian axis. Thus for the ADVs, u and v were rotated around the z axis producing u_{r1} and v_{r1} , u_{r1} and w were rotated around the y axis producing u_{r2} and w_{r1} , and v_{r1} and w_{r1} were rotated around the x axis producing v_{r2} and w_{r2} . The final rotated velocities were therefore u_{r2} , v_{r2} and w_{r2} . For the ECMs, no crosswise component of flow was measured, and hence u and w were rotated around the y axis producing u_{r1} and w_{r1} , being the final rotated velocities for the ECMs. Figure 3 shows the results of this procedure for an ECM record obtained 0.5 m above the bed during Delta flume test M09-1.

For the CDVP, rotation of the recorded velocities was less straight forward, for two reasons. Firstly, the close proximity of the lower CDVP bins to the flume bed could cause the principle angle of variance to be aligned in a local direction, perhaps dictated by bedforms, rather than being aligned in the along flume direction. Consequently, all CDVP bins were

rotated by a common angle, derived by finding the mean angle to the principle axis of variance from the first 6 bins only (ranging from 77.7 – 46.6 cm above the feet of the frame, see Table 3). Secondly, whilst the CDVP was designed to measure all three orthogonal velocity components, and should hence be rotated following the same method as applied to the ADVs, extensive ambiguity was present in the crosswise v velocity component. This ambiguity was un-correctable, and attempts to remove it using the phase-space thresholding despiking method (Section 2.4.1) were unsuccessful. The v velocity ambiguity problem is illustrated for one flume test in Figure 4, which shows a comparison between v velocities measured by the CDVP and ADV-2. The exact cause of this ambiguity was unknown, though it was likely due to either the misalignment of one of the side receivers during setup, or electronic failure (Paul Bell, personnel communication). Hence, *only the streamwise (u) and vertical (w) velocity components are hitherto reported*, and were rotated with the crosswise v velocity component excluded, thus following the same method as described for the ECMs.

2.5 Modelling Root Mean Square (RMS) velocities

RMS velocities were modelled at the location of each ECM and ADV sampling volume, and for each CDVP bin, using the surface elevations obtained by the wave staff positioned directly above the instrument frame (wave staff 3). The power spectral density (PSD) for a given wave frequency (f) present in the surface elevation record was used to obtain the square of the wave amplitude (a) for that wave, and the square of the velocity amplitudes for that wave were modelled as:

$$u^2 = a^2 \omega^2 \left[\frac{\cosh(k(h+z))}{\sinh(kh)} \right]^2 \quad (14a)$$

and

$$w^2 = a^2 \omega^2 \left[\frac{\sinh(k(h+z))}{\sinh(kh)} \right]^2 \quad (14b)$$

where h was the water column depth, z was the vertical position of the instrument sample volume or bin (with $z = 0$ corresponding to the mean water level), and all other symbols are as previously defined. As it was possible for the instrument frame to sink into the bed, or for bed deposition to occur locally under the instrument frame, h and z were calculated for each flume test for all frame instruments and CDVP bins. The total water column depth, h , was calculated as the sum of the depth below the ABS transducers plus the depth above the

Druck pressure sensor, accounting for the relative positions of each instrument. To obtain the depth from the ABS, it was assumed that each ABS bin corresponded to a 1 cm vertical element of the water column. To convert recorded pressures into depths, the temperature from ADV-2 was used to calculate the density of the water assuming a salinity of 0 PSU. This assumed no significant vertical gradient in temperature existed between the location of the ADV-2 temperature sensor and all other instruments. z was calculated as the depth above each instrument with the total water column depth subtracted. At the ECM locations, no instrumentation was present to provide measurements of either h or z , and therefore a constant water depth of 4.06 m was used (being the mean initial depth recorded for the first four flume tests for both fine and medium sand), along with the initial measured positions of each ECM above the bed (see Table 2). The wavenumber k for each wave frequency was found iteratively from the dispersion equation, using the Newton-Raphson method:

$$k_i = k_{i-1} - \frac{((\omega^2) - gk_{i-1} \tanh(k_{i-1}h))}{((-g \tan(k_{i-1}h)) - [(gk_{i-1}h) / \cosh^2(k_{i-1}h)])} \quad (15)$$

where g was the gravitational constant ($= 9.81 \text{ ms}^{-2}$), and the initial guess of k was taken from the deep water approximation ($k = \omega^2/g$). The RMS velocities were taken as the square root of the frequency mean of the squared velocities:

$$u_{RMS} = \sqrt{\langle u^2 \rangle} \quad (16a)$$

and

$$w_{RMS} = \sqrt{\langle w^2 \rangle} \quad (16b)$$

where u_{RMS} and w_{RMS} were the RMS u and w velocities respectively.

3 Results

3.1 Bed height and thickness of the wave bottom boundary layer

The calculated d_B for the sampling volumes of ADV-1 and CDVP Bins 4 – 15 are presented as a function of flume test index in Figure 5. Table 5 provides a mapping between flume test names and the flume test index used in Figure 5. Figure 5 shows that for all flume tests, the sampling volume of CDVP Bin 15 was located either in, or too close to the bed (i.e. within 5 cm of the bed). Similarly, Figure 5 shows the sampling volumes of CDVP Bins 9 – 14 were also located either in or too close to the bed for numerous flume tests. CDVP velocities from all effected bins were excluded from further analysis. The sampling volume of ADV-1 was located either in, or too close to the bed (in the 5 and 9 cm above bed region, see the Nortek[®] ADV User Manual) for flume tests F06-1 – F16-2 and M07-1 – M17-2. Hence, ADV-1 velocities from these flume tests were also excluded from further analysis. The sampling volume for ADV-2 overlapped with that of CDVP Bin-4, and is therefore not presented in Figure 5 for clarity.

The mean thickness of the WBBL obtained using Equations 5 – 8 is also presented in Figure 5 for each flume test. For flume tests not excluded above, the sampling volume of ADV-1 fell within or sufficiently close to the WBBL for flume tests M05-1 – M06-2. CDVP Bins 4 – 14 fell within (or very close) to the WBBL for numerous non-excluded flume tests, particularly Bins 8 – 14 for tests M07-2 – M14-2 (see Figure 5). It should be noted however, that Davies and Villaret (1999) cast some doubt on the validity of Equation 8, suggesting the proportionality factor may be ~ 3 times bigger than quoted. Such an increase in k_S would cause the calculated δ_w to increase by a factor of 1.31 – 1.73 compared to those presented in Figure 5. This would result in the sampling volume of ADV-1 being within the WBBL for the additional flume tests F05-1 and M04-1 – M04-2.

3.2 Detected velocity spikes

An example comparison between a raw and despiked velocity record obtained from the CDVP is provided in Figure 6. The mean number of spikes detected across all flume tests are presented in Figure 7, for each velocity component and for each instrument, as a function of height above the feet of the instrument frame. Figure 7 shows the mean number of spikes detected was greatest for the CDVP and least for the ECMs, for all velocity components. As the number of detected spikes was large for some velocity records, records for which more than 10 % of the record consisted of spikes were excluded from further analysis. It should be noted that by imposing this threshold, no velocity records from either ADV-1, ADV-2 or the ECMs were excluded, beyond those already outlined in Section 3.1.

3.3 Comparison of modelled and measured RMS velocities

As the trolley chain broke during test M10-1, and as the wave generator was switched off after 16 minutes, all comparisons exclude this flume test. Following refilling of the flume after test M10-1, all 3 Wave-staffs experienced technical problems, and only 20 minutes of reliable wave data was recorded by Wave-staff 3 during M10-2. No wave data was obtained from the Wave-staffs for flume tests M10-3 – M11-2, and therefore all comparisons between measured and modelled RMS velocities exclude these flume tests.

3.3.1 ECMs

Comparisons between the modelled and measured RMS u and w velocities are presented for the ECMs in Figures 8 and 9 respectively. Overall, close agreement was evident between the modelled and measured u and w velocities, though some disagreement in w was apparent for ECMs 1 and 2 (Figure 9 (a) and (b)). Whilst it is conceivable that the source of this disagreement was due to non-linear effects in the near-bed region, it is likely that at least some of the disagreement was simply due to modelling uncertainties. The main modelling uncertainties were the absolute water column depth and the vertical positions of each ECM. Both absolute water column depth and ECM vertical position had the potential to change during and between flume tests, due to either the build up or erosion of the bed beneath the ECMs, or due to wave induced movement of the ECM heads. It should be noted that the position of the ECM heads was known to be effected by the surface waves, with the ECM extension arms being severely bent during the fine sand bed tests (see Figure 10). Figure 10 shows that ECMs 1, 2 and 3 were most susceptible to wave induced movement of the heads, with ECMs 4 and 5 being undamaged. As no bed detection instrumentation or pressure sensors were located at the ECM locations, no direct measurement of water depth or instrument position was available during individual flume tests. Quantitatively however, a 2 cm uncertainty in the vertical position of ECM-1 would cause an ~10 % change in the modelled RMS w velocities at this location. The RMS differences between the modelled and measured RMS velocities, for each ECM and velocity component, are presented in Table 6.

3.3.2 ADVs

Figure 11 presents a comparison between modelled and measured RMS u velocities for both ADV-1 and ADV-2. Figure 11 shows measured RMS u velocities were in close agreement to modelled values for both ADVs, over all flume tests. Similarly, a comparison between modelled and measured RMS w velocities is presented in Figure 12 for both ADVs. For ADV-1, Figure 12 (a) shows significant disagreement existed between modelled and measured RMS w velocities recorded inside the WBBL, with reasonable agreement between

modelled and measured RMS w velocities recorded outside the WBBL. The significant departure of measured RMS w velocities from modelled values within the WBBL could be due to turbulence, with power spectra derived from ADVs supporting this hypothesis (see Section 3.4.1). For ADV-2, Figure 12 (b) shows close agreement between modelled and measured RMS w velocities for the majority of fine and medium sand flume tests. For flume tests M10-1 – M17-2, poor agreement was observed between the modelled and measured RMS w velocities. As the ADV-2 measured velocities for these flume tests showed no obvious faults, and as for the majority of these flume tests the sampling volume of ADV-2 was located outside the WBBL (see Section 3.1), the source of this disagreement was attributed to the breakage of the trolley chain in flume test M10-1. Whilst ADV-2 was not located on the trolley, it is possible that ADV-2 was damaged when the trolley chain broke, or that one of the other instruments on the trolley used to model the RMS velocities was offset vertically (such as the pressure sensor, or ABS) when the trolley chain was replaced. The RMS differences between the modelled and measured RMS velocities for both ADVs and velocity components are presented in Table 6.

3.3.3 CDVP

Figure 13 presents a comparison between modelled and measured RMS u velocities derived from CDVP Bins 1 – 14 (Bin 15 was located within or too close to the bed for all flume tests, see Section 3.1). The RMS velocities presented in Figure 13 were divided into three groups: those that were in close agreement to modelled values, those which were obtained from locations within the wave-bottom-boundary-layer, and those that showed more than a 4 cms^{-1} disagreement with modelled values. The limit of 4 cms^{-1} was \sim twice the RMS difference between modelled and measured RMS u velocities achieved by ADV-2 (see Table 6). Setting an acceptable RMS difference between modelled and CDVP measured RMS velocities that was twice that achieved by ADV-2 was considered reasonable, since measurement errors due to velocity distributions and gradients within sampling volumes scale with the size of the sampling volume (see Section 2.2). Figure 13 shows that for many flume tests, poor agreement was observed between modelled and measured RMS u velocities, with measured RMS u velocities typically being underestimated relative to modelled values. The number of flume tests for which close agreement was observed, decreased as the height of the sampling volume above the bed decreased (i.e. as bin number increased). In the highest bins (Bins 1 – 5), \sim 20 flume tests showed close agreement with modelled RMS velocities, whilst in the lowest bins (Bins 11 – 14), typically only half a dozen flume tests showed close agreement. Where the sampling volume was located within the wave-bottom-boundary-layer, measured RMS u velocities were underestimated relative

to the modelled values for the majority of flume tests. Such behaviour may reasonably be expected in the presence of significant bed forms (such as large ripples or sand waves) which could impede the near-bed velocities relative to those predicted from linear wave theory.

A comparison between modelled and measured RMS w velocities derived from Bins 1 – 14 (Figure 14) showed similar features to those described for RMS u velocities, with the number of flume tests for which measured RMS w velocities were in close agreement to the modelled velocities decreasing with decreasing sample volume height above the bed. For the w component of velocity, a 0.6 cm s^{-1} limit was imposed as an acceptable disagreement between modelled and measured RMS w velocities. Again, this limit was \sim twice the RMS difference between modelled and measured RMS w velocities achieved by ADV-2 (Table 6). In contrast to RMS u velocities, where the sampling volume was located within the wave-bottom-boundary-layer, measured RMS w velocities were overestimated relative to modelled values (in agreement with the trend observed for ADV-1), further suggesting the presence of turbulent velocities within the WBBL.

Table 7 presents a bin-by-bin summary of the most complete CDVP profiles from the Delta flume 2001 experiments, according to the comparisons between modelled and measured RMS velocities. The 13 flume tests presented in Table 7 showed close agreement between modelled and measured velocities, for both u and w components, for multiple bins within the CDVP profile, allowing for disagreement within the WBBL. All flume tests *not* present in Table 7 showed poor agreement between modelled and measured RMS velocity, for one or both velocity components, *over the majority of the acoustic profile*, and were therefore considered unreliable, of little use to turbulence and sediment transport studies, and were therefore excluded from further analysis.

3.4 Comparison of velocity series in the time and frequency domains

Following identification of the most complete CDVP profiles (Section 3.3.3), the 16 Hz CDVP data for each flume test presented in Table 7 was compared with the ADVs and ECMs in the time and frequency domains.

3.4.1 Comparison of CDVP with ADV velocities

3.4.1.1 ADV-1

For the flume tests presented in Table 7, only Bin-12 of test M06-2 overlapped with the vertical location of the sampling volume of ADV-1. For all other flume tests presented in Table 7, either the CDVP or ADV-1 velocity records had been discarded due to poor agreement between modelled and measured RMS velocities, due to the proximity of the bed, or due to excessive spiking in one or both records.

Figure 15 presents a comparison between CDVP Bin-12 and ADV-1 recorded velocities for M06-2, with a time series comparison presented in Figure 16. For the u velocity component, power spectra derived from CDVP Bin-12 and ADV-1 recorded velocities were in close agreement, particularly at frequencies below 0.3 Hz. At higher frequencies, more energy was observed by the CDVP than the ADV, with nearly an order of magnitude difference in the PSD at the nyquist frequency (8 Hz). The 16 Hz recorded velocities also showed good agreement for the u velocity component, with values scattered closely around the theoretical 1:1 line in Figure 15 (b), and with the time series for both instruments varying coherently (Figure 16 (a)). For the w velocity component, close agreement was observed in the power spectra above ~ 0.01 Hz, with the PSD of ADV-1 slightly elevated relative to that obtained from the CDVP between ~ 0.2 Hz and the nyquist frequency. Less agreement was observed in the 16 Hz w velocities however, with the time series obtained from the two instruments being generally incoherent, though with the magnitude of variability being similar. As the vertical locations of CDVP Bin-12 and ADV-1 were inside the WBBL for flume test M06-2 (see Table 7), the lack of agreement between the 16 Hz recorded velocities observed in Figures 15 (d) and 16 (b) could reasonably be expected, since w velocities would be strongly influenced by the local bedforms and turbulent velocities. Hence, as the sampling volumes of CDVP Bin-12 and ADV-1 were not collocated (separated laterally by 38 cm), and were not of equal size, differences in w velocities would be likely.

In accord with Kolmogorov's spectral model for the inertial sub-range, power spectra should decrease with $f^{5/3}$ when turbulent velocities are present (Williams *et al.*, 2003). Hence, to evaluate whether turbulent velocities were present in CDVP Bin-12 velocities, both u and w PSD were linearly regressed on $f^{5/3}$ for frequencies between 0.5 and 3 Hz (see Table 8). The relatively high R^2 values (> 0.6), and low p values (0.000) confirmed that

CDVP Bin-12 PSD did decrease with $f^{5/3}$, suggesting turbulent velocities were present in CDVP Bin-12 recorded velocities.

3.4.1.2 ADV-2

CDVP Bin-4 overlapped with the vertical location of the sampling volume of ADV-2 for all flume tests. Hence, Figures 17, 18 and 19 present comparisons between CDVP Bin-4 and ADV-2 power spectra, recorded velocities, and time series respectively, for each flume test presented in Table 7. Figure 17 shows considerable disagreement between ADV-2 and CDVP Bin-4 derived power spectra for flume tests F02-1, F03-1, F08-1 u , M02-2 and M15-1. Figure 19 shows that for the same flume tests (among others), significant disagreement between ADV-2 and CDVP Bin-4 derived time series was also observed, with the CDVP recorded velocities being either underestimated (e.g. F02-1 u), or considerably noisier (e.g. F02-1 w , F03-1 w , F06-1 w , M02-2 w , and M15-2 u) then those recorded by ADV-2. The scatter plots presented in Figure 18 generally showed good agreement between CDVP and ADV-2 recorded velocities, though noticeable disagreements were apparent for F02-1 u , F08-1 u and w , M02-2 w , and M15-1 u and w .

CDVP Bin-4 recorded velocities were in closest agreement to those recorded by ADV-2 for flume tests F05-1, M04-2, M06-1, M06-2, M07-1, M07-2, and M08-1, with excellent agreement for tests F05-1, M06-1, M06-2, M07-1 and M07-2. The sampling volumes for both CDVP Bin-4 and ADV-2 were located outside the predicted WBL for these flume tests (Figure 5 (b)), and hence turbulent velocities would not theoretically be expected in these velocity records. However, regression of the u and w PSD on $f^{5/3}$ for these flume tests again showed high R^2 and low p values (Table 8), suggesting turbulent velocities may be present.

3.4.2 Comparison of CDVP with ECM velocities

3.4.2.1 ECM-1

For the flume tests presented in Table 7, the sampling volume of ECM-1 overlapped with CDVP Bin-9 for F06-1, Bin-11 for M06-1 and M06-2, Bin-9 for M07-2 and M08-1, and Bin-7 for M15-2. The CDVP bin with which ECM-1 overlapped changed between flume tests due to the instrument frame sinking into the bed under the larger waves (see Figure 5). Figures 20, 21, and 22 present comparisons between CDVP and ECM-1 derived power spectra, recorded velocities, and time series respectively, for the flume tests listed above. Figure 20 shows that above 0.3 Hz, CDVP derived u power spectra were considerably elevated relative to those obtained from ECM-1 for all flume tests, with up to two orders of magnitude difference in the PSD at the nyquist frequency (8 Hz). In contrast, CDVP derived

w power spectra showed close agreement with those derived from ECM-1, though CDVP w power spectra for flume tests F06-1 and M15-1 were elevated above 3 Hz, with up to an order of magnitude difference at high frequencies. Comparison of CDVP recorded velocities with those from ECM-1 showed a broad degree of scattering for all flume tests (Figure 21). Figure 21 shows CDVP and ECM-1 u velocities were in reasonable agreement however, and the magnitude of variability observed in w velocities was also consistent between the CDVP and ECM-1. Figure 22 shows CDVP recorded time series were broadly in agreement with those obtained by ECM-1 for all flume tests, though all CDVP time series showed high frequency variations not recorded by ECM-1. High frequency velocity variations were particularly evident in F06-1 w , and M15-1 u and w CDVP time series. Figure 5 shows the vertical location of the CDVP bins for flume tests M06-1, M06-2, M07-2, M08-1 and M15-2 were all close to, or within the predicted WBBL thicknesses (δ_w and $1.31\delta_w$), and regression of CDVP PSD on $f^{5/3}$ showed relatively high R^2 values and low p values for all flume tests except M15-2 (Table 9). Whilst the source of the CDVP recorded high frequency velocity variations may have been turbulence, the vertical location of CDVP Bin-9 during flume test F06-1 (the power spectra of which also decayed with $f^{5/3}$) was not within nor close to the WBBL. Hence, if turbulent velocities truly were present in CDVP Bin-9 for flume test F06-1, it is possible they were generated by flow interactions with the instrument frame. Alternatively, it is possible that the high frequency velocity variations were due to instrument noise or malfunction.

3.4.2.2 ECM-2

The sampling volume of ECM-2 overlapped with CDVP Bin-5 for F02-1, F03-1, and F05-1, Bin-4 for F08-1, Bin-5 for M02-2 and M04-2, Bin-6 for M06-1 and M06-2, Bin-5 for M07-1, and Bin 4 for M07-2, M08-1 and M15-1. Figures 23, 24 and 25 present comparisons between CDVP and ECM-2 derived power spectra, recorded velocities, and time series respectively, for these 13 flume tests. Figure 23 shows CDVP power spectra were again elevated at frequencies greater than 0.4 Hz, relative to those recorded by the ECM. CDVP u power spectra were elevated by up to 3 orders of magnitude at the nyquist frequency (see Figure 23 (e), (i) and (u)), whilst w power spectra were typically elevated by 2 order of magnitude at the nyquist frequency. Figure 25 shows the cause of the elevated power spectra was again high frequency velocity variations, which were present in all CDVP recorded time series whilst being absent from those recorded by ECM-2. It should be noted that a phase lag existed between the CDVP and ECM-2 recorded time series for flume test F03-1 (Figure 25 (c)). This phase lag varied in magnitude across the time series, with ~ 1.2 s phase lag at 77 s, ~ 0.7 s phase lag at 969 s, and ~ 0.2 s at 1415 s. Comparison of CDVP

recorded velocities with those from ECM-2 again showed a broad degree of scattering for all flume tests (Figure 24), with u velocities showing reasonable agreement and the magnitude of variability observed in w velocities also being consistent between the CDVP and ECM-1. Figure 5 shows the vertical location of all CDVP bins overlapping with ECM-2 were far from the WBBL, and hence the high frequency variations were not theoretically attributable to turbulence. Regression of CDVP PSD on $f^{5/3}$ however again showed high R^2 and low p values (Table 9), suggesting the high frequency velocity variations may be turbulence.

3.5 Affect of suspended sediment concentrations on CDVP performance

Betteridge *et al* (2005) concluded that a minimum suspended sediment concentration of 0.01 gl^{-1} was required for the CDVP to obtain accurate velocity estimates in their shallow coastal inlet field site. The reason for the existence of a minimum concentration limit is due to backscattered acoustic signal strength being a function of concentration, and hence at concentrations below the stated limit, the signal to noise ratio may become too low to enable velocities to be measured accurately. Pump samples were collected during each Delta flume test at 5 near-bed heights (see Table 4), and subsequently analysed for suspended particulate matter concentrations. Whilst some fraction of the Delta flume SPM concentrations was attributable to organic acoustically non-reflective algae (Paul Bell, personnel communication), it is expected that the majority of near-bed SPM consisted chiefly of re-suspended inorganic bed sand, and SPM concentrations did not fall below 0.01 gl^{-1} for the vast majority of Delta flume tests (see Figure 26). As noted in Section 3.3.3 however, the vast majority of Delta flume tests showed poor agreement between modelled and CDVP derived RMS velocities.

This apparent inconsistency may be explained by the differences in particle size between the field site studied by Betteridge *et al* (2005 and 2006) and the fine and medium sands employed in the Delta flume. As mentioned in Section 2.1, the d_{50} grain size of bed material at the field site of Betteridge *et al* (2005 and 2006) was 1.2 mm, whilst the d_{50} grain sizes employed in the current tests were considerably finer, being 0.221 mm and 0.349 mm for the fine and medium sand tests respectively. For near-bed applications, the backscattered acoustic signal (V) observed by a transducer can be shown to be (Thorne and Hanes, 2002):

$$V \propto \frac{M^{1/2} f}{r\psi\sqrt{a_0\rho}} e^{-2r\alpha} \quad (17a)$$

with
$$\alpha = \frac{3\chi M}{4a_0\rho} \quad (17b)$$

where χ and f describe the scattering and backscattering characteristics of the particles in suspension, M is the mass concentration, ρ the density, ψ accounts for departure from spherical spreading, r is the range from the transducer and a_0 is the mean radius of particles in suspension. Hence, assuming that the mean radius of particles in suspension scales with the bed d_{50} , and that the density, scattering, and backscattering characteristics of the particles suspended in the delta flume and at the field site studied by Betteridge *et al* (2005 and 2006) were similar, Equation 17 can be solved to obtain the suspended mass concentrations (equivalent to 0.01 g l^{-1} at the field coastal inlet site) required for the CDVP to accurately measure velocities for the sands employed in the Delta flume tests. These concentration limits were calculated to be 0.182 and 0.051 g l^{-1} for the fine and medium sands respectively. Comparing Delta flume suspended concentrations to these concentration limits, Figure 26 shows that the majority of measured concentrations for all fine sand tests and medium sand tests M01-1 to M04-1, and M17-2 were below their respective concentration limits. This suggests the signal to noise ratio for these flume tests was likely below the threshold required for the CDVP to accurately measure velocity.

4 Discussion, and classification of CDVP flume test records

In the Delta flume, CDVP derived power spectra generally showed closer agreement to ECM and ADV derived power spectra for the w velocity component, with poorer agreement observed for the u component. In contrast, CDVP derived u time series and velocities generally showed closer agreement to ECM and ADV derived time series and velocities than was observed for w . Whilst apparently contradictory, this behaviour could reasonably be expected, due to the relative magnitudes of velocities originating from oscillatory flows, turbulence, and Doppler phase noise. For the u component, wave induced oscillatory velocities would typically be much larger than turbulent velocities or errors introduced by Doppler phase noise. Theoretically, the wave induced u velocities at the locations of the CDVP, ECMs and ADVs would be similar, with differences arising due solely to vertical and streamwise separations. For the w component however, the magnitude of wave induced oscillatory velocities in the bottom 1 m above the bed would be much more comparable to turbulent velocities and errors introduced by Doppler phase noise. Hence, as the CDVP, ADV, and ECM sampling volumes were not co-located, inter-instrument spatial de-correlation of the 16 Hz w (vertical) velocities would be probable, whilst much less discernable in the u (streamwise) velocities. Whilst spatial de-correlation may occur in the 16 Hz w velocities, it would still be likely that each instrument would see a similar level of energy at each frequency over the 25 minute flume test, as observed in the comparisons of the CDVP power spectra with those obtained from the ADVs and ECM-1.

Never-the-less, the above does not satisfactorily explain why the CDVP power spectra were elevated relative to those obtained by ADV-2 and ECM-1 for the u velocity component, and ECM-2 for both velocity components. It is worth noting however that the ECMs were not located on the instrument frame, being separated from the CDVP and ADVs by 1.25 m in the along flume, upstream direction (see Tables 1 and 3). Any turbulence generated by instrument frame flow disturbance would therefore not be seen by the ECMs (as they were upstream of the instrument frame), and instrument frame generated turbulence may also explain why CDVP power spectra showed a strong decay with $f^{5/3}$ at heights outside the wave-bottom-boundary-layer (see Section 3.4.1.3).

Instrument frame generated micro-scale turbulence (defined here as being turbulence over spatial scales less than or comparable to sampling volume sizes), may account for the elevation of CDVP derived u power spectra relative to those obtained from ADV-2, due to the difference in sampling volume size between these two instruments. The sampling volume of CDVP Bin-4 occupied $\sim 16 \text{ cm}^3$, being more than 20 times greater than the sampling volume of ADV-2 (0.7 cm^3). In the streamwise direction, the diameter of CDVP Bin-4 was ~ 2.5 times that of ADV-2, whilst in the vertical direction, the height of CDVP

Bin-4 was 11 times greater than that of ADV-2. Hence, the CDVP would be much more susceptible than ADV-2 to noise caused by micro-scale turbulence within the sampling volumes, since Doppler phase noise caused by micro-scale turbulence increases with increasing sample volume size (Voulgaris and Trowbridge, 1998). In contrast, particle residence time noise can be ruled out as being the cause of the elevated CDVP power spectra relative to those obtained from ADV-2, since particle residence time noise decreases as the sampling volume size increases. Velocity gradients within the CDVP sampling volume would also act to increase the noise floor of the CDVP relative to ADV-2, due to the CDVPs larger sampling volume size.

In the presence of instrument frame generated micro-scale turbulence, and due to the poor comparison of CDVP derived velocities compared to those from the ECMs, the validity of the 16 Hz CDVP profiles from any of the Delta flume tests presented in Table 7 may be doubtful. On the strength of the comparisons with the ADVs however, flume tests F05-1, M04-2, M06-1, M06-2, M07-1, M07-2 and M08-1 were classified as Category A (relatively reliable). From Figure 26, it is not surprising that these flume tests provided relatively reliable velocities, since SPM concentrations for these flume tests were above the minimum concentration limits for nearly all bins (with the exception of F05-1 Bin-6).

Similarly, due to the weakness of the comparisons with the ADVs, though considering their close agreement to the modelled RMS velocities, flume tests F02-1, F03-1, F06-1, F08-1, M02-2, and M15-1 were classified as Category B (problematic). Figures 17 – 25 suggest that reasonably reliable u velocity series could be recovered from these flume tests by filtering out velocities with frequencies > 0.5 Hz.

Due to the considerable disagreement between the measured and modelled RMS velocities, all remaining flume tests (being F04-1, F06-2 to F07-2, F08-2 to F16-2, M01-1 to M02-1, M03-1 to M04-1, M05-1, M05-2, M08-2 to M15-1 and M16-1 to M17-2) were classified as Category C (unreliable). Whilst the poor performance of the CDVP for the majority of fine sand tests and medium sand tests M01-1 to M04-1 and M17-2 can be explained by the low concentrations of SPM (see Section 3.5), the poor performance of the CDVP for flume tests M08-2 to M17-1 is unclear. For flume tests M10-1 and onwards (indexes 45 and up in Figure 26), it is possible that the trolley chain breakage caused miss-alignment of the CDVP transducers. A change in the quality of data obtained from ADV-2 after M10-1 (apparent in Figure 12 (b)) would lend support to this theory. One further possible source of disagreement could be transducer vibration under the larger waves (resulting in a loss of phase coherency). For sound of frequency 0.5 MHz, the in-water wavelength corresponds to ~ 3 mm, and hence a frame/transducer vibration of only 1 mm in amplitude would cause considerable loss of phase coherency.

5 Conclusions

The main findings of this evaluation are:

- The CDVP v component velocities showed numerous spurious data spikes (suggestive of aliasing) for all flume tests, which could not be removed using the phase space threshold despiking method of Goring and Nikora (2002).
- The RMS velocities measured by the 5 ECMs were in close agreement to those modelled using linear wave theory and surface elevation data from the wave staffs.
- The RMS u velocities measured by the ADVs were in close agreement to modelled values.
- The RMS w velocities measured by ADV-1 were typically overestimated relative to modelled values, though ADV-1 was located within or close to the predicted WBBL for all flume tests.
- The RMS w velocities measured by ADV-2 were in close agreement to modelled values for flume tests F02-1 to M10-1, and overestimated relative to modelled values for all flume tests after M10-1. It is possible that ADV-2 suffered an impact when the trolley chain broke (test M10-1).
- The RMS velocities measured by the CDVP generally showed poor agreement to modelled values, and SPM concentrations for most fine sand flume tests and medium sand flume tests M01-1 to M04-1 were below the minimum predicted concentration required for accurate CDVP velocity measurement.
- For the 13 most complete CDVP profiles (Table 7), CDVP derived power spectra, recorded velocities and time series showed close agreement to those derived from the ADVs for flume tests F05-1, M04-2, M06-1, M06-2, M07-1, M07-2, and M08-1, which were classified as Category A (relatively reliable). The remaining flume tests showed poor agreement between the CDVP and ADV-2 and were classified as Category B (problematic).
- All flume tests not present in Table 7 were classified as Category C (unreliable).
- SPM concentrations for all Category A flume tests were above the minimum predicted concentration levels required for accurate CDVP velocity measurement.
- For the 13 most complete CDVP profiles (Table 7), all CDVP derived u power spectra showed poor agreement to those derived from ECMs 1 and 2, being elevated at frequencies greater than ~ 0.3 Hz. CDVP derived w power spectra showed close agreement to those derived from ECM-1, though were elevated in comparison to those obtained from ECM-2.

6 Acknowledgements

This work was supported by the European HYDRALABIII project, and NERC UK as part of its small scale sediment process studies.

7 References

Bell, P.S. and Williams, J.J., 2002. Comprehensive measurement of sediment resuspension processes by waves at full scale. *POL Internal Document No. 143*.

Betteridge, K.F.E., Williams, J.J., Thorne, P.D. and Bell, P.S., 2003. Acoustic instrumentation for measuring near-bed sediment processes and hydrodynamics. *Journal of Experimental Marine Biology and Ecology*, 285, 105 – 118.

Betteridge, K.F.E., Bell, P.S., Thorne, P.D. and Williams, J.J., 2005. A Field Study Evaluation of the triple axis Coherent Doppler Velocity Profiler for measuring near bed flow. *POL Internal Document No. 177*.

Betteridge, K.F.E., Bell, P.S., Thorne, P.D. and Williams, J.J., 2006. Evaluation of a Triple-Axis Coherent Doppler Velocity Profiler for Measuring Near-Bed Flow: A Field Study. *Journal of Atmospheric and Oceanic Technology*, 23, 90 – 106.

Christensen, J.L., 1983. A new Acoustic Doppler Current Profiler. *Sea Technology*, 24(2), 10 – 13.

Davies, A.G. and Villaret, C., 1999. Eulerian drift induced by progressive waves above rippled and very rough beds. *Journal of Geophysical Research*, 104 (C1), 1465 – 1488.

Dean, R.G. and Dalrymple, R.A., 1992. Water Wave Mechanics for Engineers and Scientists. Advanced Series on Ocean Engineering – Volume 2. *World Scientific Publishing*, 353 pp.

Emery, W.J. and Thomson, R.E., 1997. Data Analysis Methods in Physical Oceanography, *Elsevier Science*, 638 pp.

Goring, D.G. and Nikora, V.I., (2002). Despiking Acoustic Doppler Velocimeter Data. *Journal of Hydraulic Engineering*, 128 (1), 117 – 126.

Soulsby, R., 1997. Dynamics of Marine Sands, *Thomas Telford*, 249 pp.

Thorne, P.D. and Hanes, D.M., 2002. A review of acoustic measurement of small-scale sediment processes. *Continental Shelf Research*, 22, 603 – 632.

Voulgaris, G. and Trowbridge, J.H., 1998. Evaluation of the Acoustic Doppler Velocimeter (ADV) for Turbulence Measurements. *Journal of Atmospheric and Oceanic Technology*, 15, 272 – 289.

Williams, J.J., Bell, P.S., Coates, L.E., Metje, N. and Selwyn, R., 2003. Interactions between a benthic tripod and waves on a sandy bed. *Continental Shelf Research*, 23, 355 – 375.

Zedel, L. and Hay, A.E., 2002. A Three Component Bistatic Coherent Doppler Velocity Profiler: Error Sensitivity and System Accuracy. *Journal of Ocean Engineering*, 27 (3), 717 – 725.

Zedel, L., Hay, A.E., Cabrera, R. and Lohrmann, A., 1996. Performance of a Single Beam Pulse-to-Pulse Coherent Doppler Profile. *Journal of Ocean Engineering*, 21 (3), 290 – 297.

8 Tables

Instrument/Sensors	X (cm)	Y (cm)	Z (cm)
ABS (1 MHz)		166	97
ABS (2 MHz)		161	97
ABS (4 MHz)		156	97
ADV-1 (Tests up to and including M10-1)		108	23 (14.5)
ADV-1 (Tests after M10-1)		108	32 (23.5)
ADV-2	200	84.5	72 (57)
CDVP Transducer	0	146	97
CDVP Receiver-1	-47	146	85.5
CDVP Receiver-2	0	197.5	85.5

Table 1 – Locations of ABS, ADVs, and the CDVP sensors on the instrument frame in the 2001 Delta flume tests (taken from Bell and Williams, 2002). X was oriented streamwise, and relative to the back of the instrument frame. Positive X was towards the wave generator. Y was oriented cross-flume, and relative to the outer-edge of the frame. Z was oriented vertically, and relative to the bottom of the feet of the frame. Numbers in brackets denote the location of the sampling volumes. All instruments were located on a moveable trolley, except ADV-2. The instrument frame was centred 125.5 m relative to the wave generator.

Instrument	X (m)	Y (cm)	Z (cm)
ECM-1	125.5	60	25
ECM-2	125.5	60	50
ECM-3	125.5	60	100
ECM-4	125.5	60	150
ECM-5	125.5	60	250

Table 2 – Locations of the ECMs in the 2001 Delta flume tests (taken from Bell and Williams, 2002). X was oriented streamwise and relative to the wave generator. Positive X was towards the wave generator. Y was relative to the opposite wall, Z was relative to the sand surface.

CDVP Bin	Height (cm)	S_D (cm)	S_V (cm ³)
1	77.7	1.9	4.0
2	70.5	2.5	7.5
3	64.0	3.2	11.6
4	57.9	3.8	16.2
5	52.1	4.3	21.4
6	46.6	4.8	27.0
7	41.2	5.4	33.0
8	36.0	5.9	39.5
9	30.8	6.4	46.5
10	25.8	6.8	53.8
11	20.8	7.3	61.6
12	15.9	7.8	69.8
13	11.1	8.3	78.3
14	6.3	8.7	87.3
15	1.5	9.2	96.8

Table 3 – CDVP bin heights, sampling volume diameter (S_D), and sampling volume (S_V). Heights apply to the centre of each bin, and are relative to the bottom of the feet of the frame.

Pump sampler	Height (cm)
1	12 (21)
2	16 (25)
3	24 (33)
4	40 (49)
5	72 (81)

Table 4 – Heights of pump sample nozzles above feet of instrument frame. Numbers in brackets denote heights for flume tests M10-2 and onwards.

Fine sand bed tests			Medium sand bed tests		
Test name	Test Index	Hs (m)	Test name	Test Index	Hs (m)
F02-1	1	0.37	M01-1	27	0.34
F03-1	2	0.50	M01-2	28	0.34
F04-1	3	0.64	M02-1	29	0.44
F05-1	4	0.83	M02-2	30	0.44
F06-1	5	1.02	M03-1	31	0.53
F06-2	6	1.04	M03-2	32	0.54
F07-1	7	1.23	M04-1	33	0.63
F07-2	8	1.24	M04-2	34	0.64
F08-1	9	1.42	M05-1	35	0.83
F08-2	10	1.44	M05-2	36	0.84
F09-1	11	1.34	M06-1	37	1.03
F09-2	12	1.34	M06-2	38	1.04
F10-1	13	1.24	M07-1	39	1.24
F10-2	14	1.25	M07-2	40	1.26
F11-1	15	1.14	M08-1	41	1.42
F11-2	16	1.15	M08-2	42	1.45
F12-1	17	1.04	M09-1	43	1.60
F12-2	18	1.04	M09-2	44	1.61
F13-1	19	0.84	M10-1	45	1.31
F13-2	20	0.84	M10-2	46	-
F14-1	21	0.63	M10-3	47	-
F14-2	22	0.64	M11-1	48	-
F15-1	23	0.45	M11-2	49	-
F15-2	24	0.46	M12-1	50	1.43
F16-1	25	0.34	M12-2	51	1.45
F16-2	26	0.35	M13-1	52	1.25
			M13-2	53	1.26
			M14-1	54	1.04
			M14-2	55	1.05
			M15-1	56	0.84
			M15-2	57	0.85
			M16-1	58	0.64
			M16-2	59	0.65
			M17-1	60	0.54
			M17-2	61	0.54

Table 5 – Mapping between flume test names and indexes, along with the measured significant wave height (from Wave-staff 3) for each test.

Instrument	u (cms⁻¹)	w (cms⁻¹)
ECM-1	1.16	0.41
ECM-2	0.84	0.51
ECM-3	0.82	0.32
ECM-4	0.87	0.43
ECM-5	0.94	0.94
ADV-1	1.67	1.04
ADV-2	1.94	0.30

Table 6 – RMS differences between modelled and measured RMS u and w velocities for each ECM and each ADV.

Bin	Flume test													
	F02-1	F03-1	F05-1	F06-1	F08-1	M02-2	M04-2	M06-1	M06-2	M07-1	M07-2	M08-1	M15-1	
1	√	√	√	√	×	√	×	√	×	√	√	√	×	
2	×	√	√	√	×	√	√	×	×	√	√	√	×	
3	×	√	√	√	√	√	√	√	√	√	√	√	√	
4	√	√	√	√	√	√	√	√	√	√	√	√	√	
5	√	√	√	×	√	√	√	√	√	×	√	√	×	
6	×	×	√	√	√	×	√	√	√	×	√	√	×	
7	×	×	×	×	×	×	√	√	√	×	√	×	√	
8	×	√	×	×	×	×	×	√	√	×	√	√	×	
9	×	√	×	√	×	×	×	√	√	×	√	BL	BL	
10	×	×	×	√	×	×	×	√	√	×	√	BL	BL	
11	√	√	×	√	BL	×	×	√	√	BL	BL	BL	B	
12	×	×	×	×	B	×	×	×	BL	BL	BL	B	B	
13	×	√	BL	BL	B	×	×	BL	BL	B	B	B	B	
14	×	BL	B	B	B	×	BL	BL	B	B	B	B	B	

Table 7 – Summary of the most complete CDVP profiles from the Delta flume 2001 experiments. Symbols denote: bins for which the RMS velocities for both u and w components showed close agreement to modelled values (√), bins for which one or both components showed poor agreement (×), bins located within the WBBL (BL), and bins located within the bed (B).

$PSD(CDVPBin) = (\alpha \times f^{-5/3}) + \beta$						
Flume test	CDVP Bin	Component	Slope	Intercept	R^2	p
M06-2	1	u	0.00146	0.000281	0.6086	0.000
M06-2	1	w	0.000071	0.000012	0.6661	0.000
F02-1	4	u	0.000078	0.000034	0.4942	0.000
F02-1	4	w	0.000014	0.000005	0.627	0.000
F03-1	4	u	0.000094	0.000037	0.5928	0.000
F03-1	4	w	0.000014	0.000004	0.575	0.000
F05-1	4	u	0.000546	-9.7E-05	0.5743	0.000
F05-1	4	w	0.000046	0.000005	0.661	0.000
F06-1	4	u	0.000633	0.000042	0.6574	0.000
F06-1	4	w	0.000121	0.000002	0.6718	0.000
F08-1	4	u	0.00476	-0.00098	0.7719	0.000
F08-1	4	w	0.000105	0.000022	0.6186	0.000
M02-2	4	u	0.000119	0.000057	0.5071	0.000
M02-2	4	w	0.000033	0.000006	0.6224	0.000
M04-2	4	u	0.000179	0.000037	0.5961	0.000
M04-2	4	w	0.00003	0.000005	0.6657	0.000
M06-1	4	u	0.00091	-0.00016	0.6287	0.000
M06-1	4	w	0.000072	0.000011	0.6505	0.000
M06-2	4	u	0.000815	-0.00013	0.6501	0.000
M06-2	4	w	0.000075	0.000009	0.6714	0.000
M07-1	4	u	0.000721	-3.6E-05	0.6913	0.000
M07-1	4	w	0.000116	0.000025	0.613	0.000
M07-2	4	u	0.001016	-7.6E-05	0.6722	0.000
M07-2	4	w	0.000126	0.000019	0.6587	0.000
M08-1	4	u	0.002598	-0.00059	0.6934	0.000
M08-1	4	w	0.000135	0.00002	0.6507	0.000
M15-1	4	u	0.001751	0.003503	0.2149	0.000
M15-1	4	w	0.000034	0.000012	0.5802	0.000

Table 8 – Summary of statistics from regressions of CDVP derived PSD on $f^{5/3}$, for CDVP bins overlapping with the vertical locations of the ADV sampling volumes.

$PSD(CDVPBin) = (\alpha \times f^{-5/3}) + \beta$						
Flume test	CDVP Bin	Component	Slope	Intercept	R^2	p
F06-1	9	<i>u</i>	0.000974	0.000256	0.5575	0.000
F06-1	9	<i>w</i>	0.000028	0.000004	0.6302	0.000
M06-1	11	<i>u</i>	0.000583	0.000127	0.6046	0.000
M06-1	11	<i>w</i>	0.000028	0.000007	0.6225	0
M06-2	11	<i>u</i>	0.00102	0.000182	0.644	0
M06-2	11	<i>w</i>	0.000041	0.000007	0.641	0
M07-2	9	<i>u</i>	0.001437	0.000039	0.6445	0
M07-2	9	<i>w</i>	0.000077	0.000007	0.6821	0
M08-1	9	<i>u</i>	0.001876	-0.00024	0.6572	0
M08-1	9	<i>w</i>	0.000063	0.000009	0.6412	0
M15-1	7	<i>u</i>	0.001922	0.002577	0.2893	0
M15-1	7	<i>w</i>	0.000031	0.000008	0.5931	0
F02-1	5	<i>u</i>	0.000181	0.000079	0.4769	0
F02-1	5	<i>w</i>	0.000008	0.000004	0.5114	0
F03-1	5	<i>u</i>	0.000097	0.000117	0.3371	0
F03-1	5	<i>w</i>	0.000012	0.000006	0.5501	0
F05-1	5	<i>u</i>	0.000507	-4.3E-05	0.6406	0
F05-1	5	<i>w</i>	0.000036	0.000003	0.6388	0
F08-1	4	<i>u</i>	0.00476	-0.00098	0.7719	0
F08-1	4	<i>w</i>	0.000105	0.000022	0.6186	0
M02-2	5	<i>u</i>	0.000211	0.000086	0.5452	0
M02-2	5	<i>w</i>	0.000019	0.000007	0.5499	0
M04-2	5	<i>u</i>	0.000192	0.000046	0.5749	0
M04-2	5	<i>w</i>	0.000026	0.000003	0.7037	0
M06-1	6	<i>u</i>	0.00112	-0.00017	0.6516	0
M06-1	6	<i>w</i>	0.000058	0.000009	0.6894	0
M06-2	6	<i>u</i>	0.001017	-9.9E-05	0.6697	0
M06-2	6	<i>w</i>	0.00006	0.000012	0.5995	0
M07-2	4	<i>u</i>	0.001016	-7.6E-05	0.6722	0
M07-2	4	<i>w</i>	0.000126	0.000019	0.6587	0
M08-1	4	<i>u</i>	0.002598	-0.00059	0.6934	0
M08-1	4	<i>w</i>	0.000135	0.00002	0.6507	0
M15-1	4	<i>u</i>	0.001751	0.003503	0.2149	0
M15-1	4	<i>w</i>	0.000034	0.000012	0.5802	0

Table 9 – Summary of statistics from regressions of CDVP derived PSD on $f^{5/3}$, for CDVP bins overlapping with the vertical locations of the ECM sampling volumes.

9 Figures

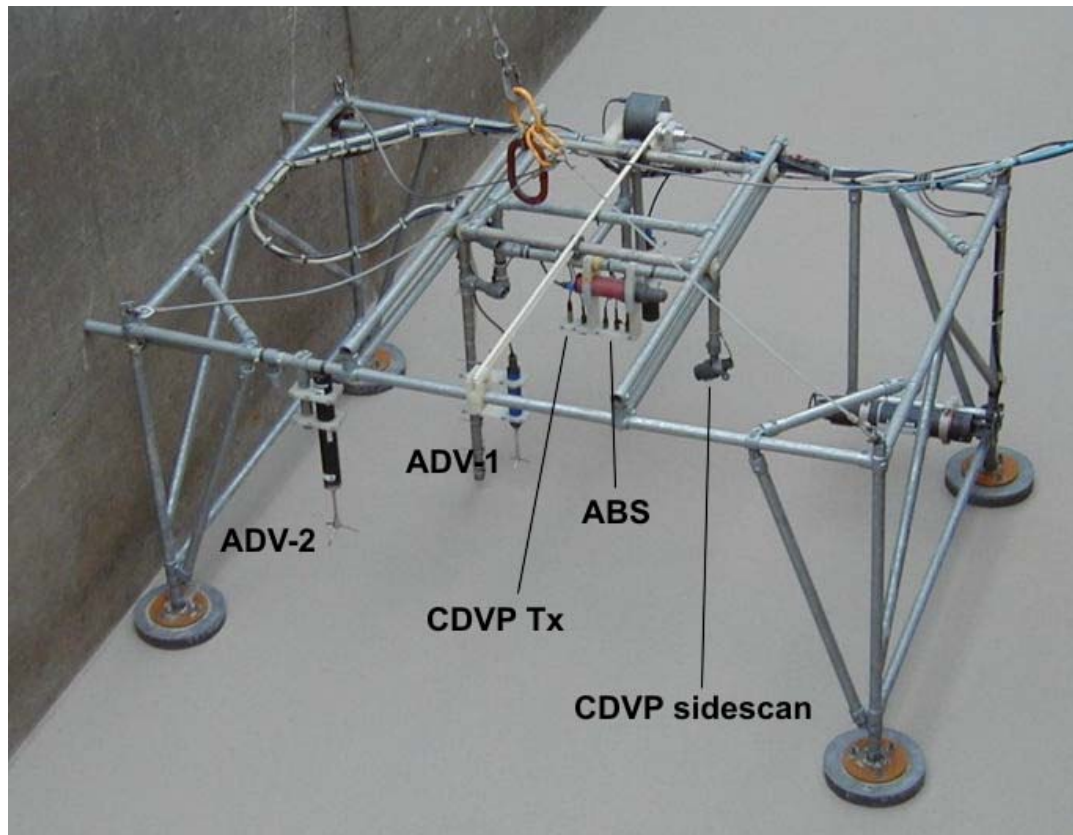


Figure 1 – Photograph of the instrument frame. The locations of instruments used in the present study are indicated.

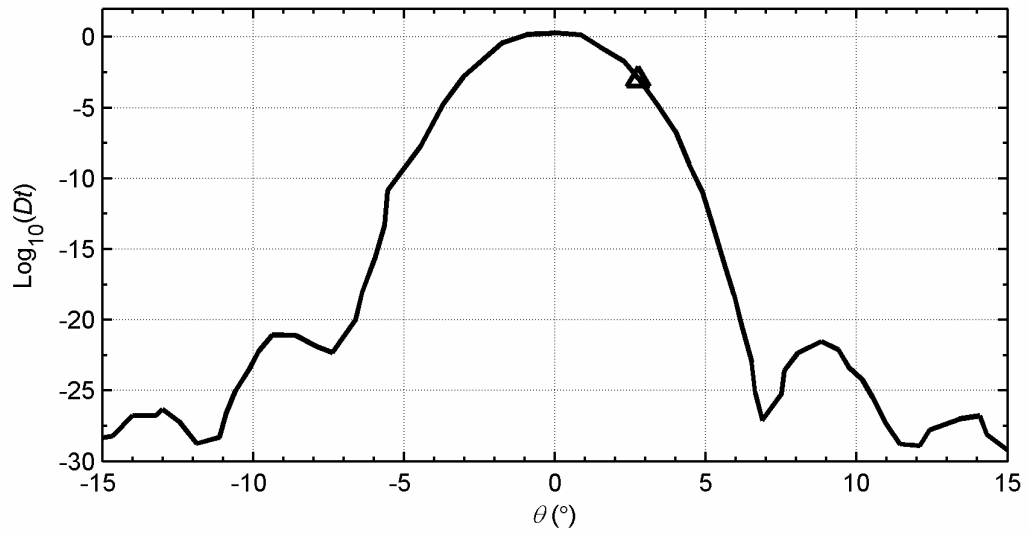


Figure 2 – Measured beam pattern for the vertical CDVP 524 KHz transducer (Transonics). The open triangle denotes the angle at -3 dB.

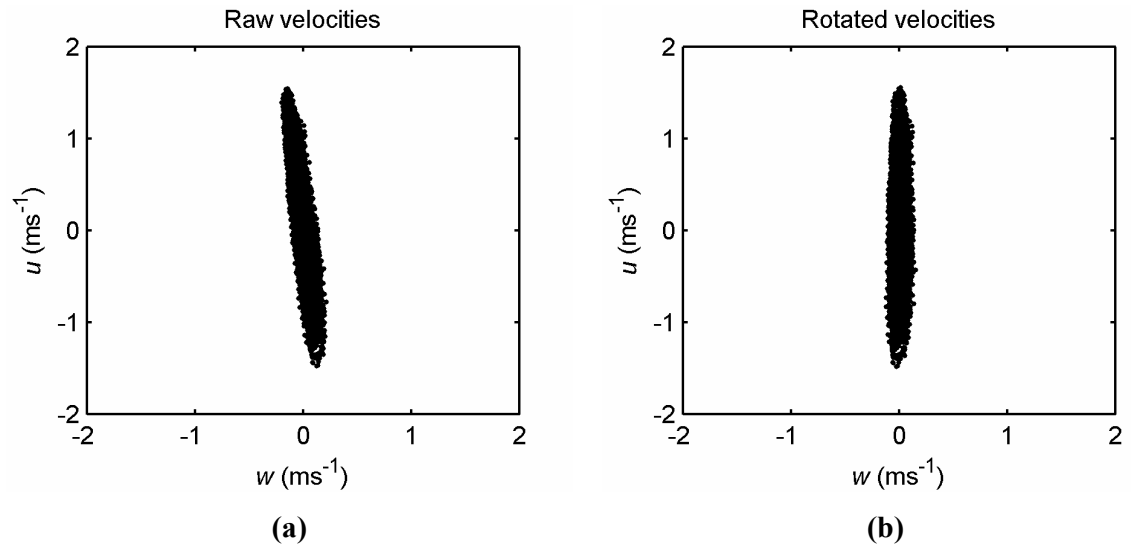


Figure 3 – Scatter plots of raw (a) and rotated (b) u and w velocity components derived from ECM-2 (0.5 m above the bed) during Delta flume test M09-1. The rotation angle around the z axis was calculated (using Equation 11) to be -5.8° .

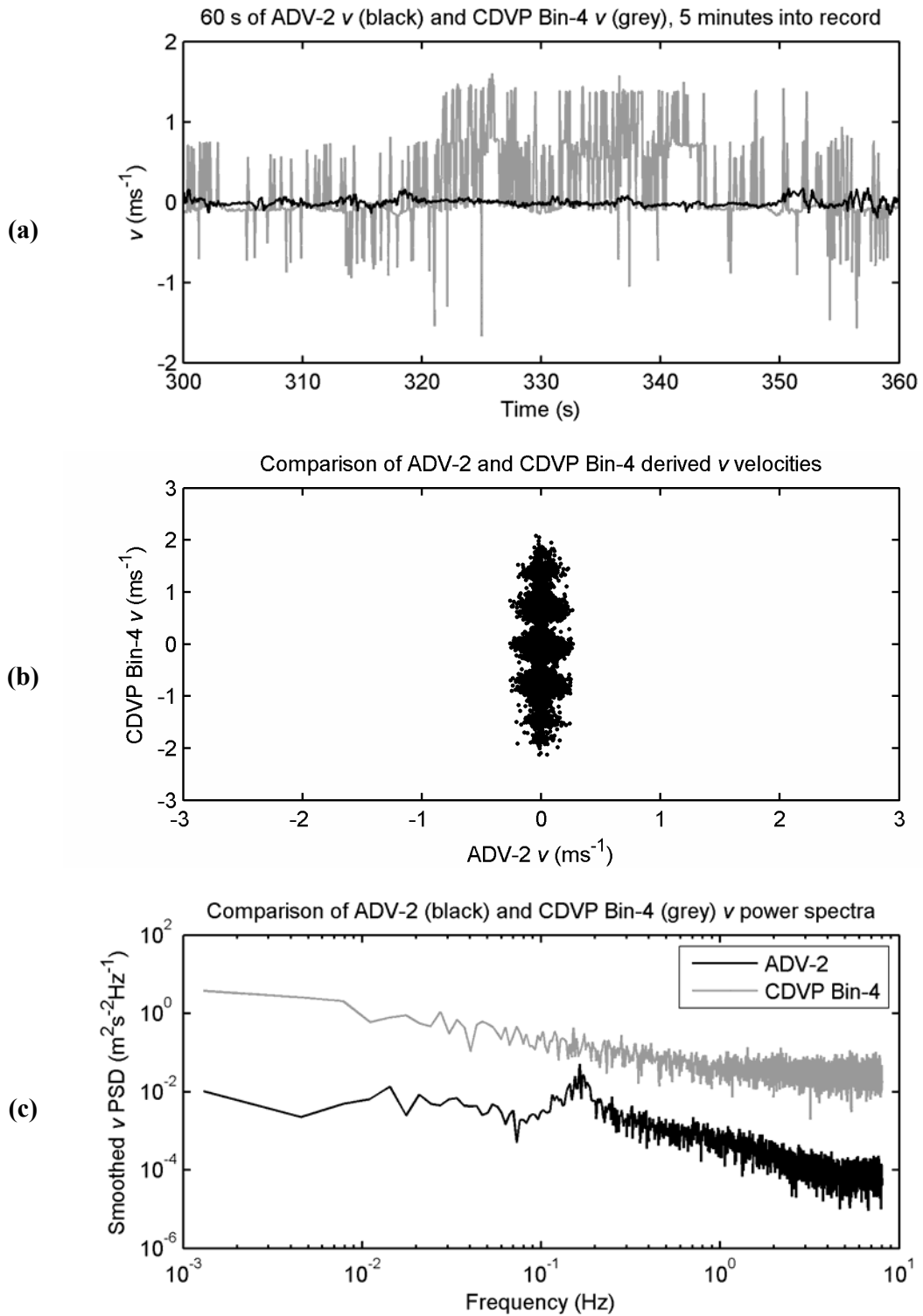


Figure 4 – Comparison of (a) time series (b) scatterplot and (c) power spectra of the v velocity component derived from ADV-2 and CDVP Bin-4 for Delta flume test M13-1. The considerable ambiguity present in the CDVP derived v velocities visible in (a) and (b) result in the CDVP PSD being two orders of magnitude greater than that observed by ADV-2 (c).

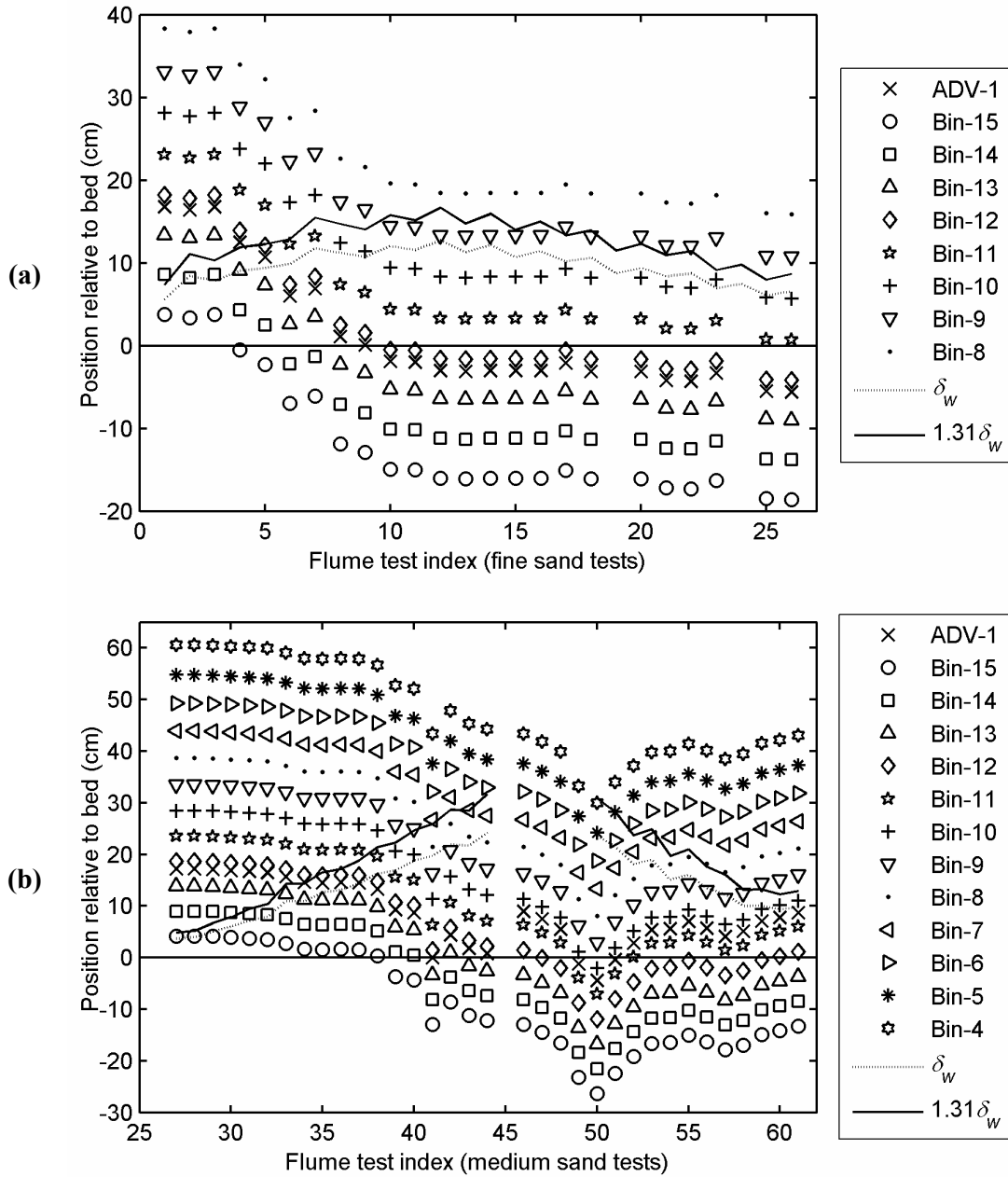


Figure 5 – Position of ADV-1 and CDVP sampling volumes, relative to the mean flume bed for (a) fine sand flume tests, and (b) medium sand flume tests. The dashed line depicts the thickness of the wave bottom boundary layer (δ_w), whilst the solid line depicts $1.31\delta_w$ (see text).

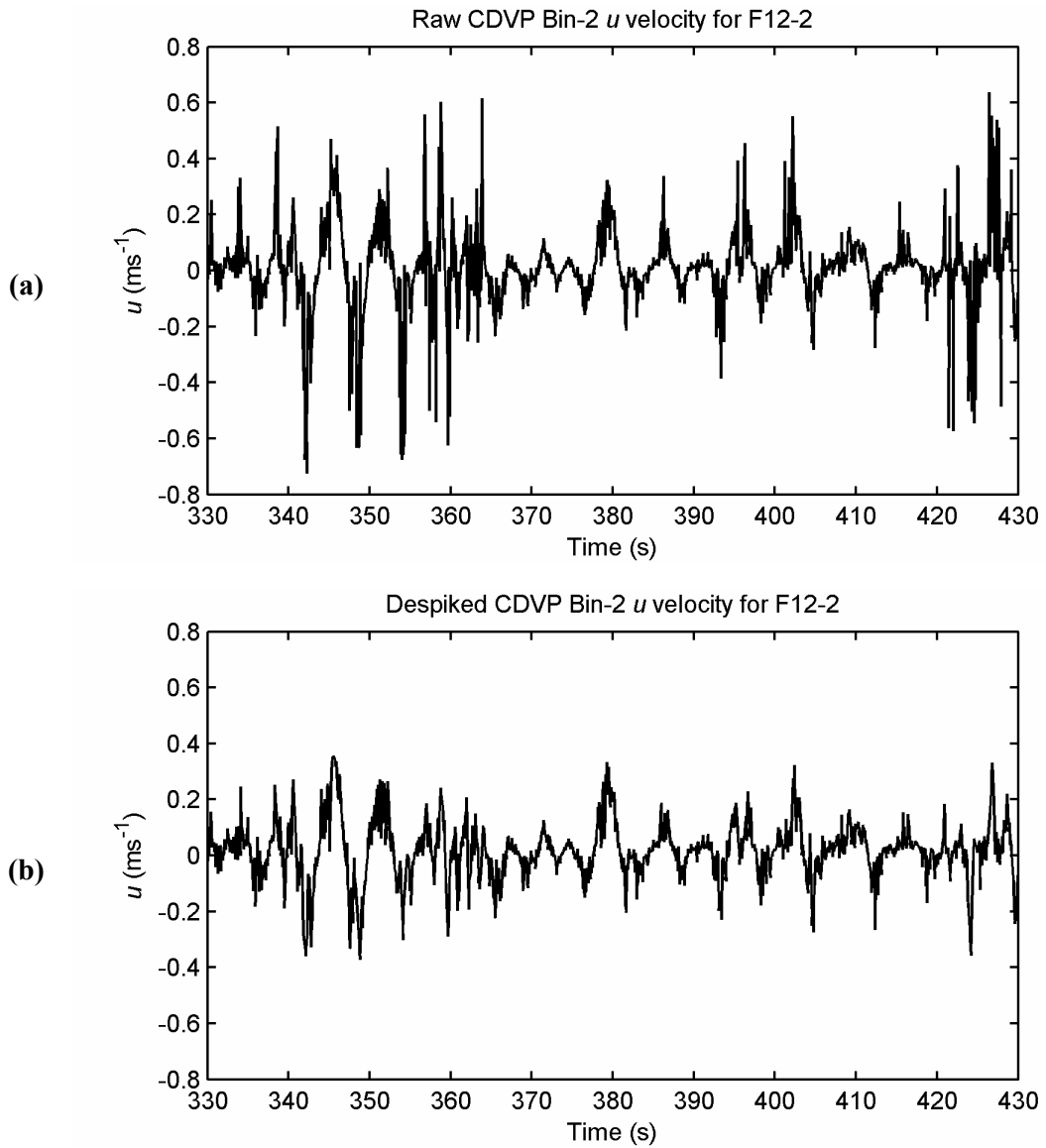


Figure 6 – Comparison between 100 seconds of (a) raw, and (b) despiked u velocities recorded by the CDVP (Bin-2) during flume test F12-2. The despiked velocities in (b) have been plotted to the same scale as the raw velocities in (a) to aid comparison.

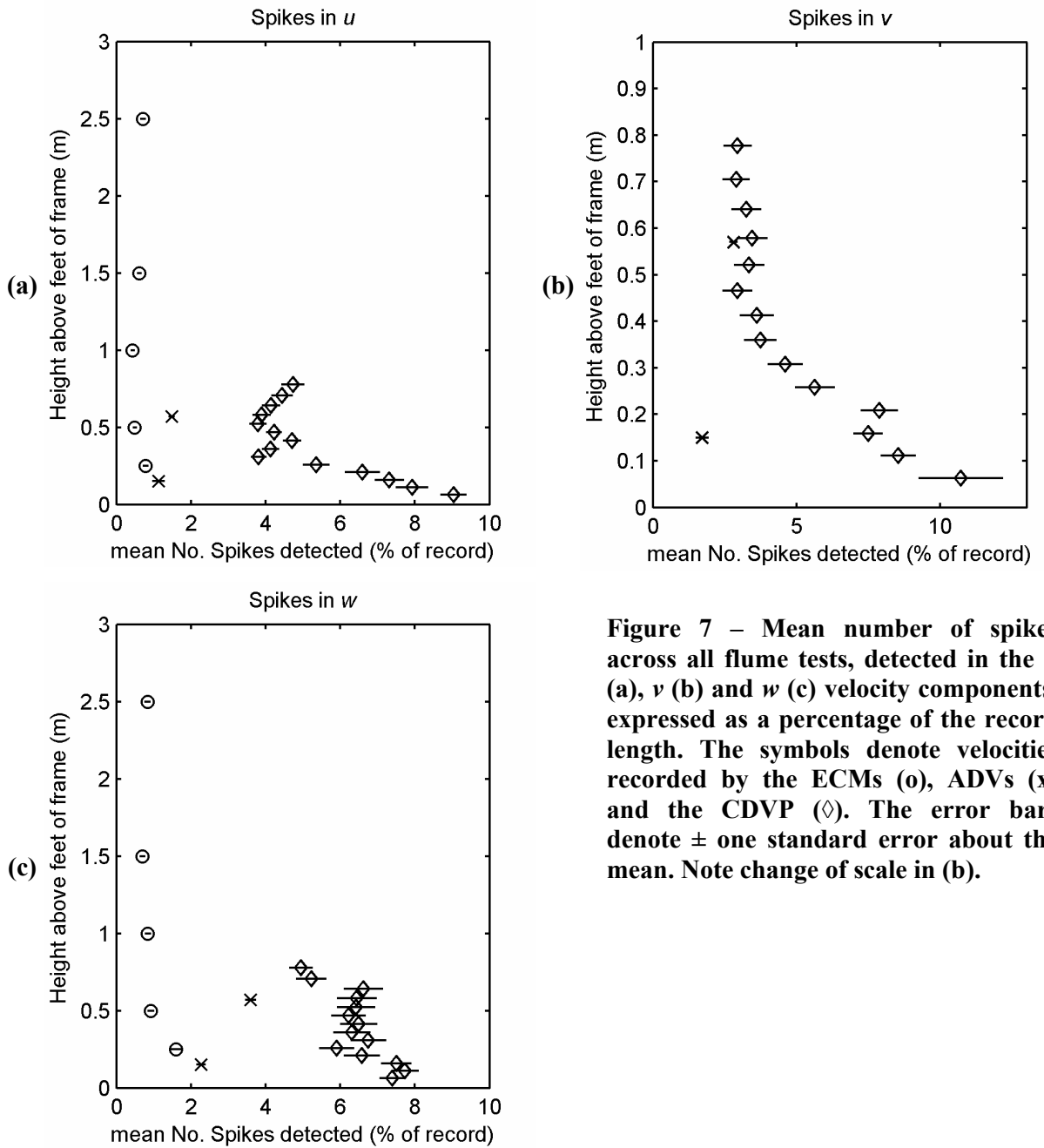


Figure 7 – Mean number of spikes across all flume tests, detected in the u (a), v (b) and w (c) velocity components, expressed as a percentage of the record length. The symbols denote velocities recorded by the ECMs (o), ADVs (x) and the CDVP (◇). The error bars denote \pm one standard error about the mean. Note change of scale in (b).

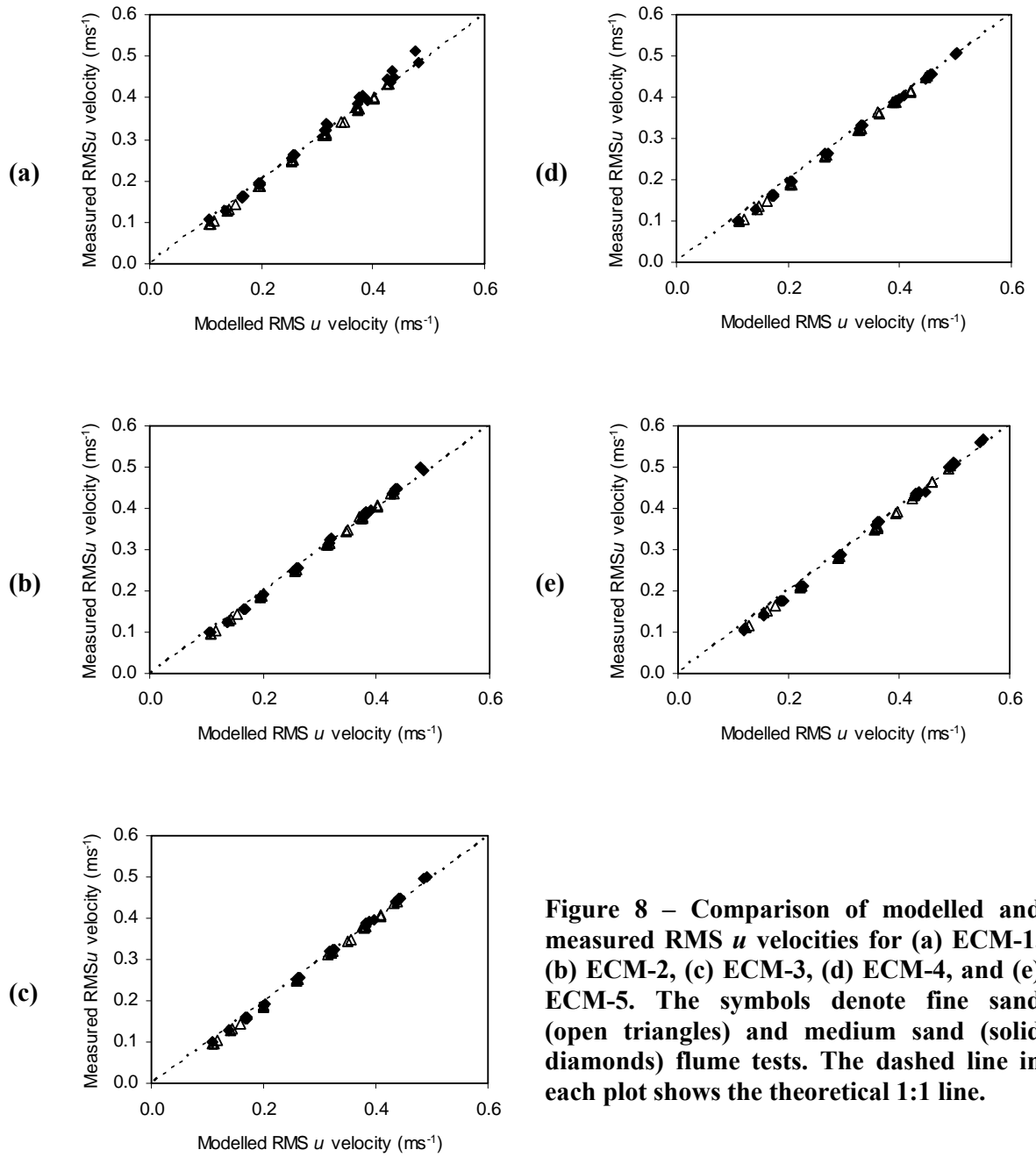


Figure 8 – Comparison of modelled and measured RMS u velocities for (a) ECM-1, (b) ECM-2, (c) ECM-3, (d) ECM-4, and (e) ECM-5. The symbols denote fine sand (open triangles) and medium sand (solid diamonds) flume tests. The dashed line in each plot shows the theoretical 1:1 line.

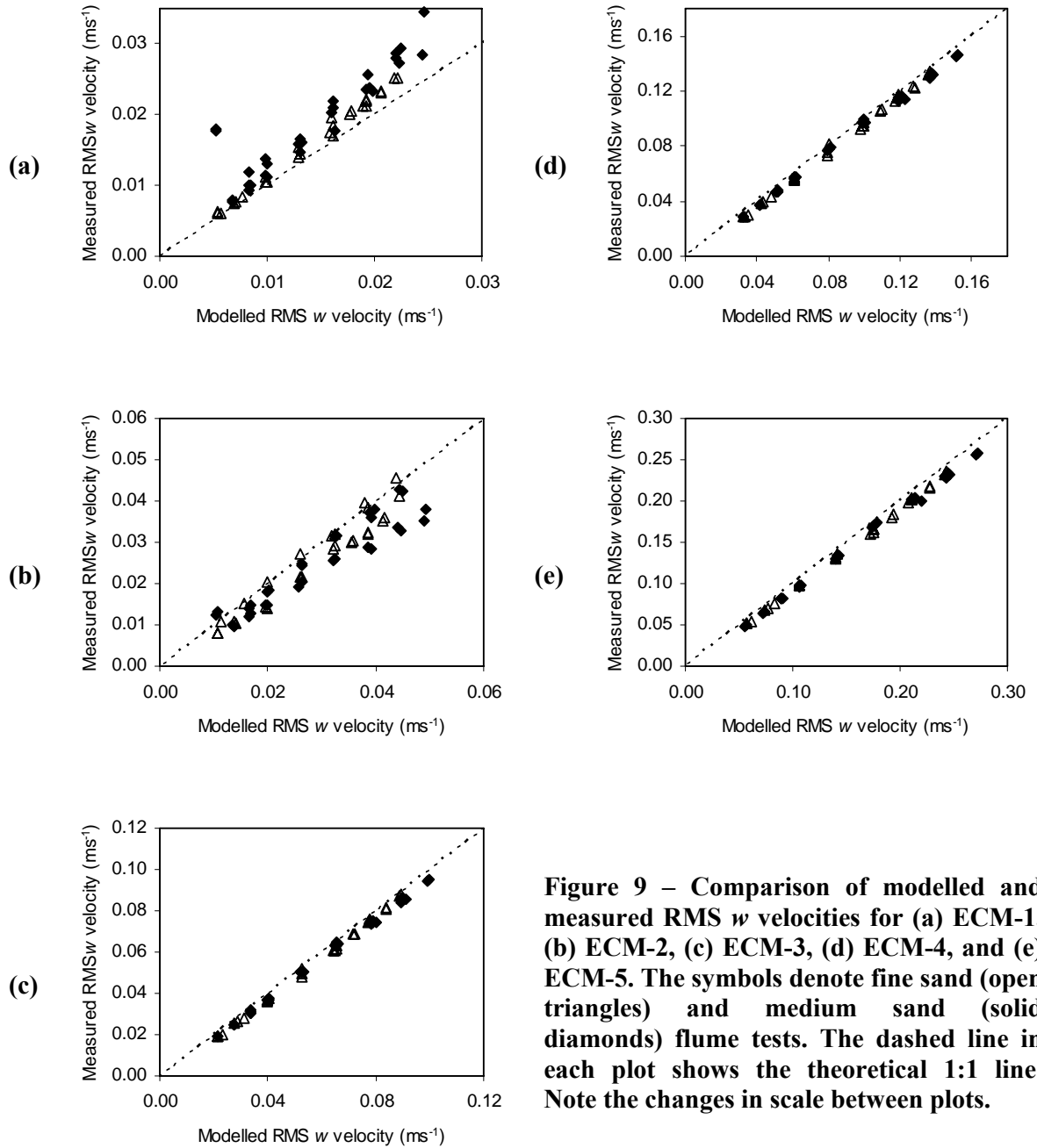


Figure 9 – Comparison of modelled and measured RMS w velocities for (a) ECM-1, (b) ECM-2, (c) ECM-3, (d) ECM-4, and (e) ECM-5. The symbols denote fine sand (open triangles) and medium sand (solid diamonds) flume tests. The dashed line in each plot shows the theoretical 1:1 line. Note the changes in scale between plots.

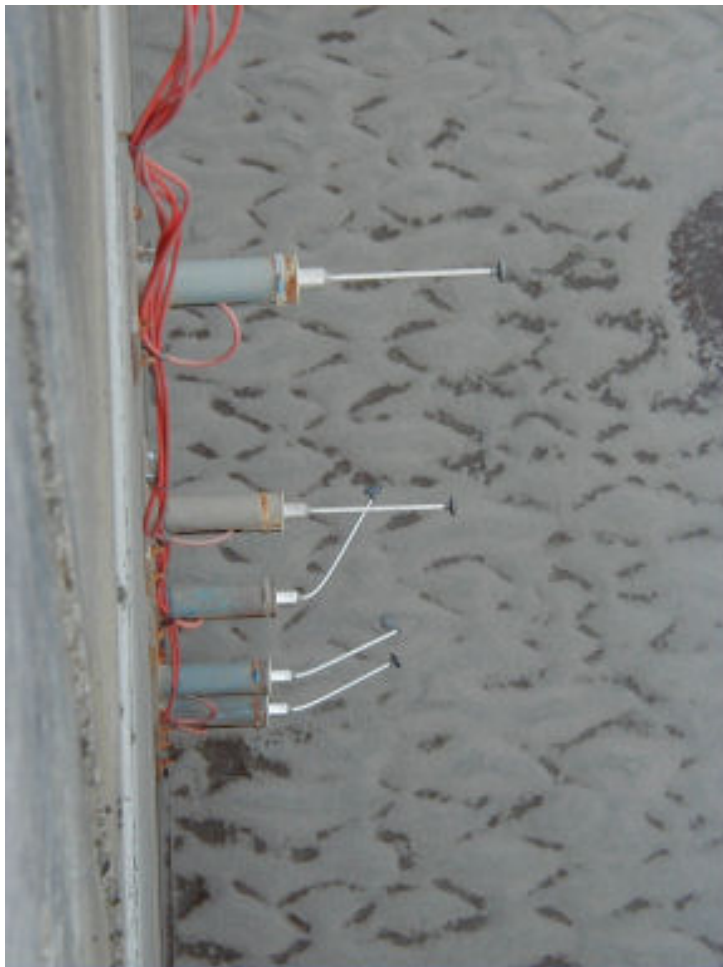


Figure 10 – Photograph of ECM damage which occurred during the fine sand flume tests.

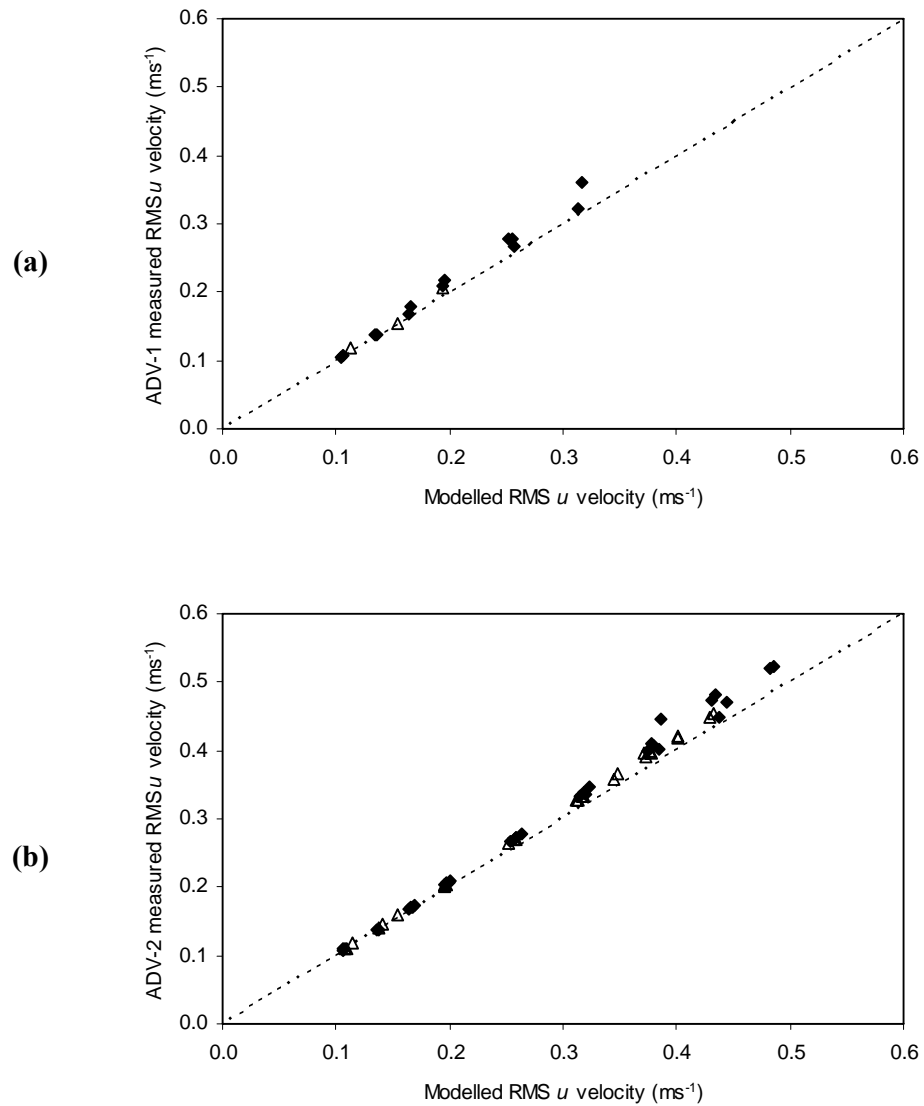


Figure 11 – Comparison of modelled and measured RMS u velocities for (a) ADV-1, and (b) ADV-2. The symbols denote fine sand (open triangles) and medium sand (solid diamonds) flume tests. The dashed line in each plot shows the theoretical 1:1 line.

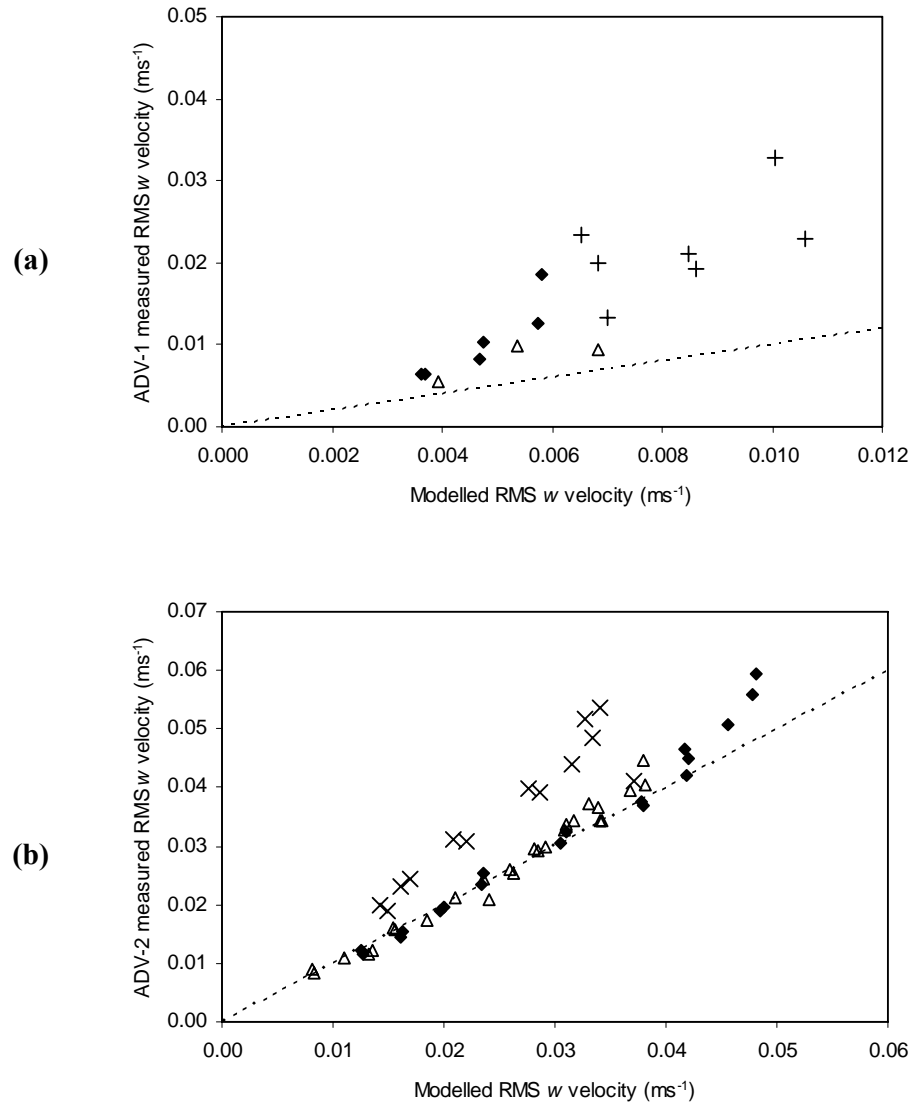


Figure 12 – Comparison of modelled and measured RMS w velocities for (a) ADV-1, and (b) ADV-2. The symbols denote fine sand flume tests outside the WBBL (open triangles), medium sand flume tests outside the WBBL (solid diamonds), flume tests inside the WBBL (+) and flume tests M10-1 to M17-2 (crosses). The dashed line in each plot shows the theoretical 1:1 line.

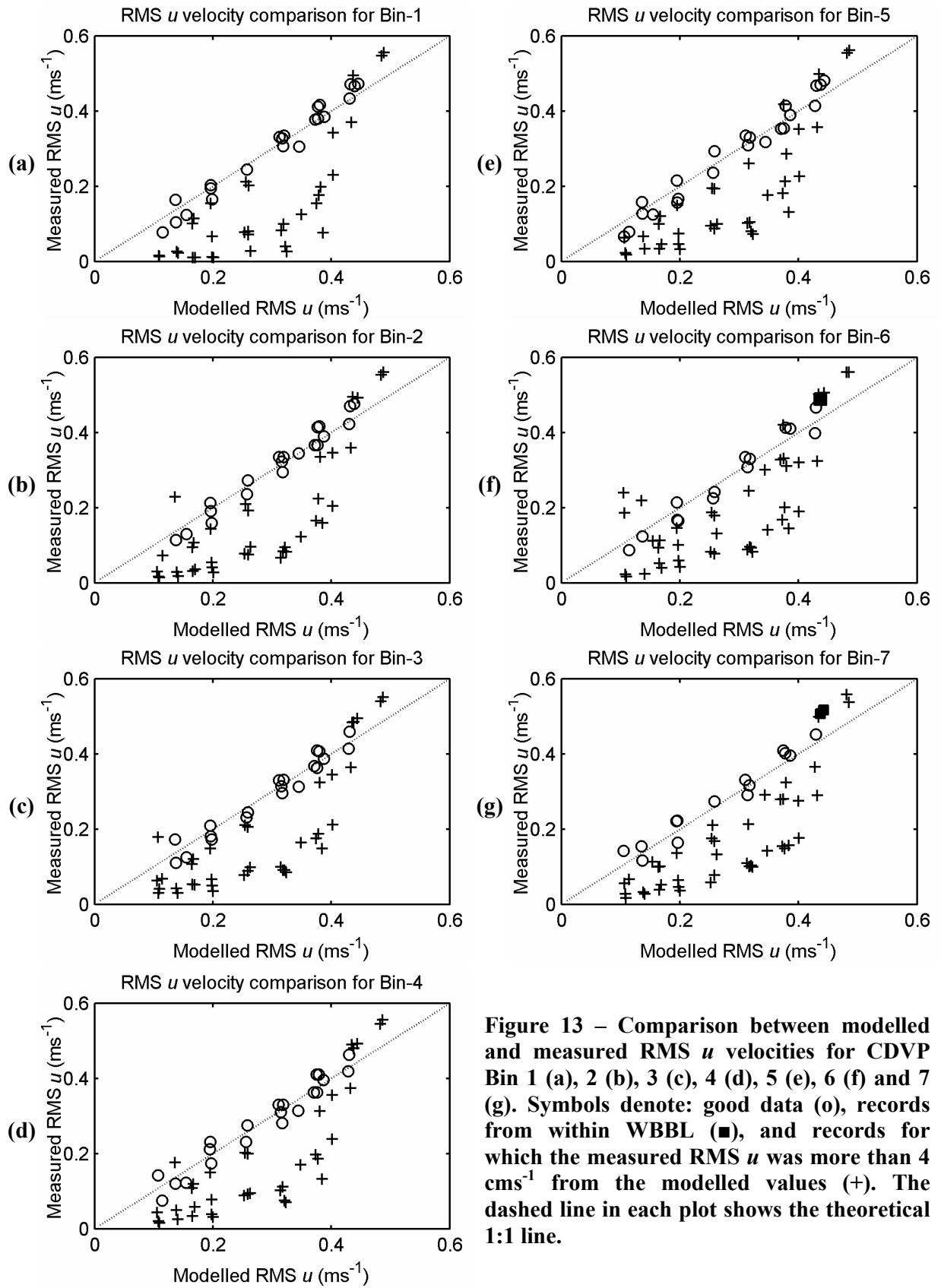


Figure 13 – Comparison between modelled and measured RMS u velocities for CDVP Bin 1 (a), 2 (b), 3 (c), 4 (d), 5 (e), 6 (f) and 7 (g). Symbols denote: good data (o), records from within WBBL (■), and records for which the measured RMS u was more than 4 cm s^{-1} from the modelled values (+). The dashed line in each plot shows the theoretical 1:1 line.

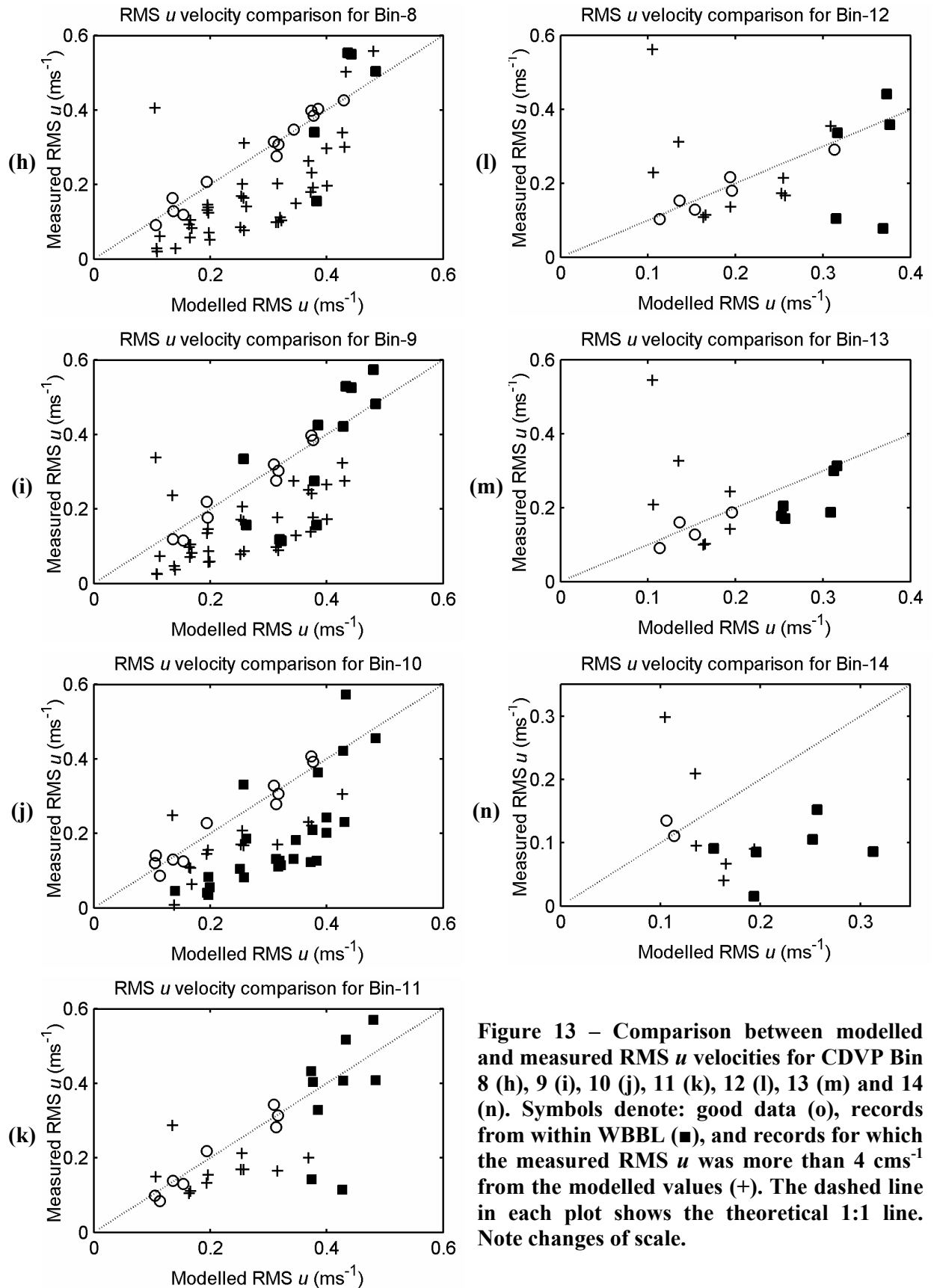


Figure 13 – Comparison between modelled and measured RMS u velocities for CDVP Bin 8 (h), 9 (i), 10 (j), 11 (k), 12 (l), 13 (m) and 14 (n). Symbols denote: good data (o), records from within WBBL (■), and records for which the measured RMS u was more than 4 cm s⁻¹ from the modelled values (+). The dashed line in each plot shows the theoretical 1:1 line. Note changes of scale.

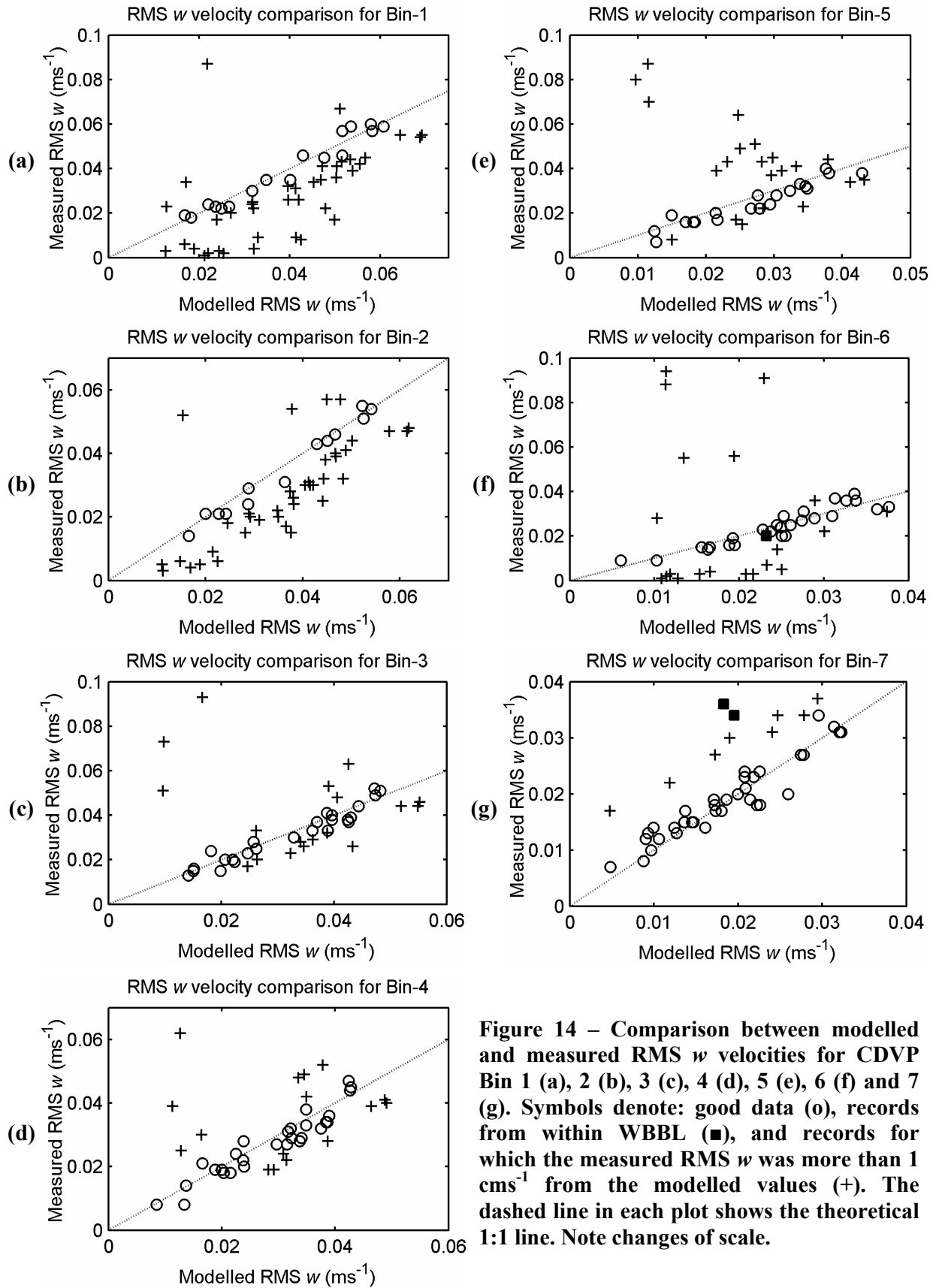


Figure 14 – Comparison between modelled and measured RMS w velocities for CDVP Bin 1 (a), 2 (b), 3 (c), 4 (d), 5 (e), 6 (f) and 7 (g). Symbols denote: good data (o), records from within WBBL (■), and records for which the measured RMS w was more than 1 cm s^{-1} from the modelled values (+). The dashed line in each plot shows the theoretical 1:1 line. Note changes of scale.

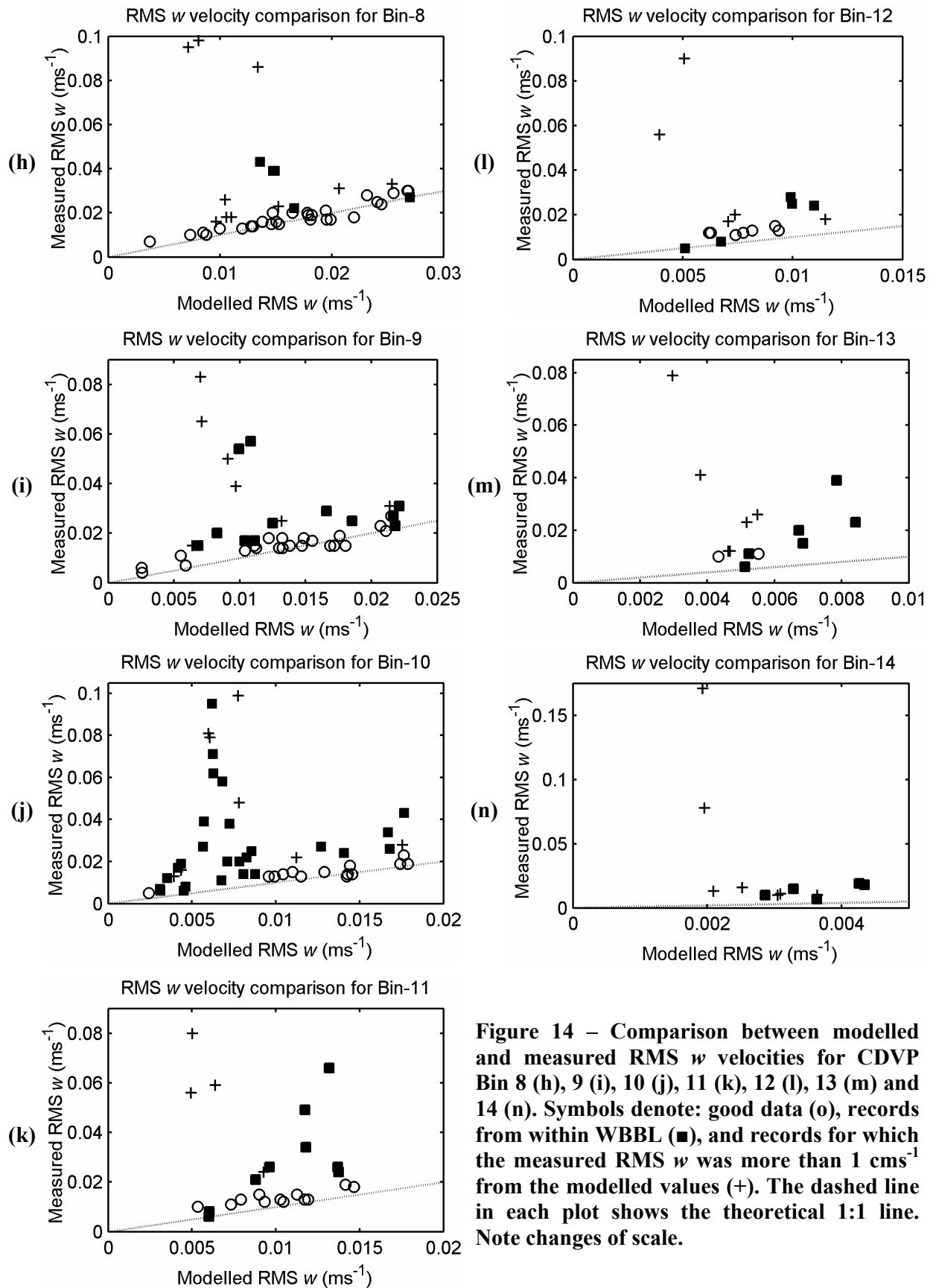


Figure 14 – Comparison between modelled and measured RMS w velocities for CDVP Bin 8 (h), 9 (i), 10 (j), 11 (k), 12 (l), 13 (m) and 14 (n). Symbols denote: good data (o), records from within WBBL (■), and records for which the measured RMS w was more than 1 cm s^{-1} from the modelled values (+). The dashed line in each plot shows the theoretical 1:1 line. Note changes of scale.

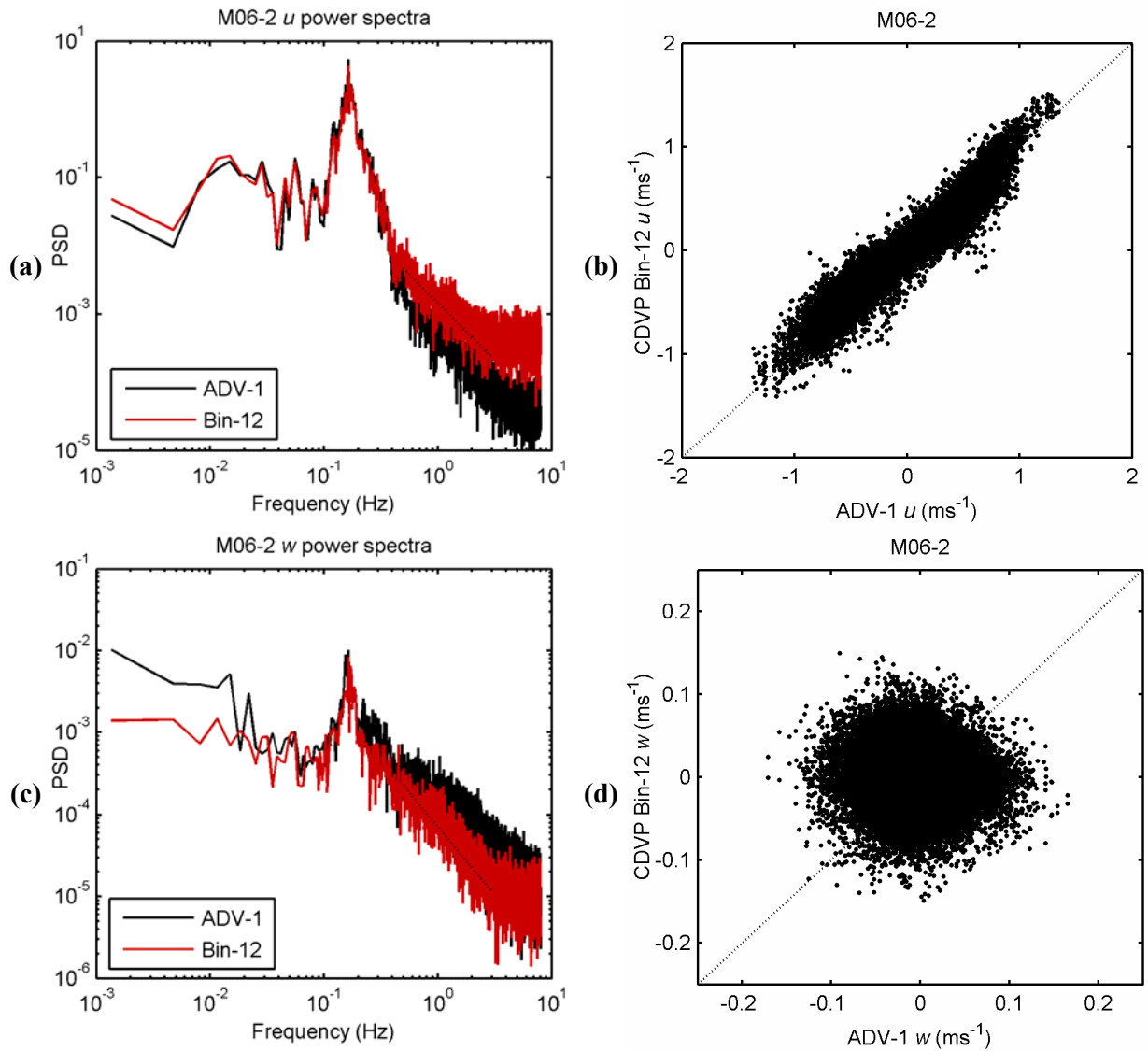


Figure 15 – Comparison between CDVP Bin-12 and ADV-1 derived u power spectra (a), u velocities (b), w power spectra (c) and w velocities (d), for flume test M06-2. The dashed line in plots (a) and (c) depicts $f^{5/3}$, whilst the dashed line in plots (b) and (d) shows the theoretical 1:1 line.

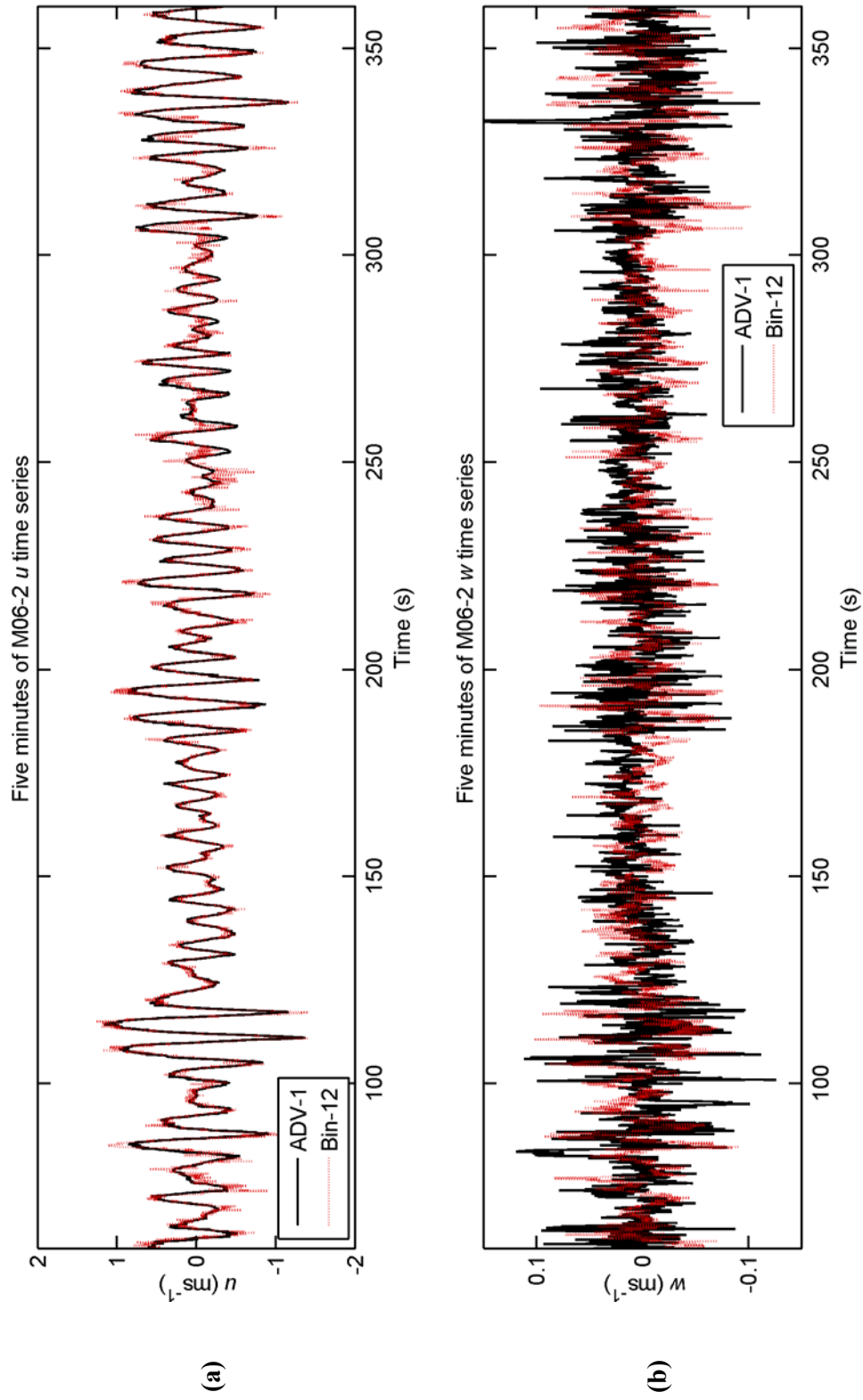


Figure 16 – Comparison between CDVP Bin-12 and ADV-1 derived time series for (a) u , and (b) w velocity components from flume test M06-2.

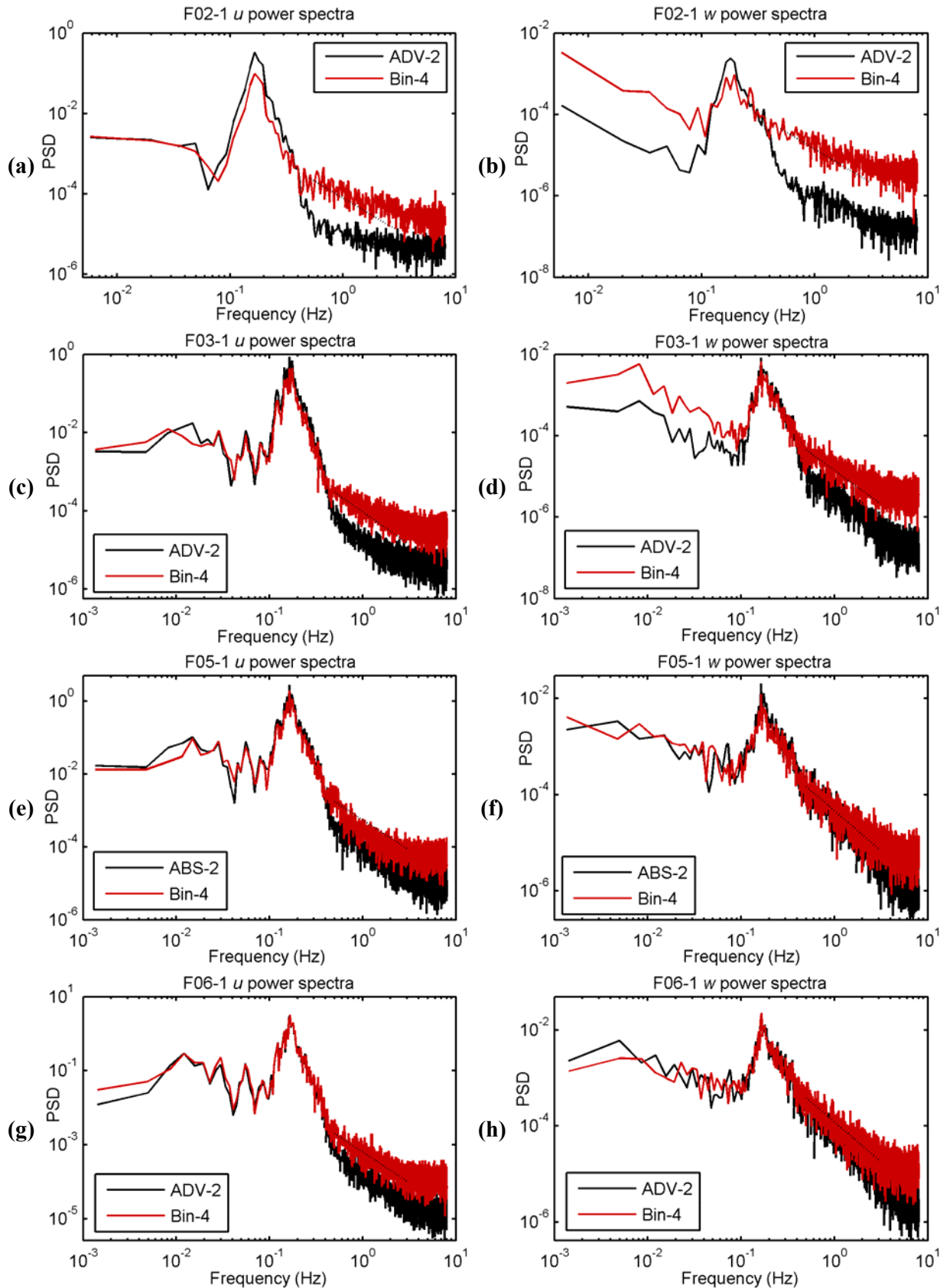


Figure 17 – Comparison between CDVP Bin-4 and ADV-2 derived power spectra for (a) F02-1 u , (b) F02-1 w , (c) F03-1 u , (d) F03-1 w , (e) F05-1 u , (f) F05-1 w , (g) F06-1 u , and (h) F06-1 w . The dashed line in each plot depicts $f^{5/3}$.

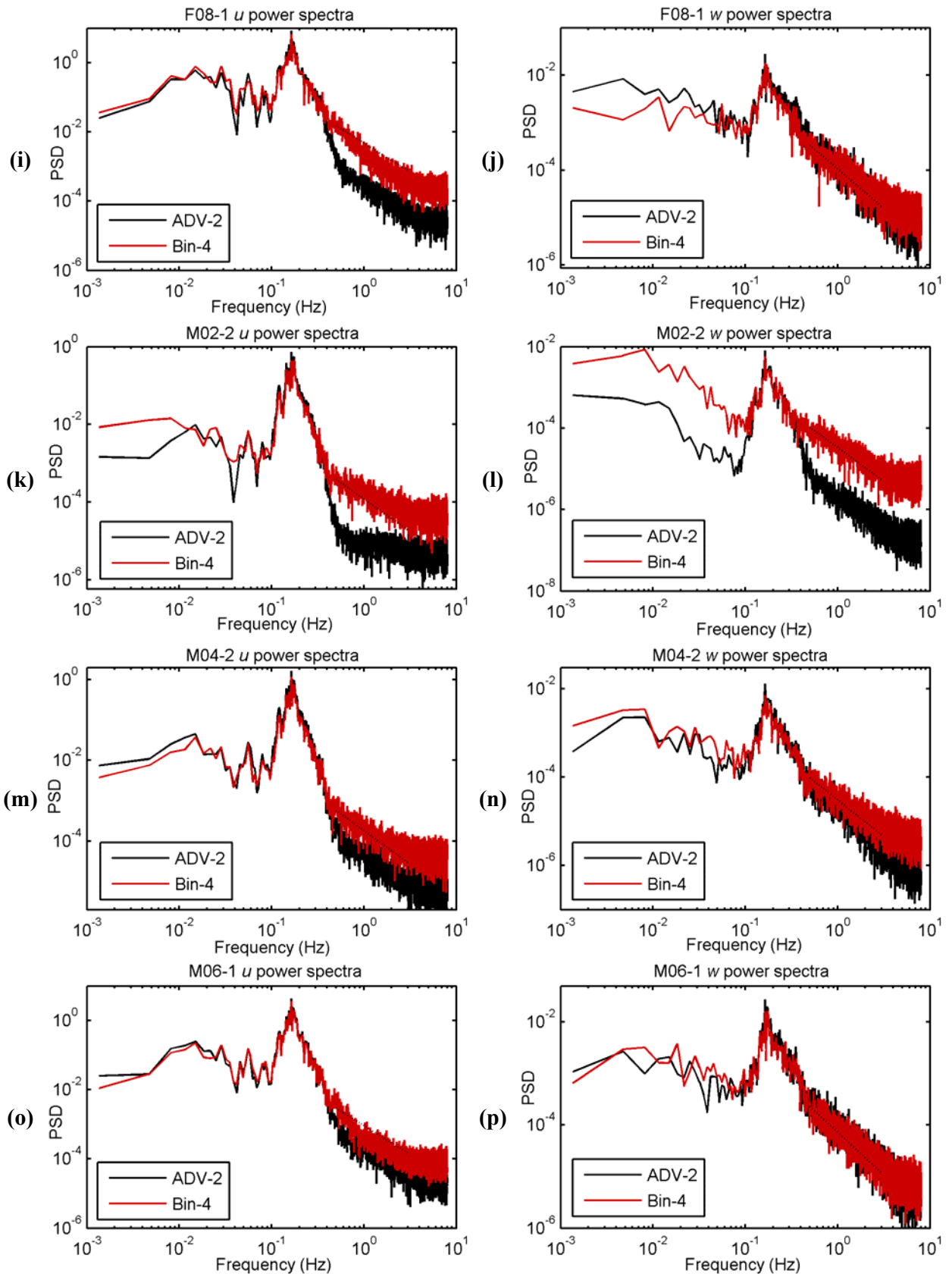


Figure 17 – Comparison between CDVP Bin-4 and ADV-2 derived power spectra for (i) F08-1 u , (j) F08-1 w , (k) M02-2 u , (l) M02-2 w , (m) M04-2 u , (n) M04-2 w , (o) M06-1 u , and (p) M06-1 w . The dashed line in each plot depicts $f^{5/3}$.

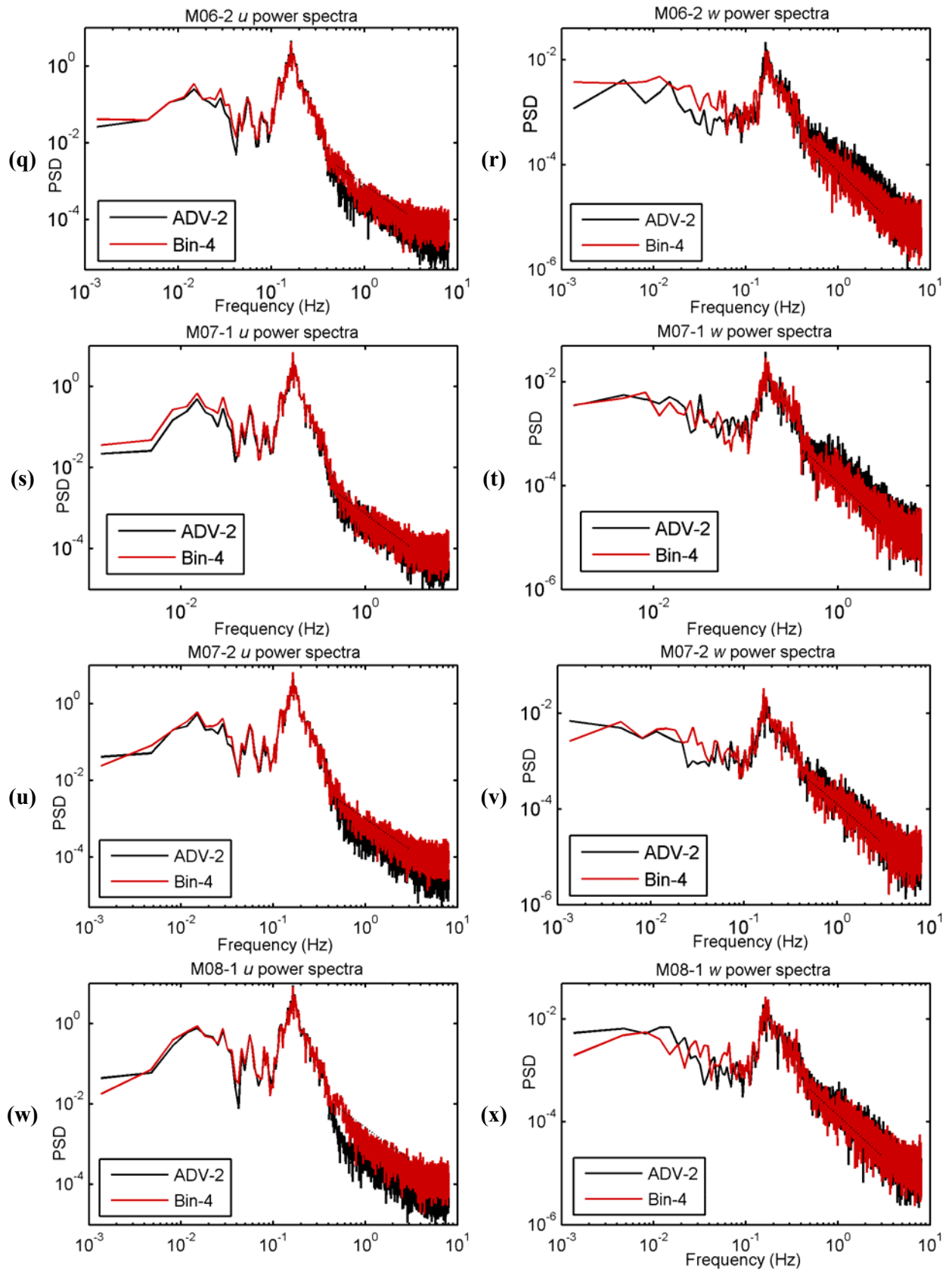


Figure 17 – Comparison between CDVP Bin-4 and ADV-2 derived power spectra for (q) M06-2 u , (r) M06-2 w , (s) M07-1 u , (t) M07-1 w , (u) M07-2 u , (v) M07-2 w , (w) M08-1 u , and (x) M08-1 w . The dashed line in each plot depicts $f^{5/3}$.

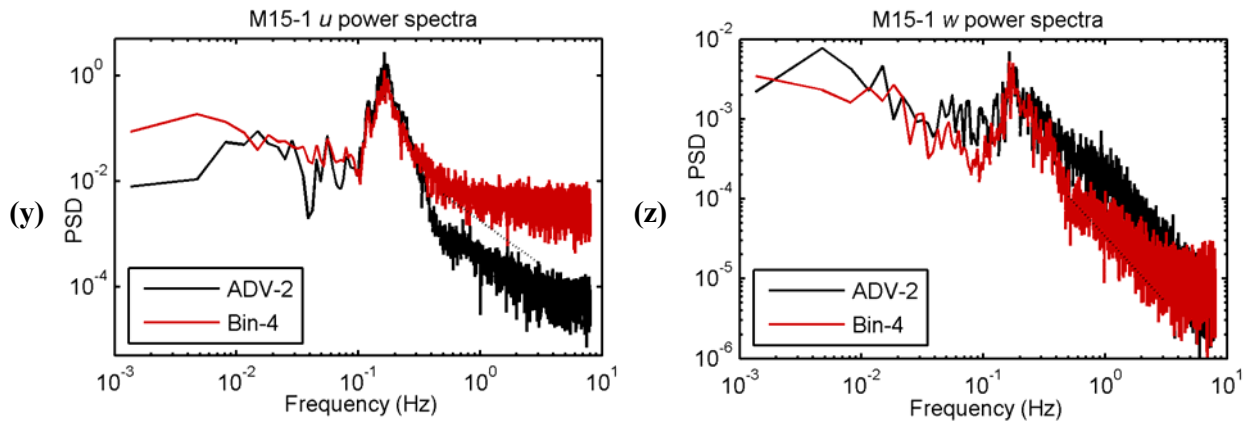


Figure 17 – Comparison between CDVP Bin-4 and ADV-2 derived power spectra for (y) M15-1 u , and (z) M15-1 w . The dashed line in each plot depicts $f^{5/3}$.

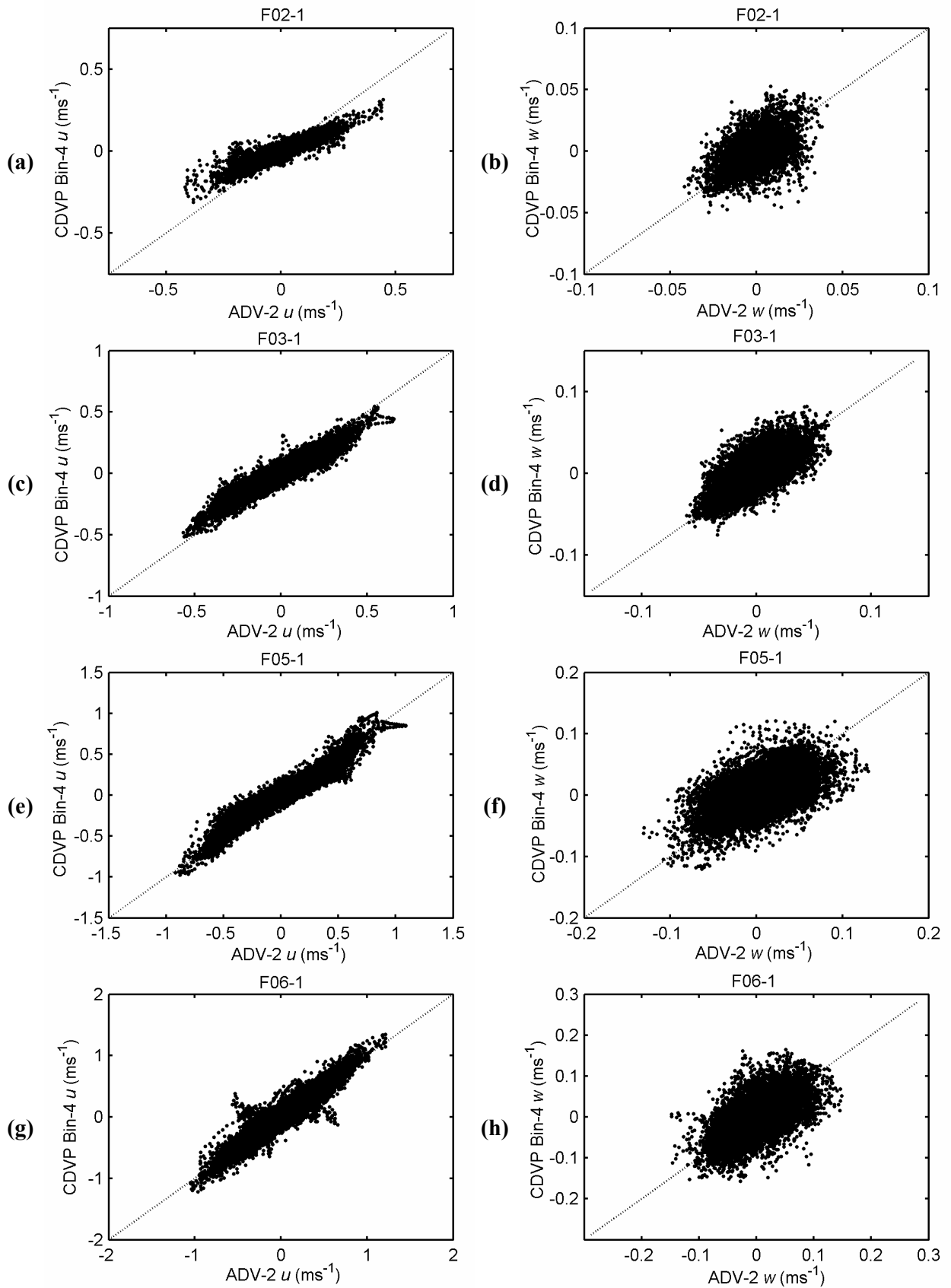


Figure 18 – Comparison between CDVP Bin-4 and ADV-2 recorded velocities for (a) F02-1 u , (b) F02-1 w , (c) F03-1 u , (d) F03-1 w , (e) F05-1 u , (f) F05-1 w , (g) F06-1 u , and (h) F06-1 w . The dashed line in each plot shows the theoretical 1:1 line.

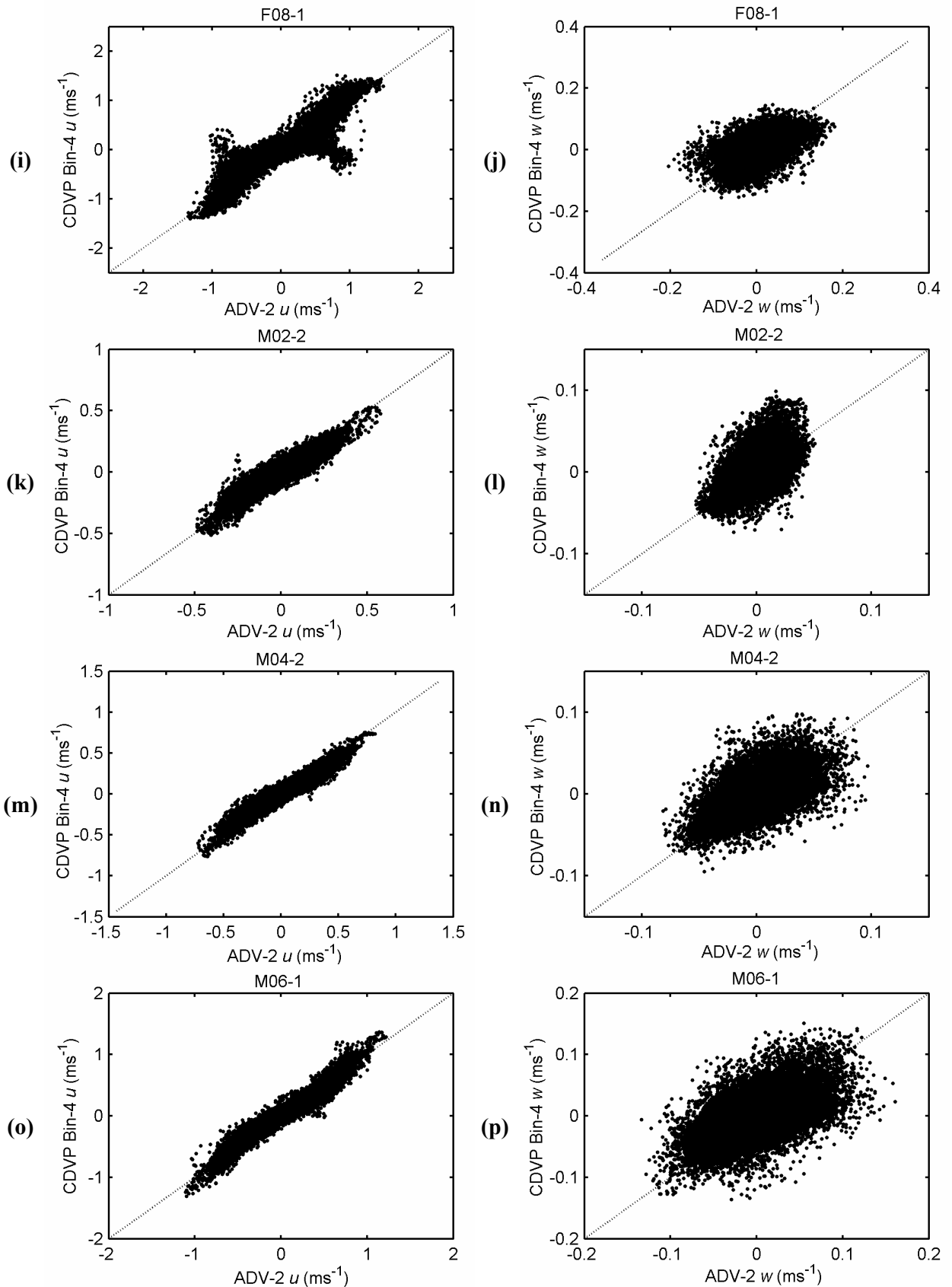


Figure 18 – Comparison between CDVP Bin-4 and ADV-2 recorded velocities for (i) F08-1 u , (j) F08-1 w , (k) M02-2 u , (l) M02-2 w , (m) M04-2 u , (n) M04-2 w , (o) M06-1 u , and (p) M06-1 w . The dashed line in each plot shows the theoretical 1:1 line.

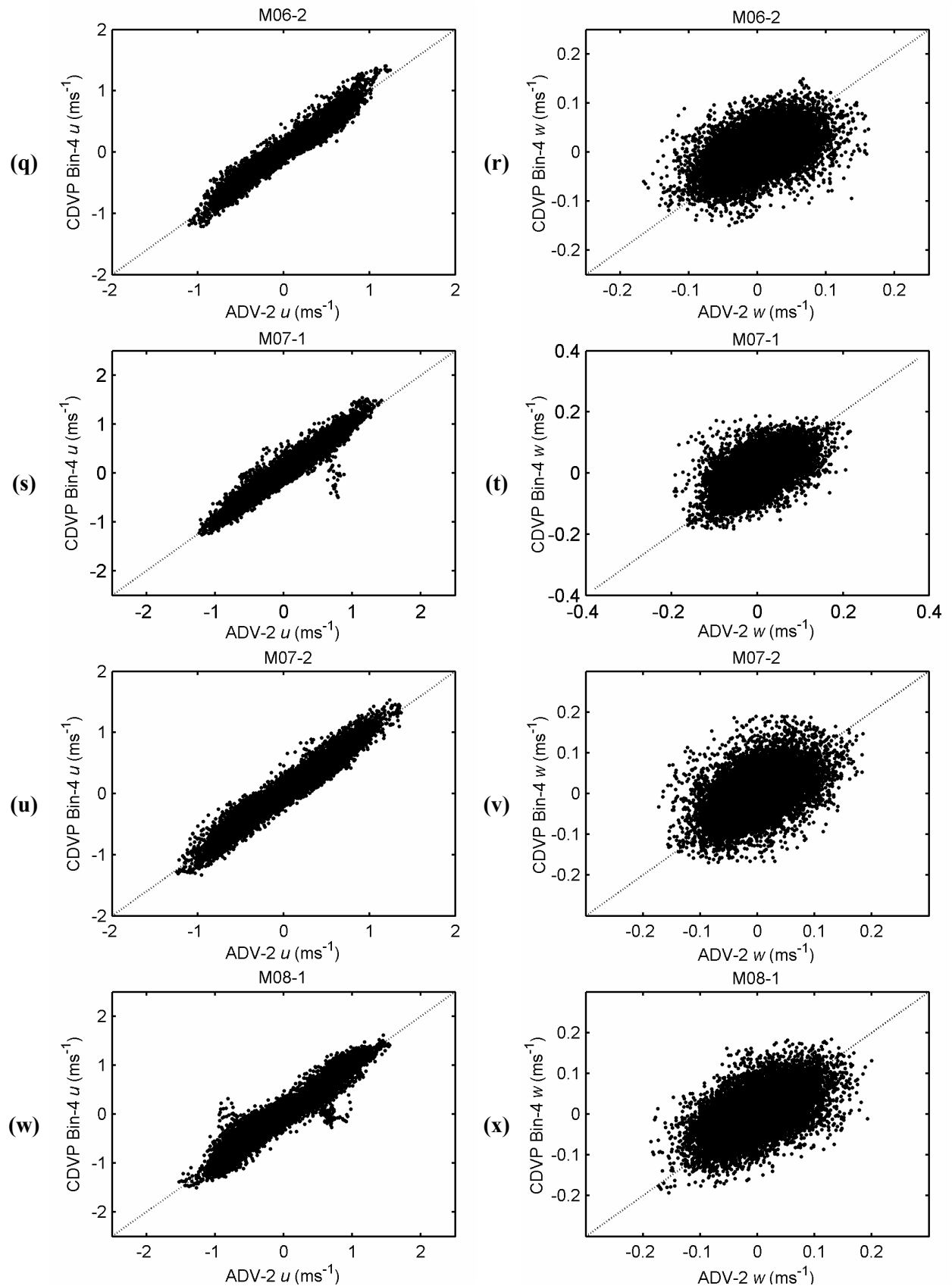


Figure 18 – Comparison between CDVP Bin-4 and ADV-2 recorded velocities for (q) M06-2 u , (r) M06-2 w , (s) M07-1 u , (t) M07-1 w , (u) M07-2 u , (v) M07-2 w , and (w) M08-1 u , (x) M08-1 w . The dashed line in each plot shows the theoretical 1:1 line.

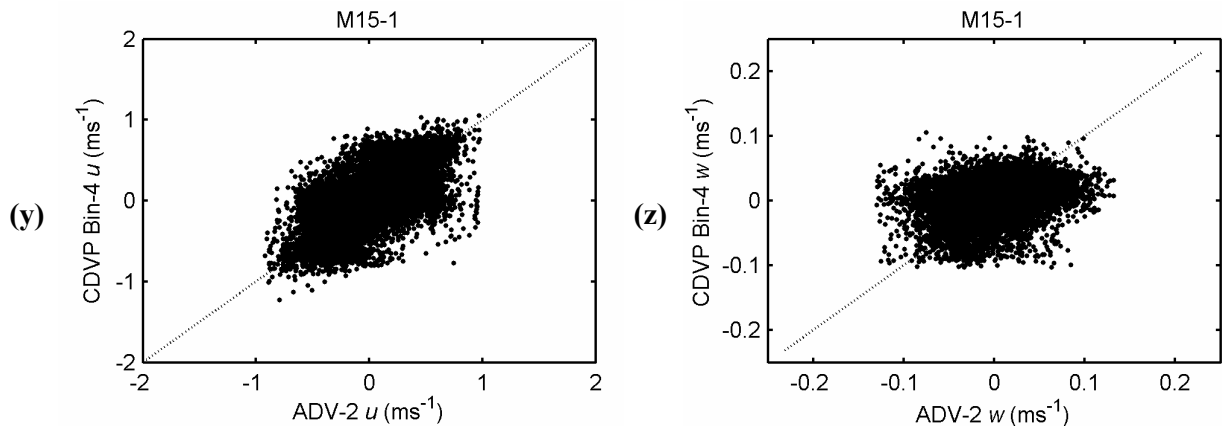


Figure 18 – Comparison between CDVP Bin-4 and ADV-2 recorded velocities for (y) M15-1 u , and (z) M15-1 w . The dashed line in each plot shows the theoretical 1:1 line.

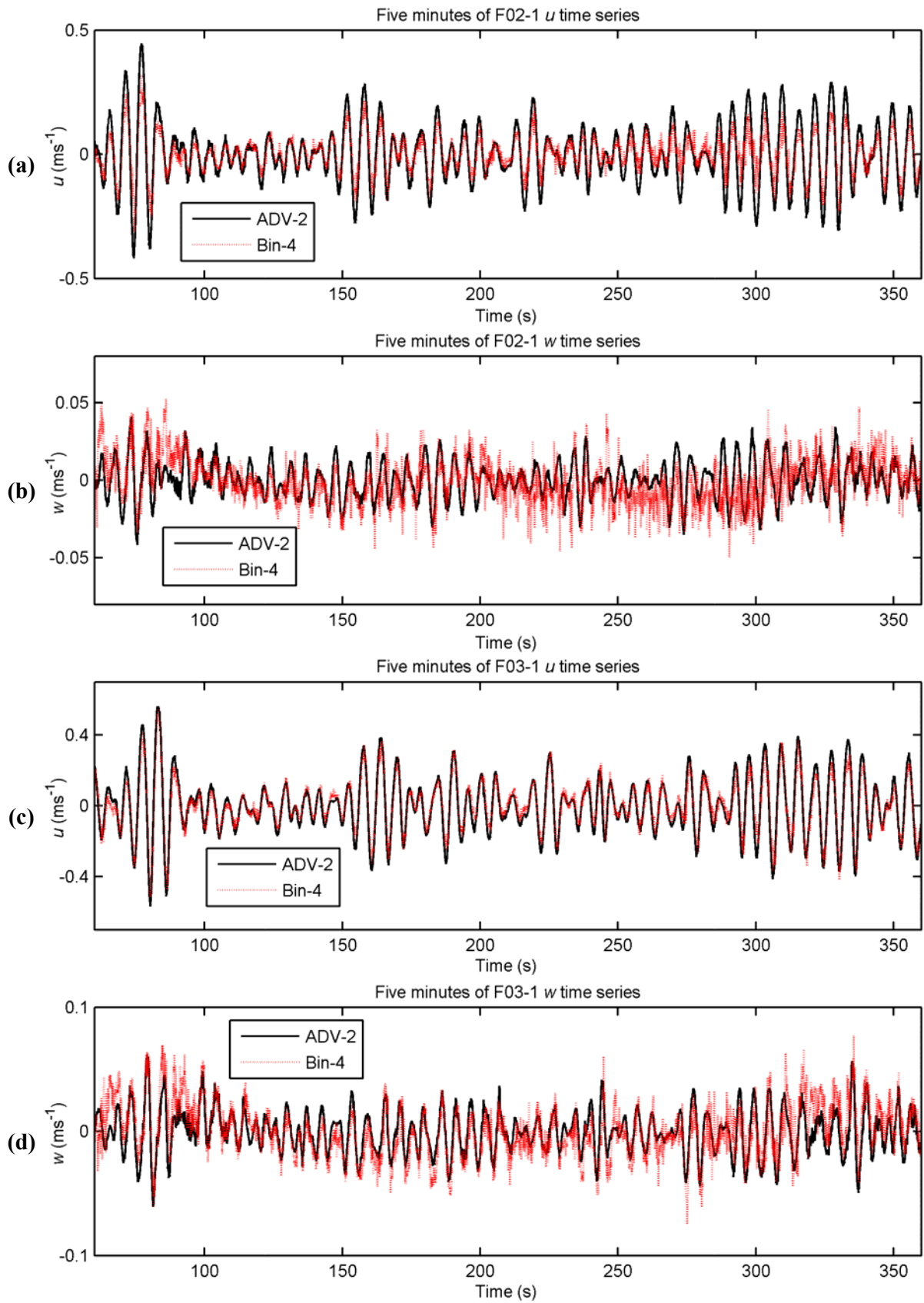


Figure 19 – Comparison between CDVP Bin-4 and ADV-2 derived time series for (a) F02-1 u , (b) F02-1 w , (c) F03-1 u and (d) F03-1 w .

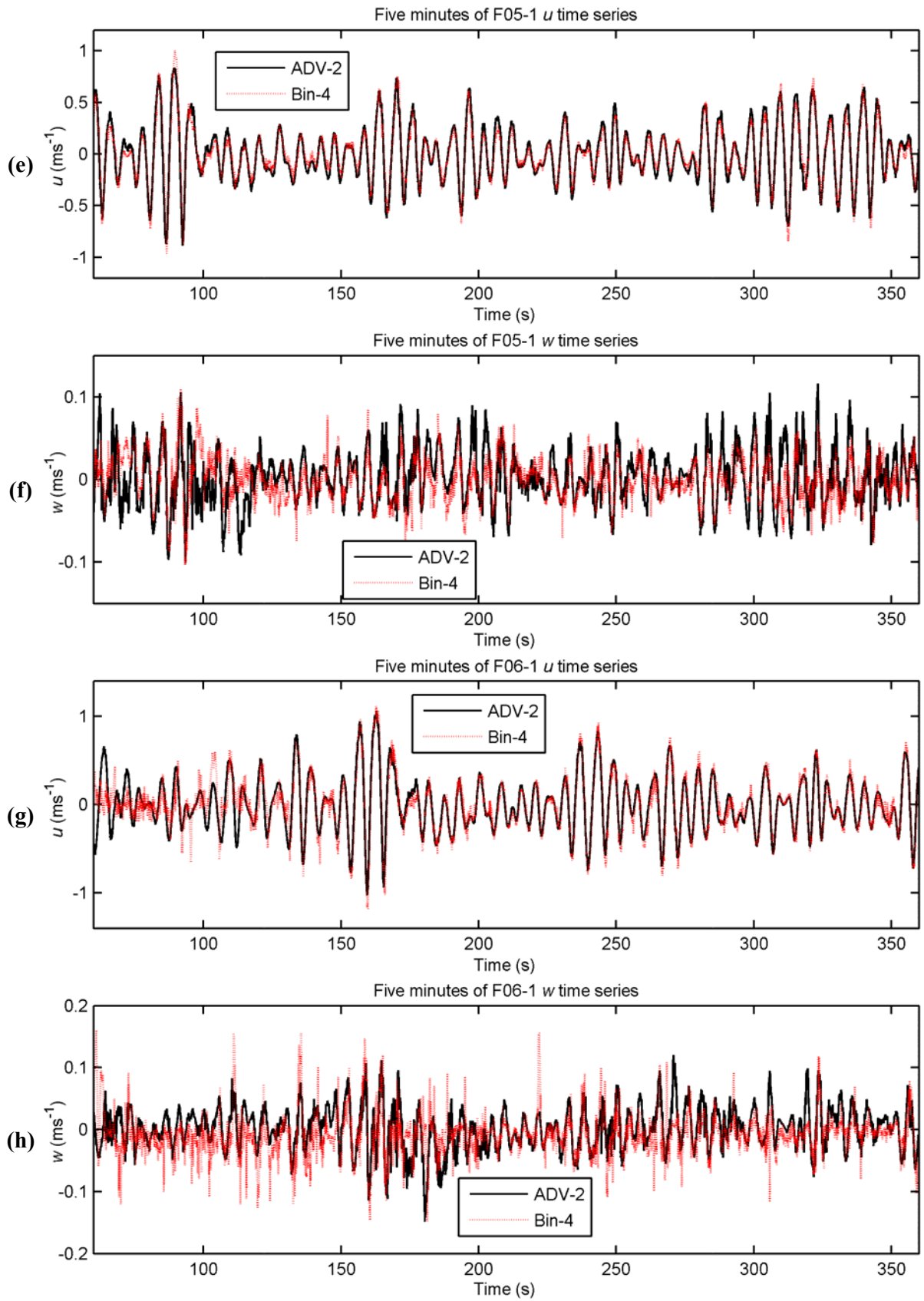


Figure 19 – Comparison between CDVP Bin-4 and ADV-2 derived time series for (e) F05-1 u , (f) F05-1 w , (g) F06-1 u and (h) F06-1 w .

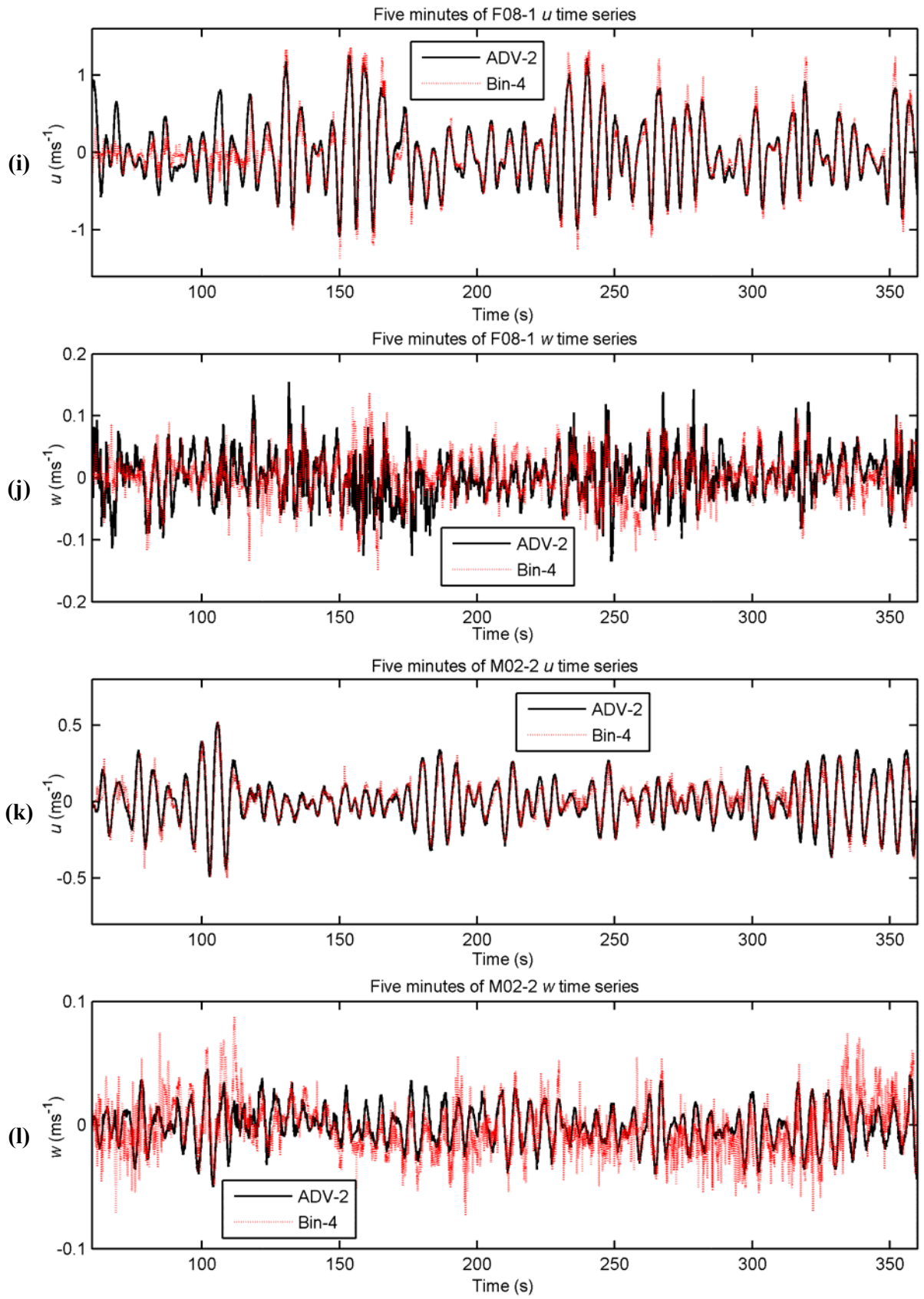


Figure 19 – Comparison between CDVP Bin-4 and ADV-2 derived time series for (i) F08-1 u , (j) F08-1 w , (k) M02-2 u and (l) M02-2 w .

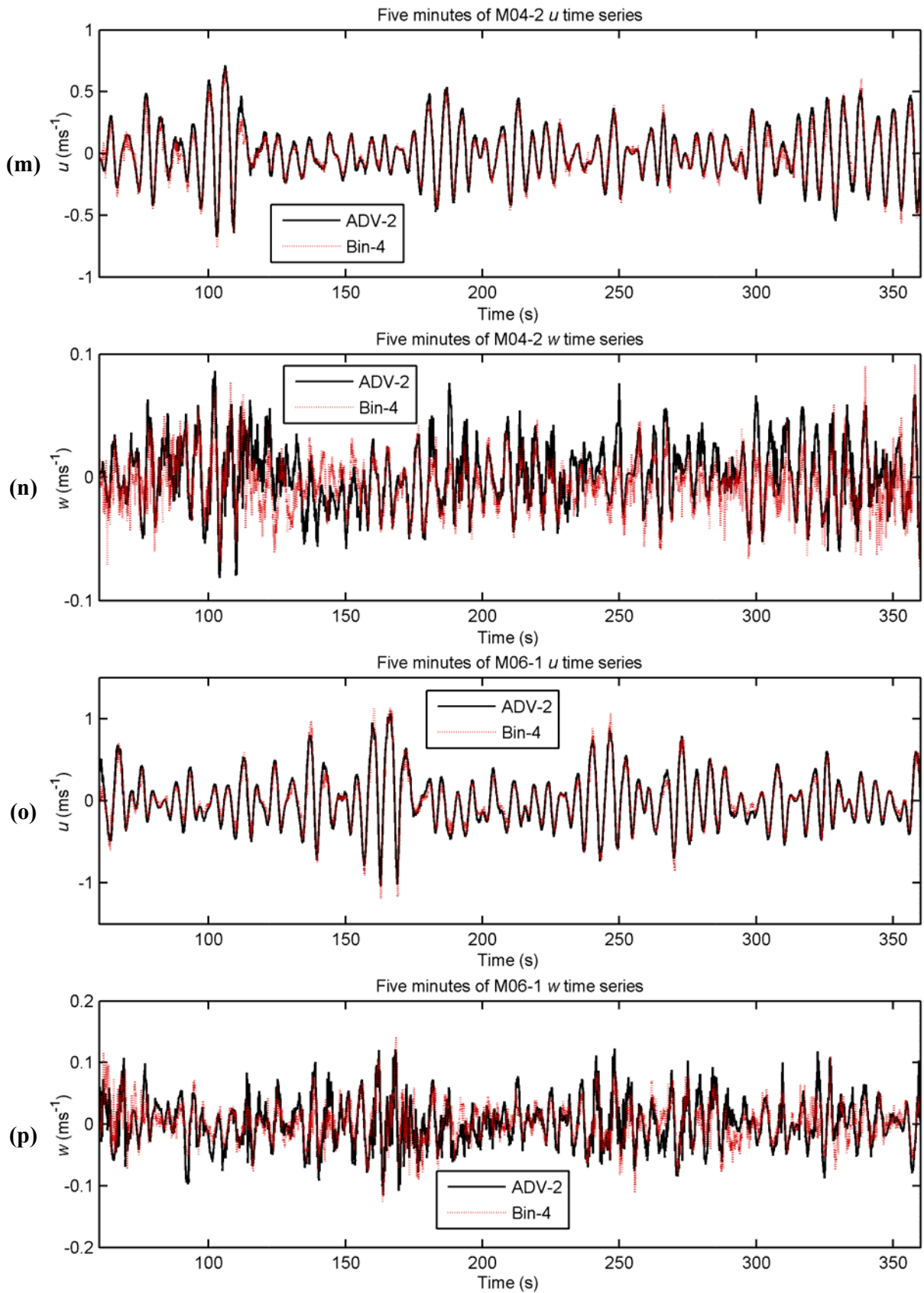


Figure 19 – Comparison between CDVP Bin-4 and ADV-2 derived time series for (m) M04-2 u , (n) M04-2 w , (o) M06-1 u and (p) M06-1 w .

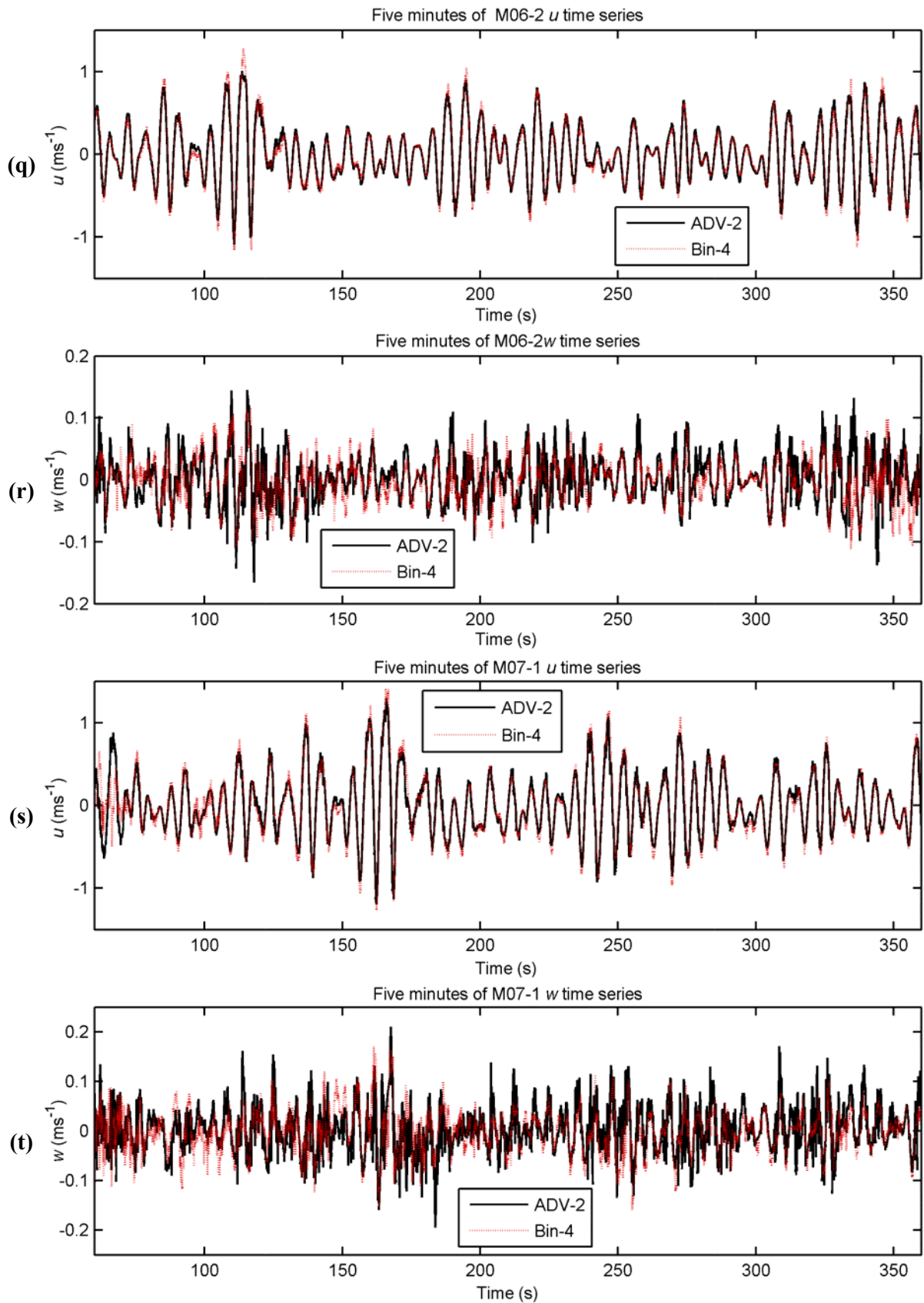


Figure 19 – Comparison between CDVP Bin-4 and ADV-2 derived time series for (q) M06-2 u , (r) M06-2 w , (s) M07-1 u and (t) M07-1 w .

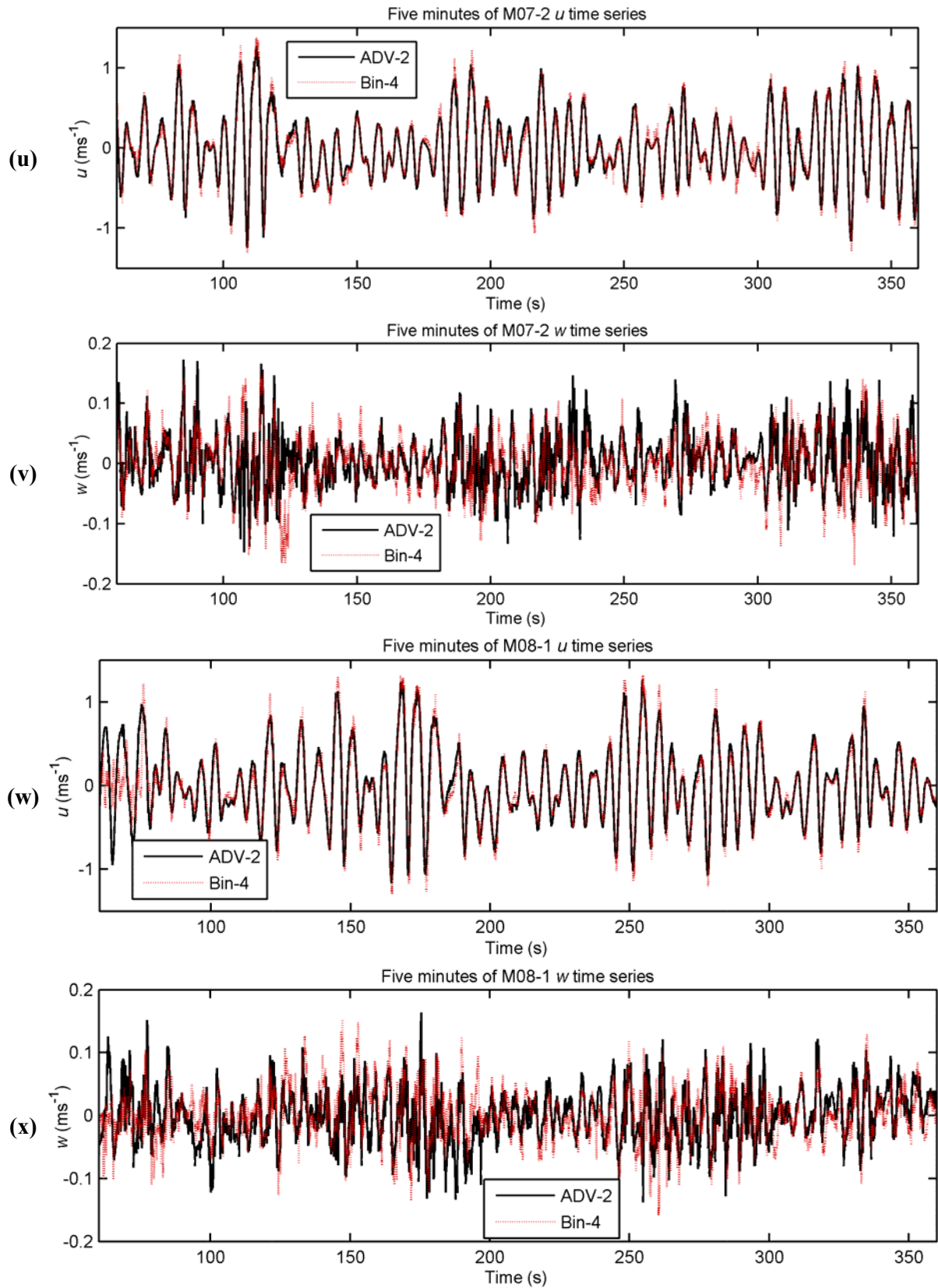


Figure 19 – Comparison between CDVP Bin-4 and ADV-2 derived time series for (u) M07-2 u , (v) M07-2 w , (w) M08-1 u and (x) M08-1 w .

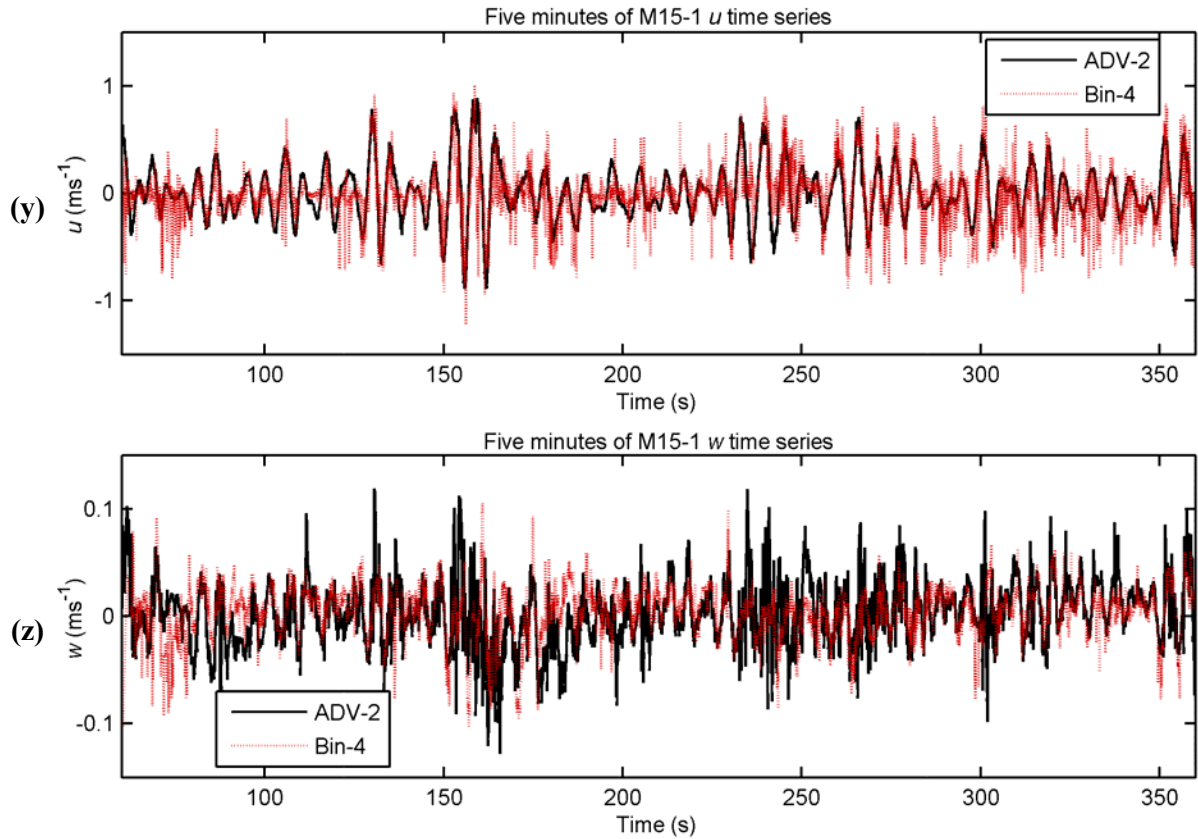


Figure 19 – Comparison between CDVP Bin-4 and ADV-2 derived time series for (y) M15-1 u and (z) M15-1 w .

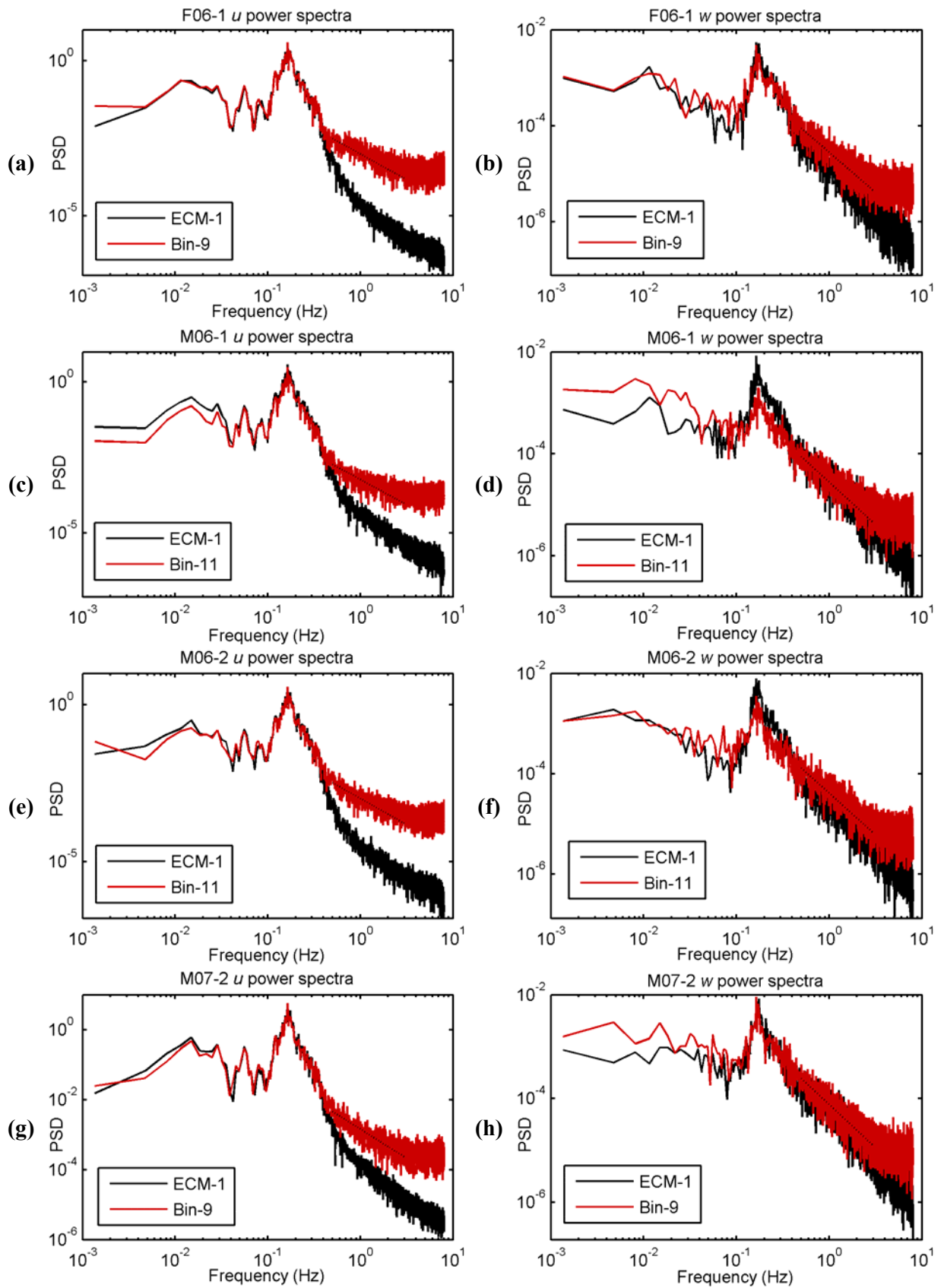


Figure 20 – Comparison between CDVP and ECM-1 derived power spectra for (a) F06-1 u , (b) F06-1 w , (c) M06-1 u , (d) M06-1 w , (e) M06-2 u , (f) M06-2 w , (g) M07-2 u , and (h) M07-2 w . The dashed line in each plot depicts $f^{-5/3}$.

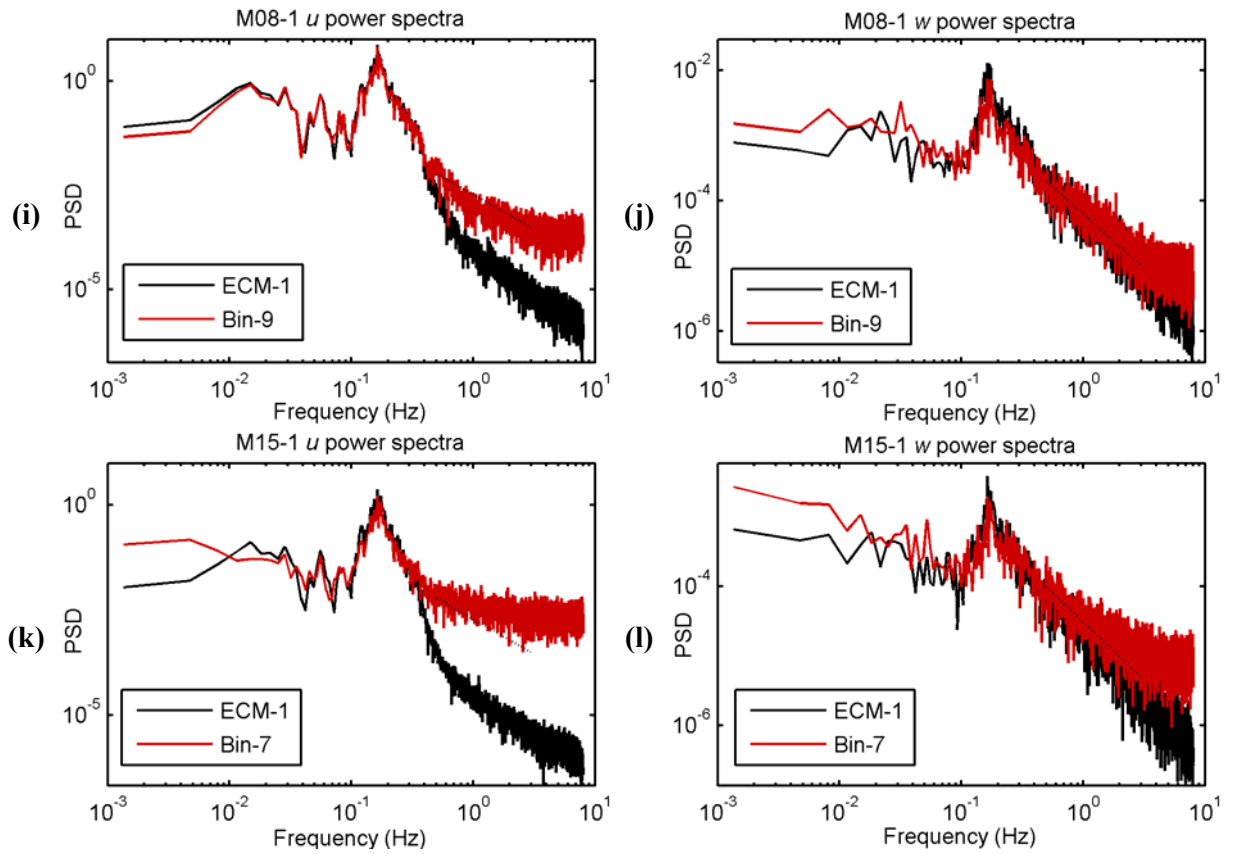


Figure 20 – Comparison between CDVP and ECM-1 derived power spectra for (i) M08-1 u , (j) M08-1 w , (k) M15-1 u , and (l) M15-1 w . The dashed line in each plot depicts $f^{5/3}$.

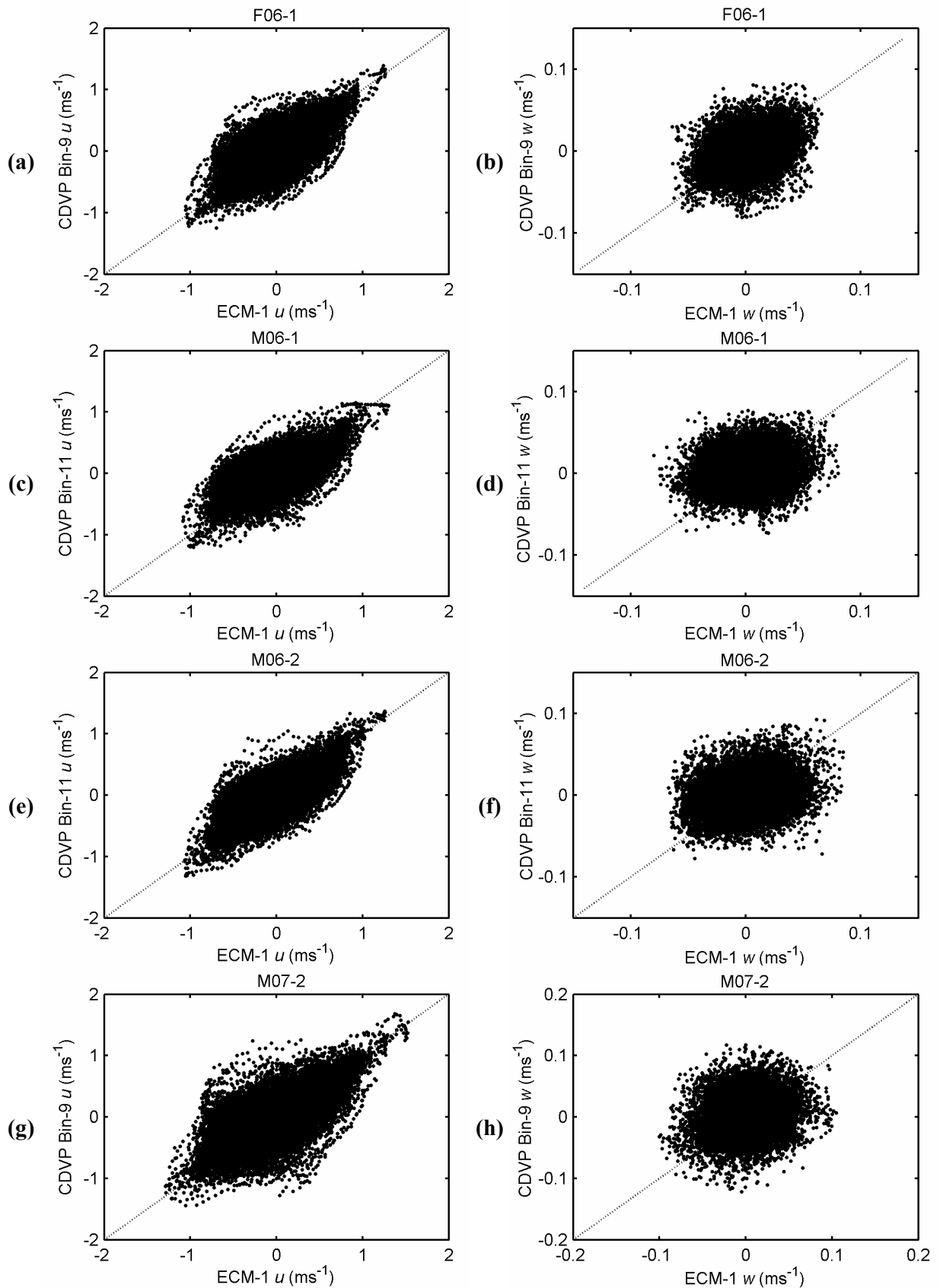


Figure 21 – Comparison between CDVP and ECM-1 recorded velocities for (a) F06-1 u , (b) F06-1 w , (c) M06-1 u , (d) M06-1 w , (e) M06-2 u , (f) M06-2 w , (g) M07-2 u , and (h) M07-2 w . The dashed line in each plot shows the theoretical 1:1 line.

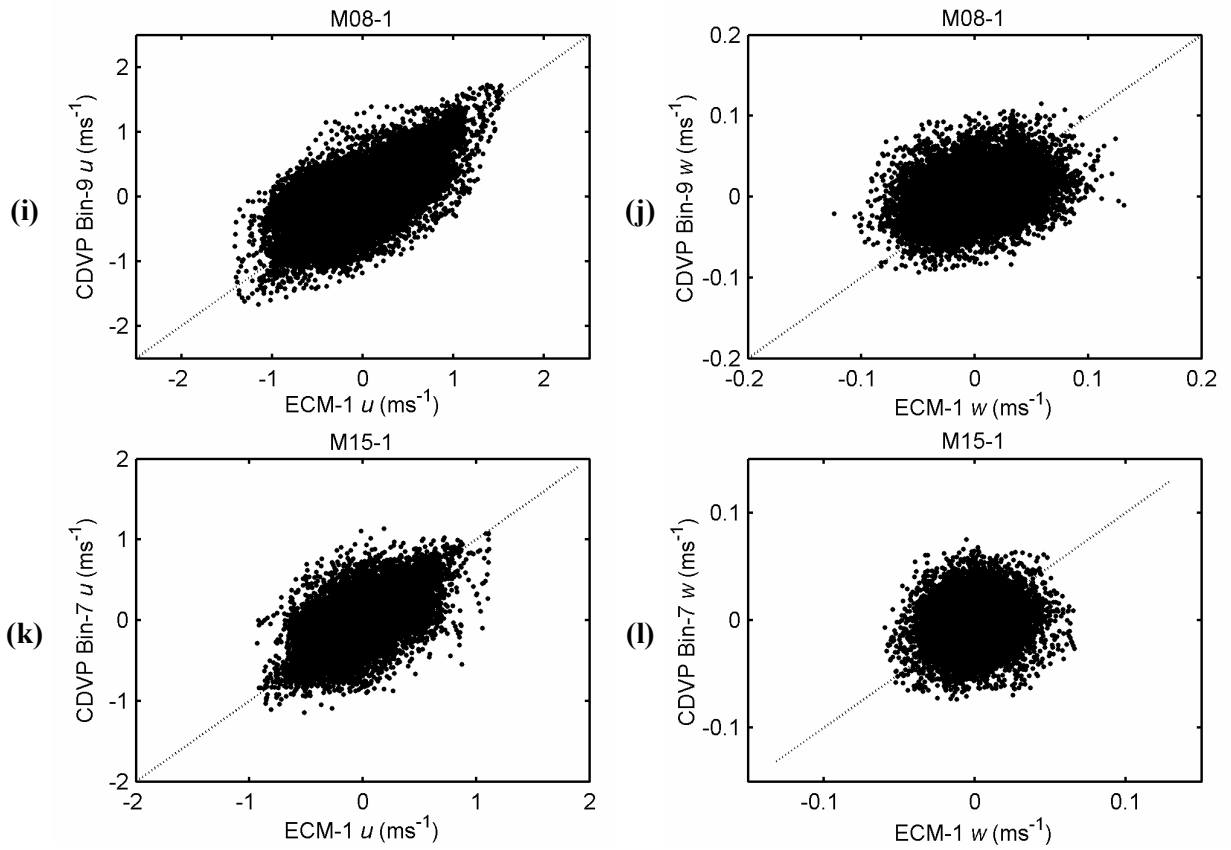


Figure 21 – Comparison between CDVP and ECM-1 recorded velocities for (i) M08-1 u , (j) M08-1 w , (k) M15-1 u , and (l) M15-1 w . The dashed line in each plot shows the theoretical 1:1 line.

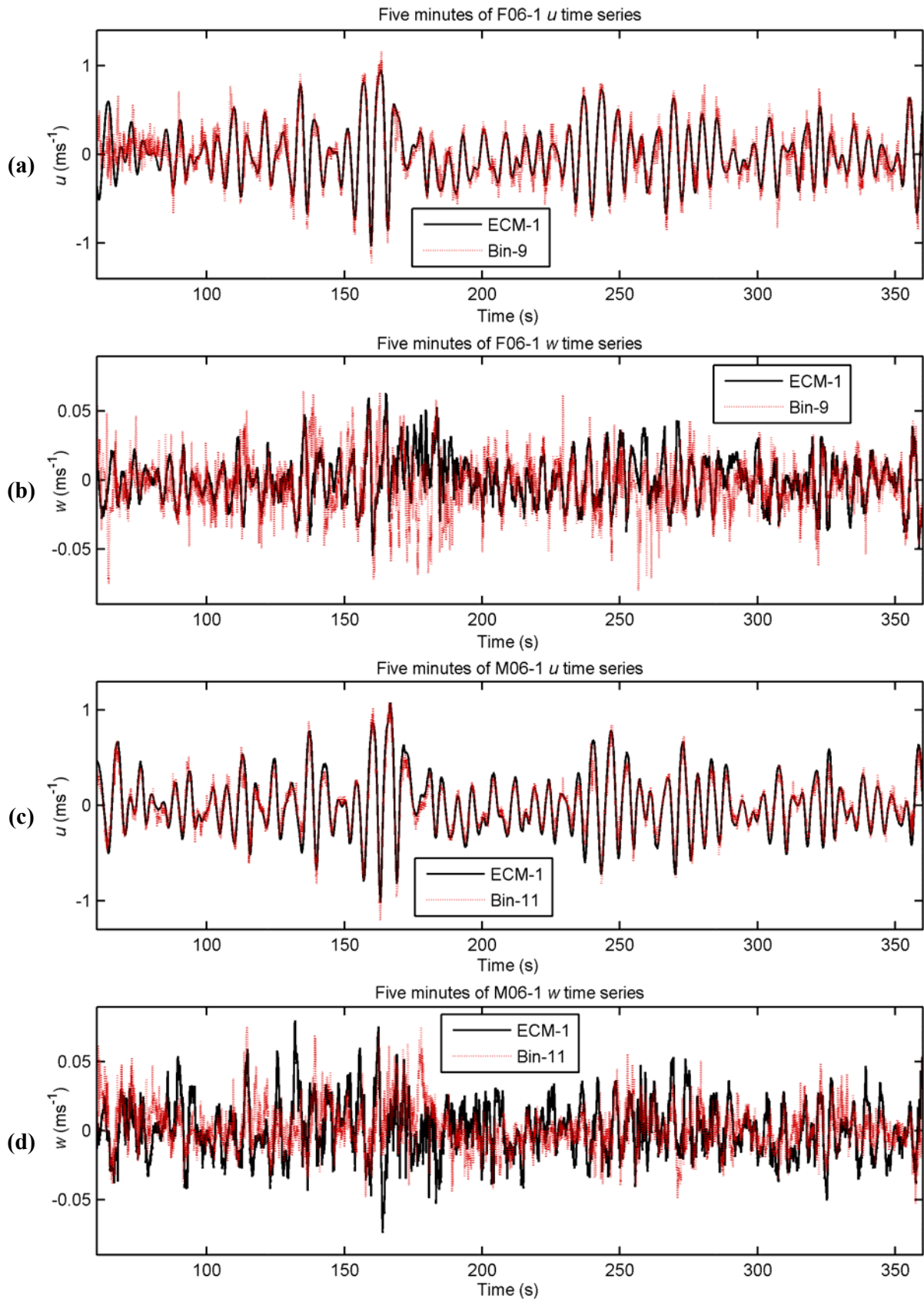


Figure 22 – Comparison between CDVP and ECM-1 derived time series for (a) F06-1 u , (b) F06-1 w , (c) M06-1 u and (d) M06-1 w .

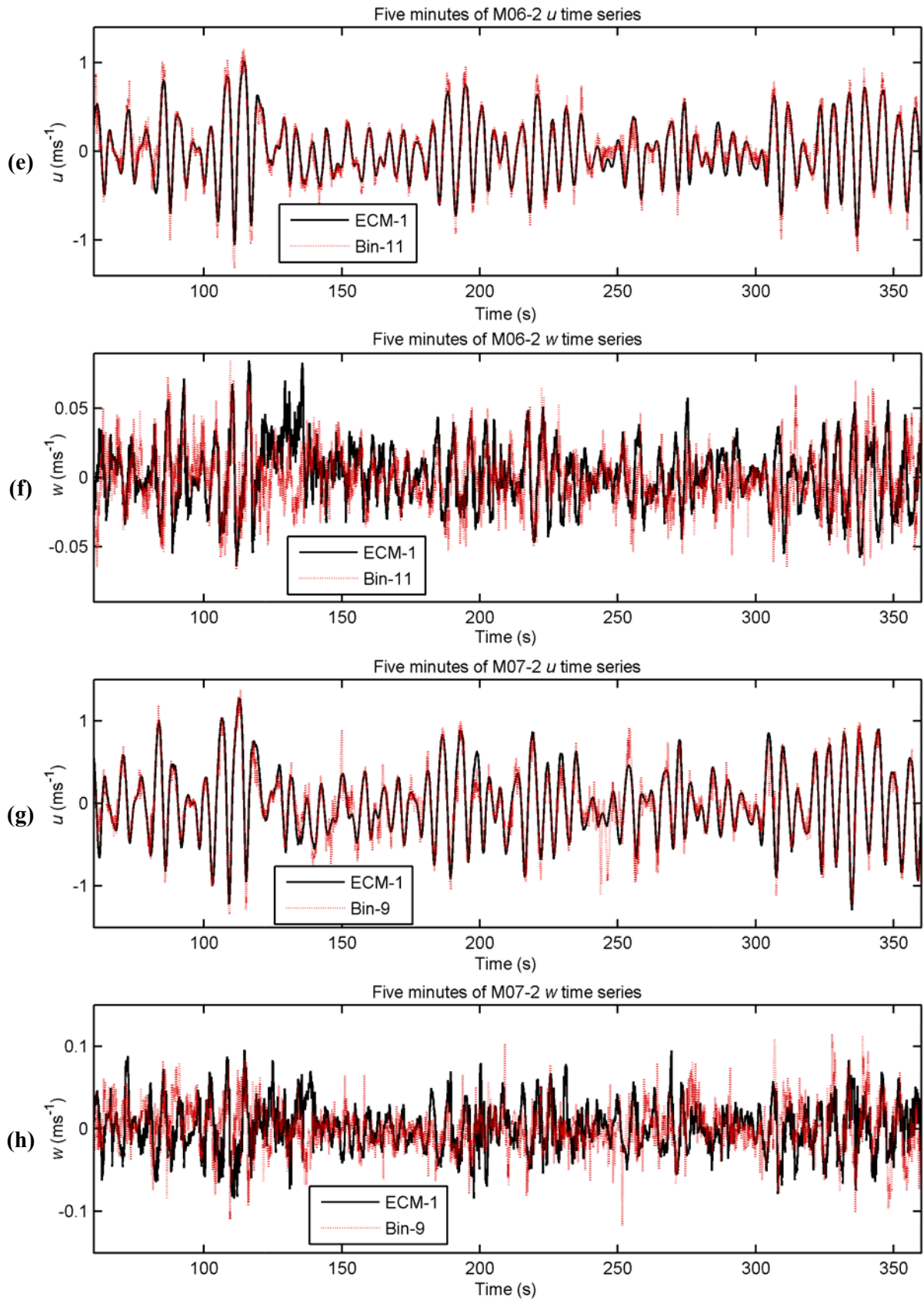


Figure 22 – Comparison between CDVP and ECM-1 derived time series for (e) M06-2 u , (f) M06-2 w , (g) M07-2 u and (h) M07-2 w .

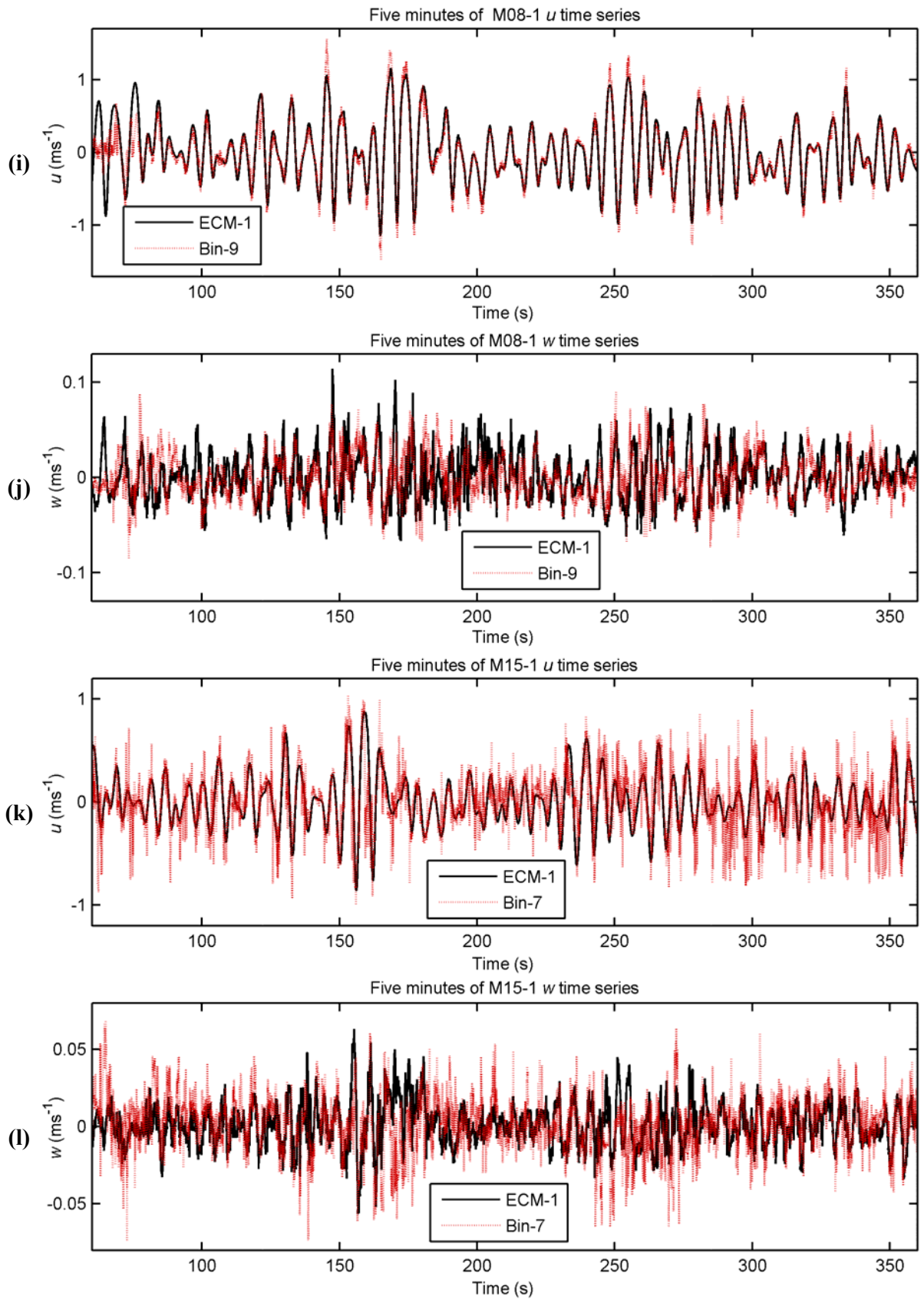


Figure 22 – Comparison between CDVP and ECM-1 derived time series for (i) M08-1 u , (j) M08-1 w , (k) M15-1 u and (l) M15-1 w .

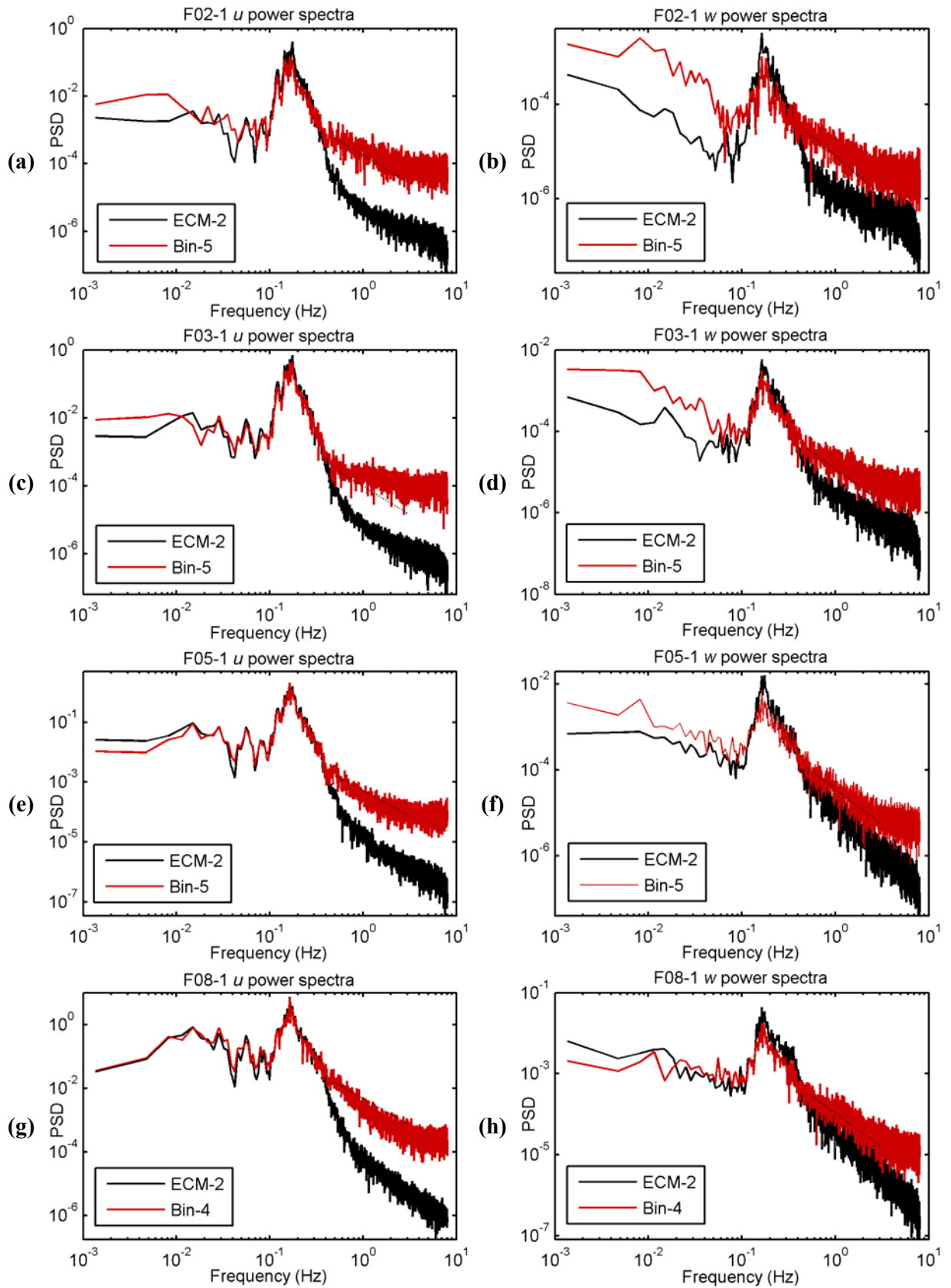


Figure 23 – Comparison between CDVP and ECM-2 derived power spectra for (a) F02-1 u , (b) F02-1 w , (c) F03-1 u , (d) F03-1 w , (e) F05-1 u , (f) F05-1 w , (g) F08-1 u , and (h) F08-1 w . The dashed line in each plot depicts $f^{5/3}$.

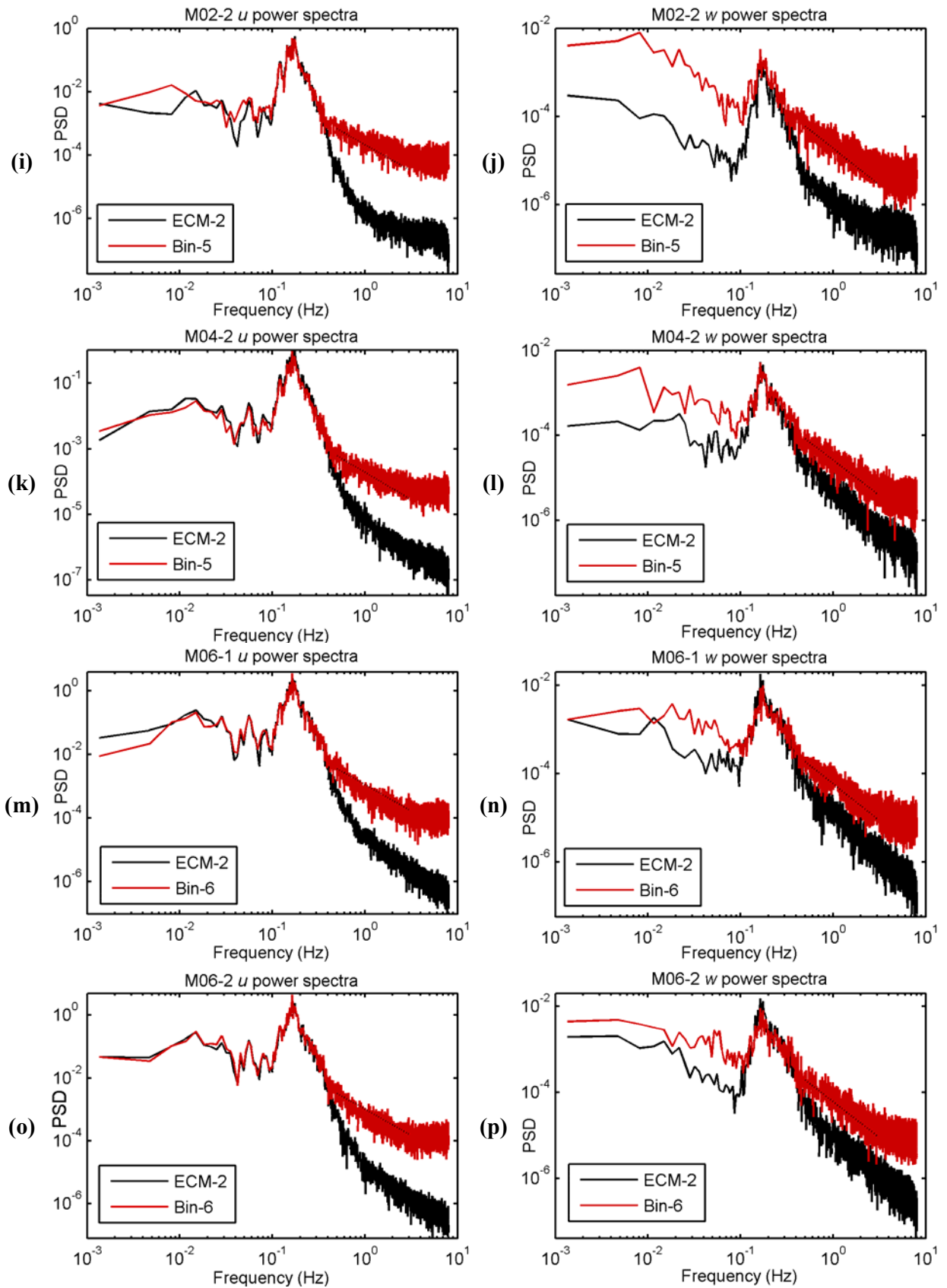


Figure 23 – Comparison between CDVP and ECM-2 derived power spectra for (i) M02-2 u , (j) M02-2 w , (k) M04-2 u , (l) M04-2 w , (m) M06-1 u , (n) M06-1 w , (o) M06-2 u , and (p) M06-2 w . The dashed line in each plot depicts $f^{-5/3}$.

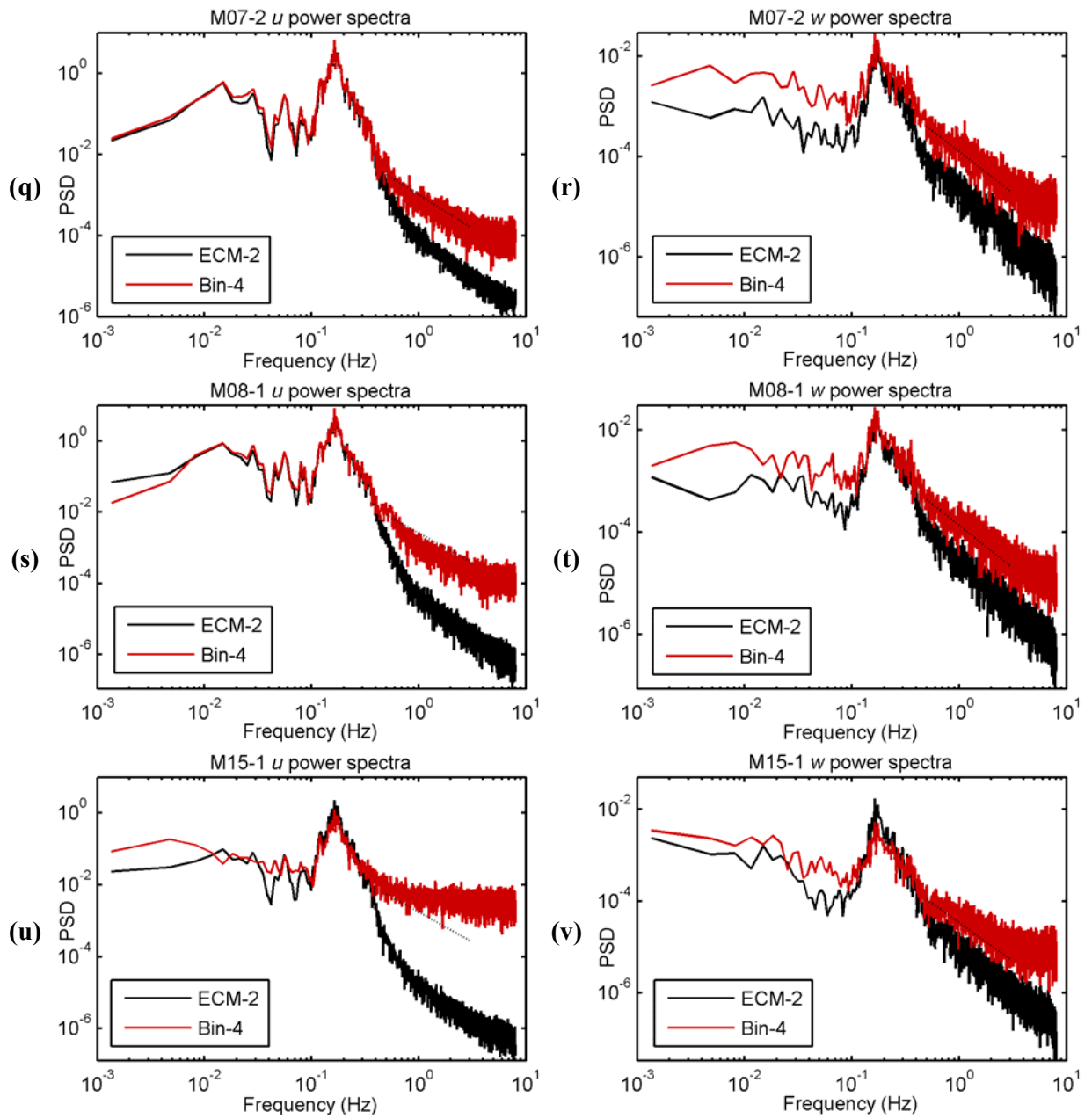


Figure 23 – Comparison between CDVP and ECM-2 derived power spectra for (q) M07-2 u , (r) M07-2 w , (s) M08-1 u , (t) M08-1 w , (u) M15-1 u , and (v) M15-1 w . The dashed line in each plot depicts $f^{5/3}$.

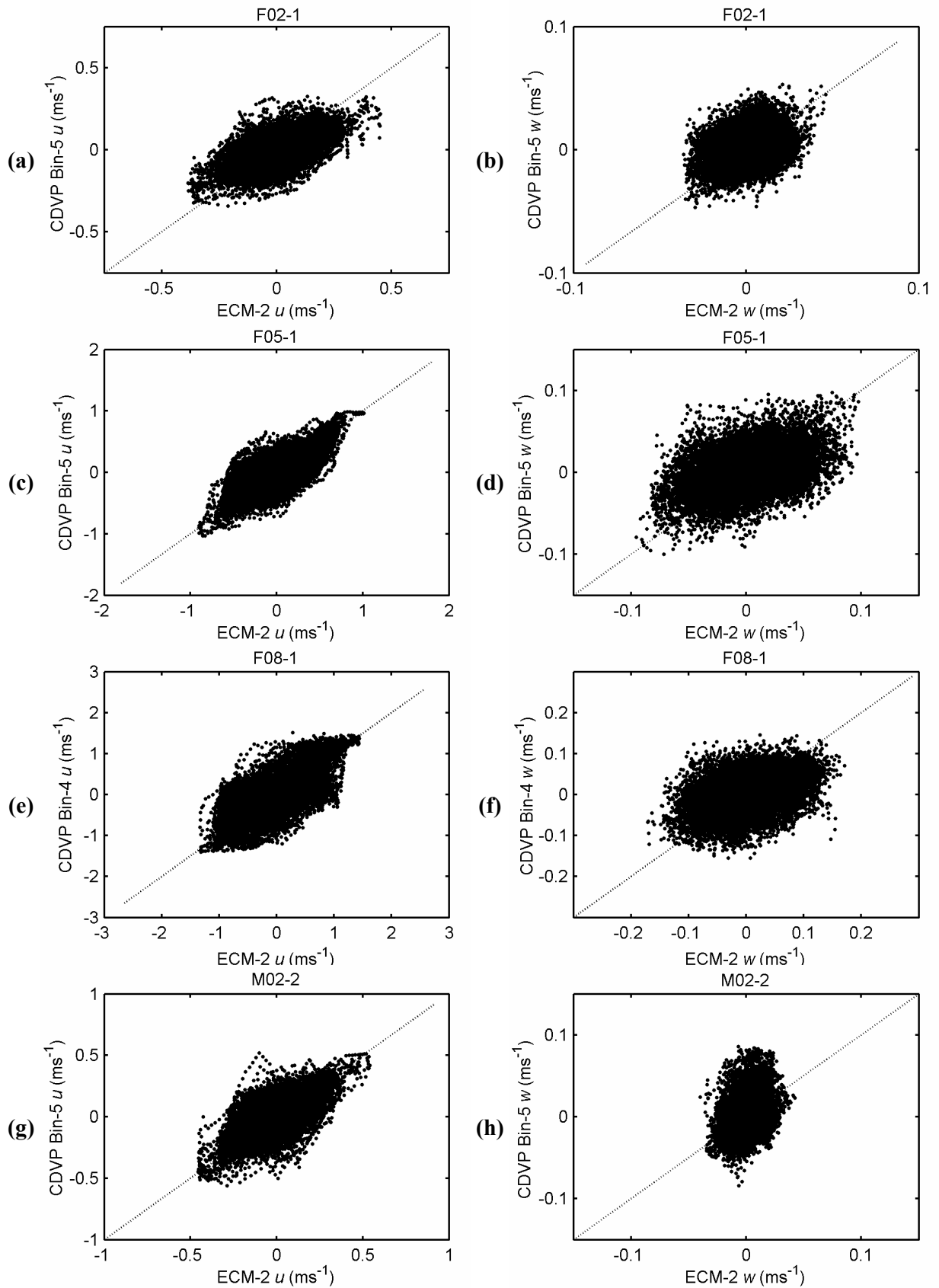


Figure 24 – Comparison between CDVP and ECM-2 recorded velocities for (a) F02-1 u , (b) F02-1 w , (c) F05-1 u , (d) F05-1 w , (e) F08-1 u , (f) F08-1 w , (g) M02-2 u , and (h) M02-2 w . The dashed line in each plot shows the theoretical 1:1 line.

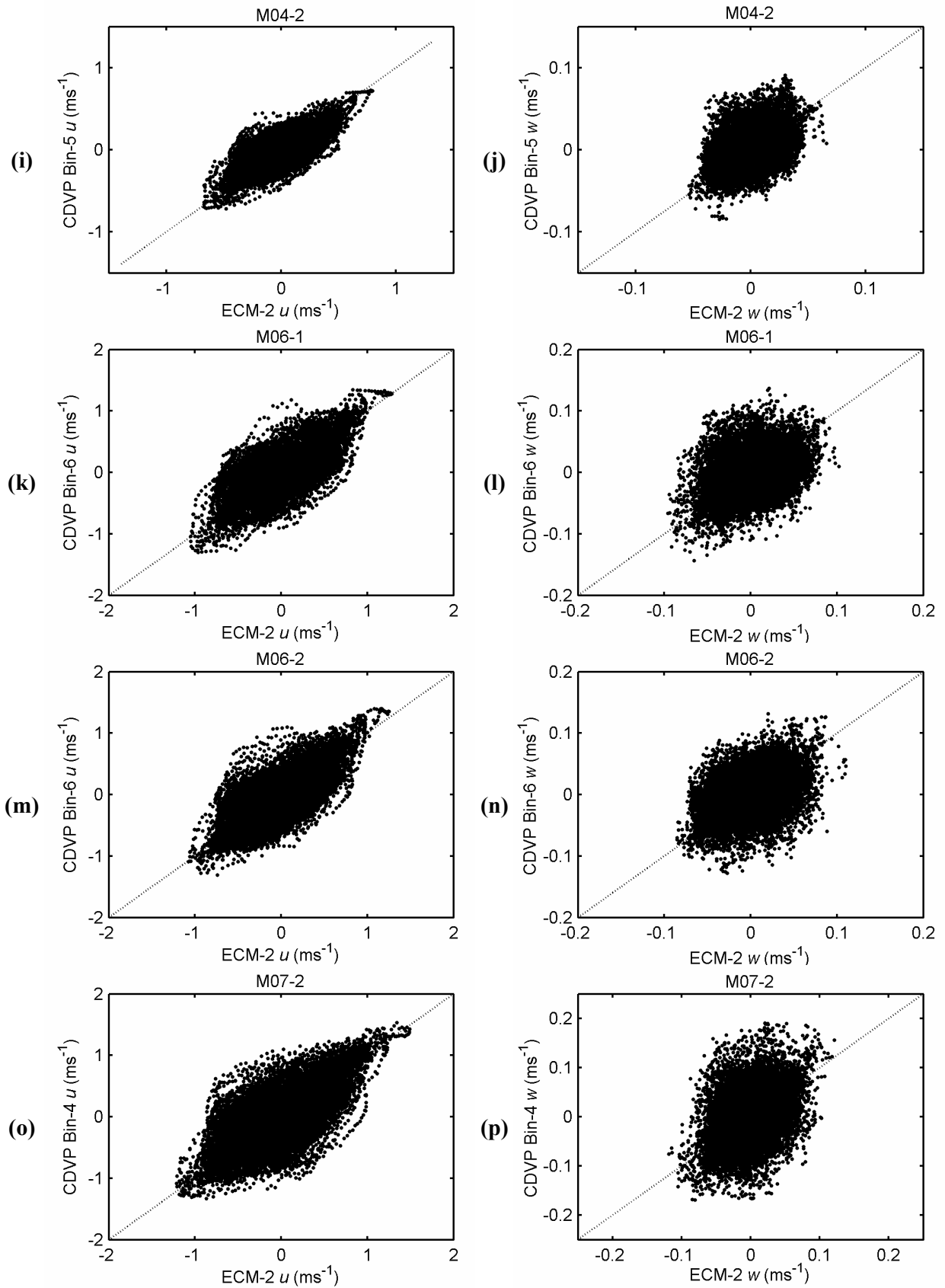


Figure 24 – Comparison between CDVP and ECM-2 recorded velocities for (i) M04-2 u , (j) M04-2 w , (k) M06-1 u , (l) M06-1 w , (m) M06-2 u , (n) M06-2 w , (o) M07-2 u , and (p) M07-2 w . The dashed line in each plot shows the theoretical 1:1 line.

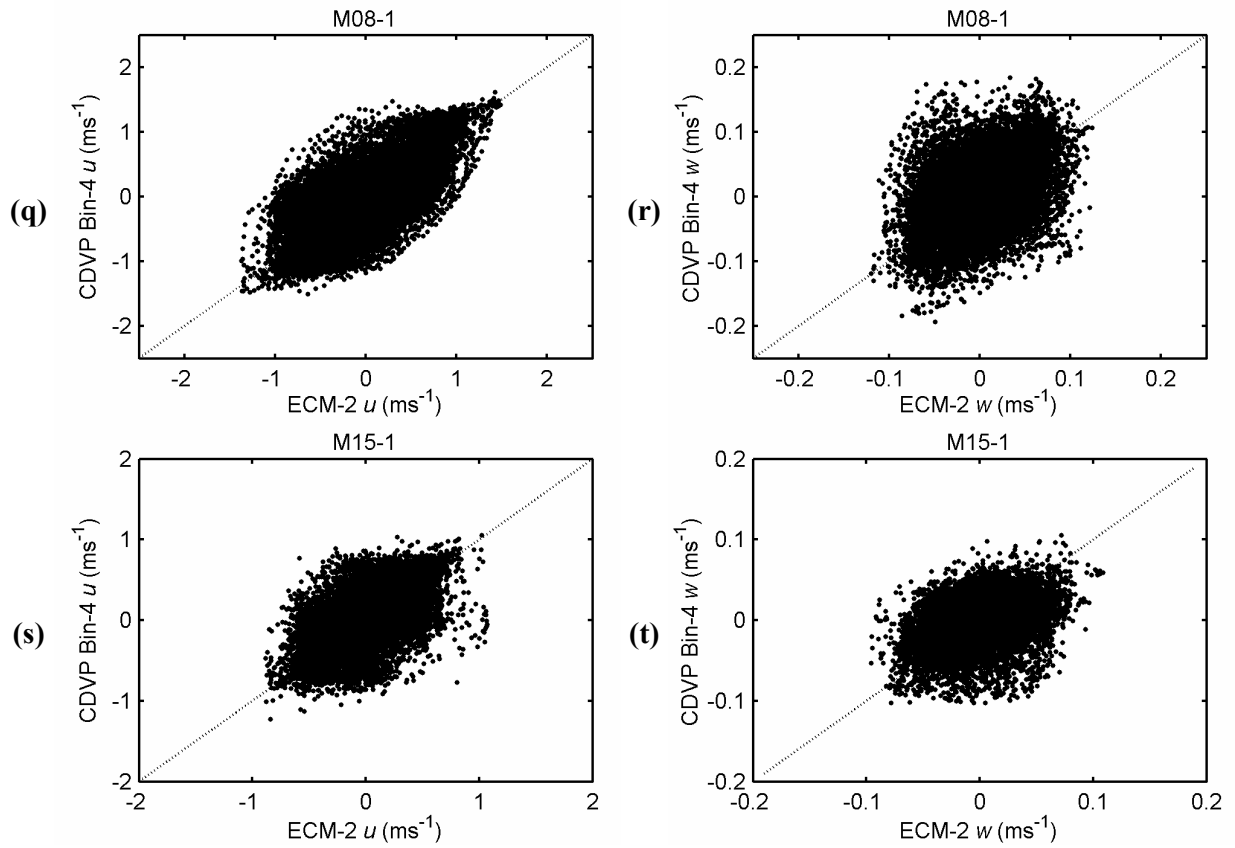


Figure 24 – Comparison between CDVP and ECM-2 recorded velocities for (q) M08-1 u , (r) M08-1 w , (s) M15-1 u , and (t) M15-1 w . The dashed line in each plot shows the theoretical 1:1 line.

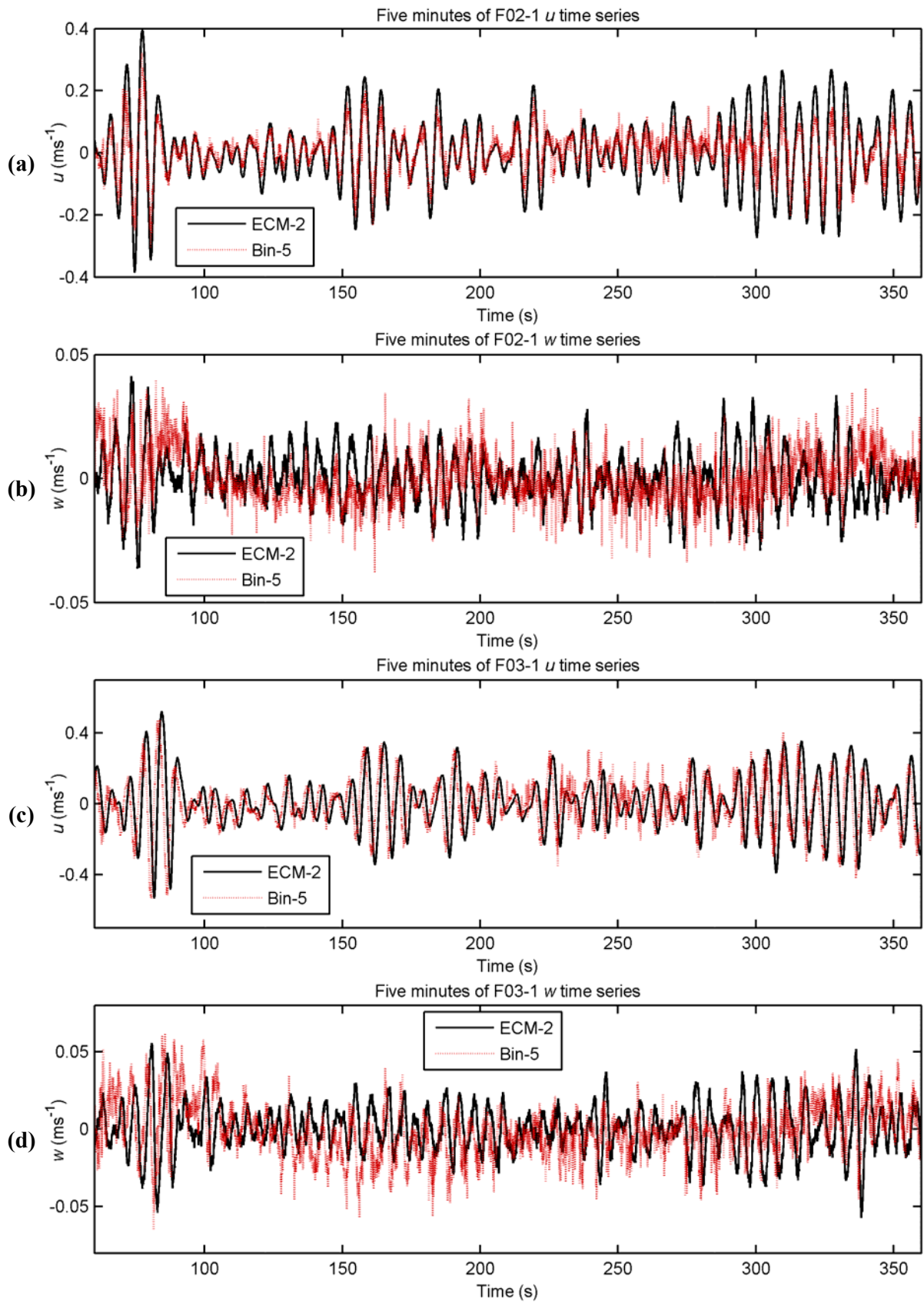


Figure 25 – Comparison between CDVP and ECM-2 derived time series for (a) F02-1 u , (b) F02-1 w , (c) F03-1 u and (d) F03-1 w .

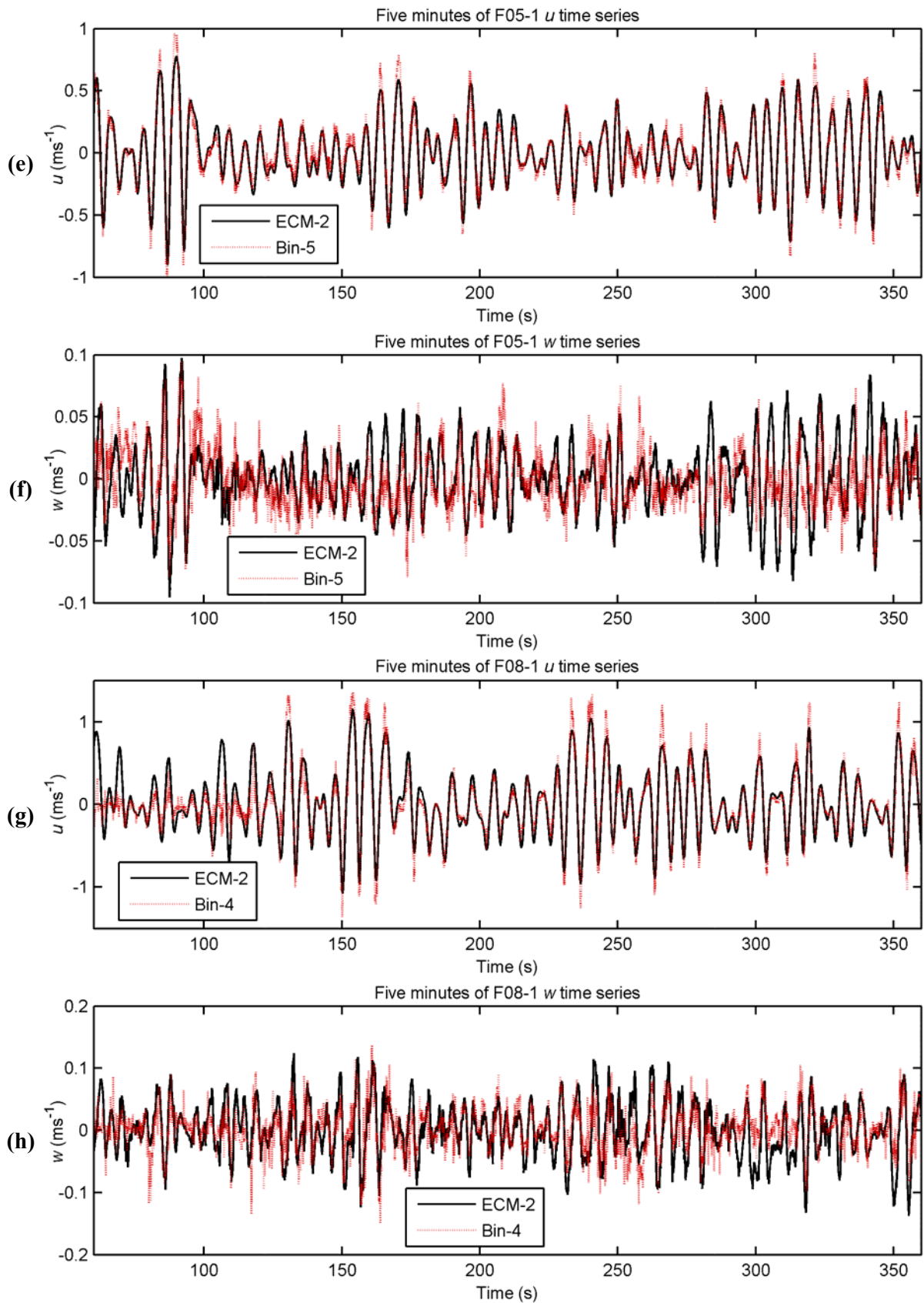


Figure 25 – Comparison between CDVP and ECM-2 derived time series for (e) F05-1 u , (f) F05-1 w , (g) F08-1 u and (h) F08-1 w .

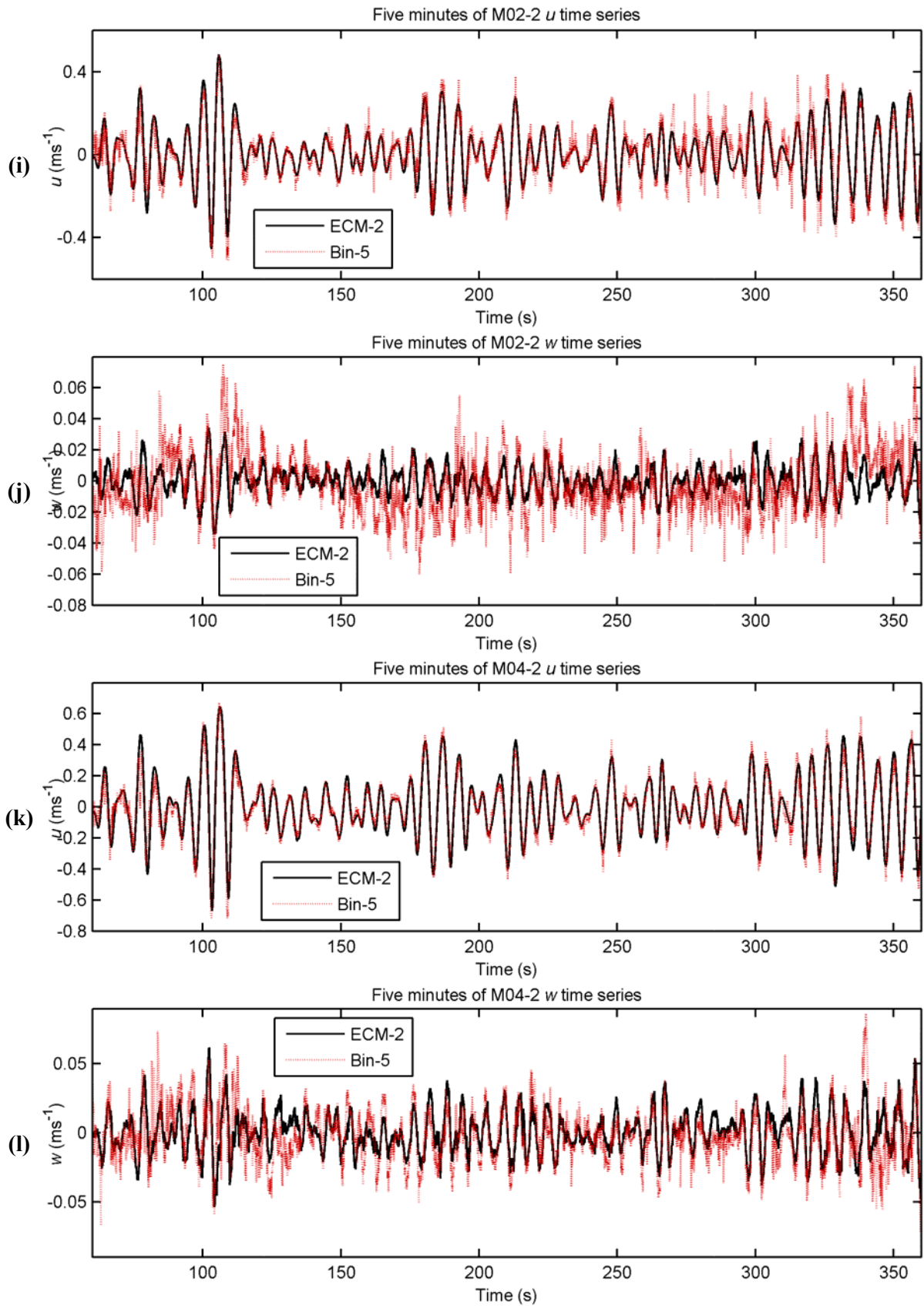


Figure 25 – Comparison between CDVP and ECM-2 derived time series for (i) M02-2 u , (j) M02-2 w , (k) M04-2 u and (l) M04-2 w .

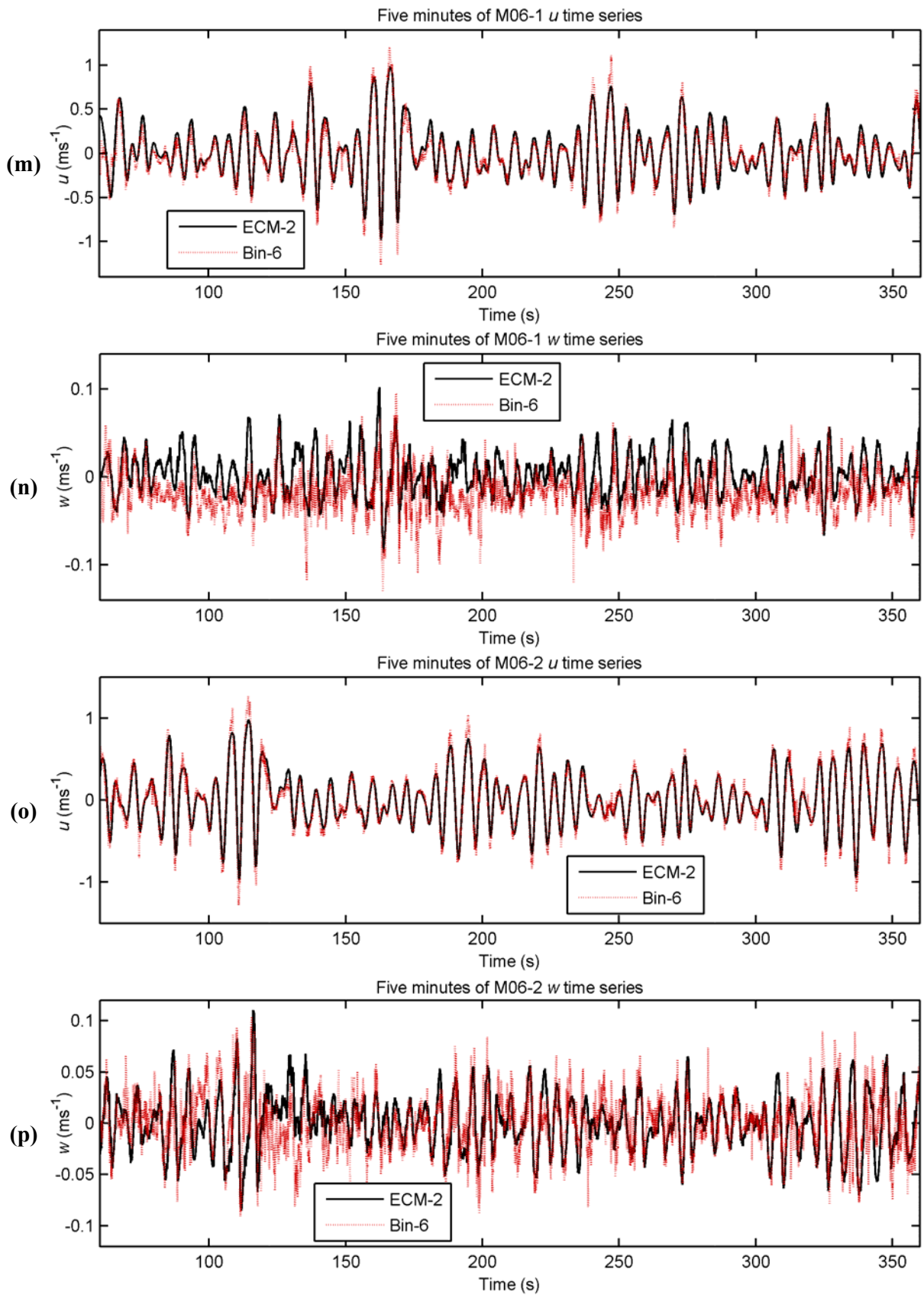


Figure 25 – Comparison between CDVP and ECM-2 derived time series for (m) M06-1 u , (n) M06-1 w , (o) M06-2 u and (p) M06-2 w .

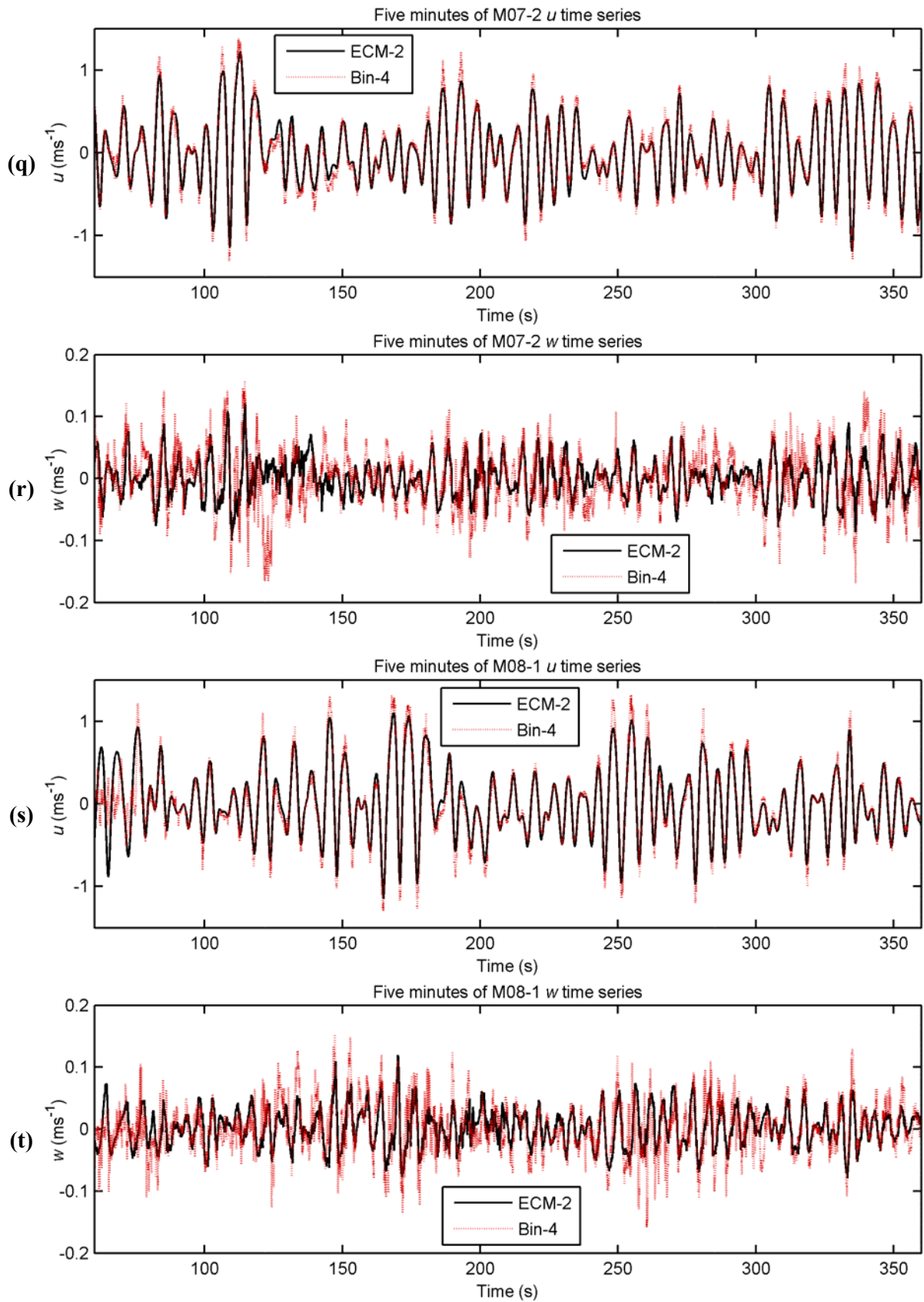


Figure 25 – Comparison between CDVP and ECM-2 derived time series for (q) M07-2 u , (r) M07-2 w , (s) M08-1 u and (t) M08-1 w .

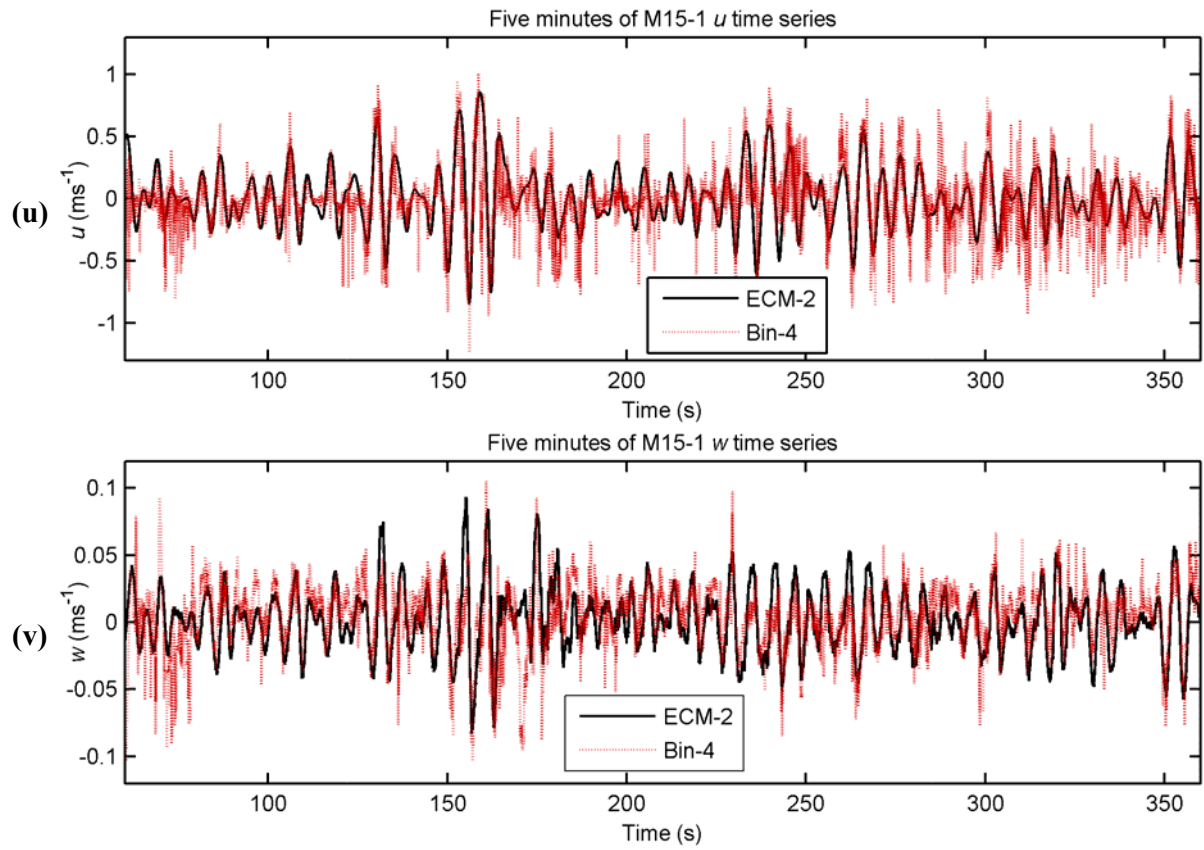


Figure 25 – Comparison between CDVP and ECM-2 derived time series for (u) M15-1 u , and (v) M15-1 w .

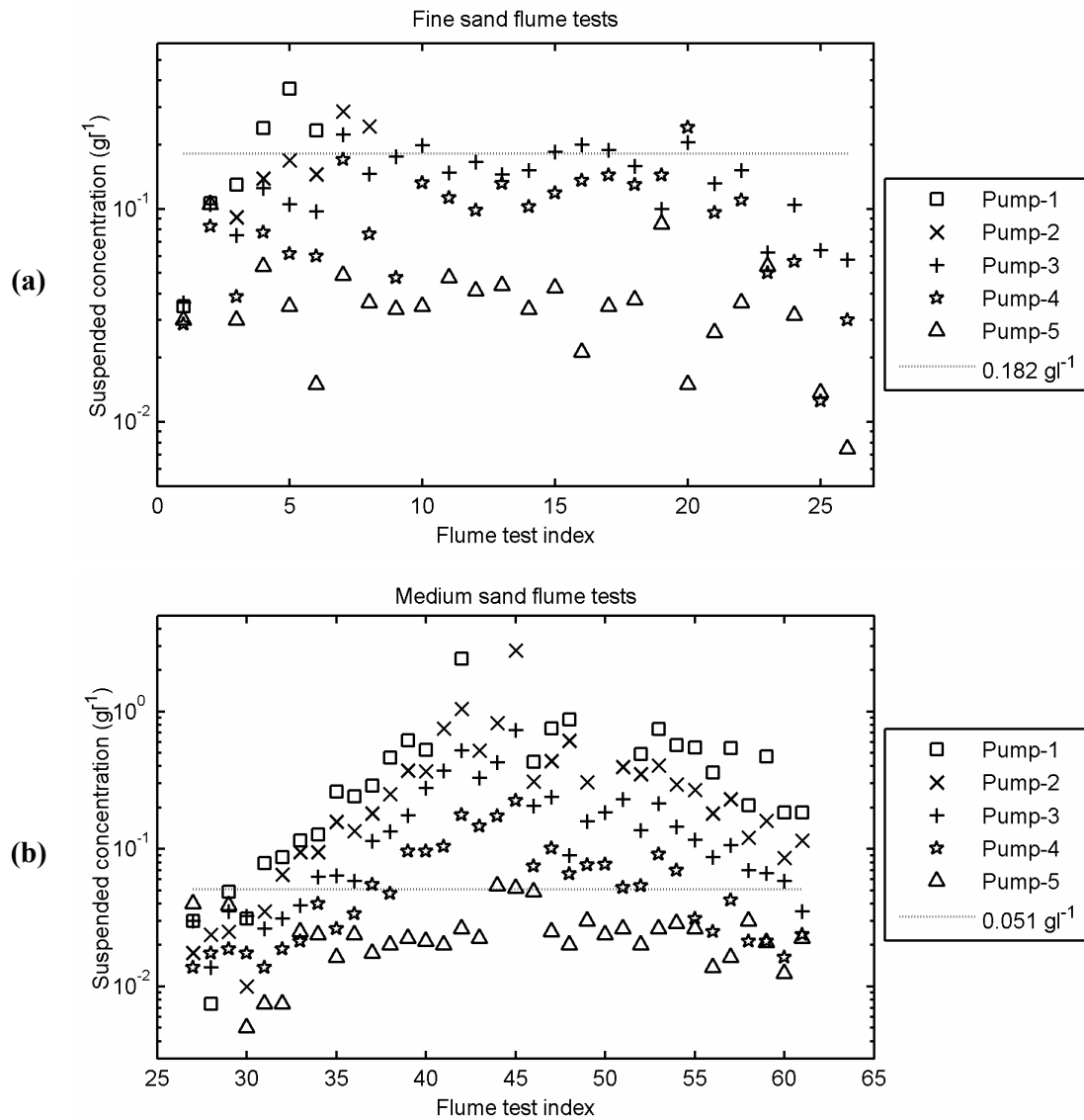


Figure 26 – Variation of suspended particulate matter concentrations with flume test index (defined in Table 5) for (a) fine sand flume tests, and (b) medium sand flume tests. The dashed line in each plot shows the concentration limits required for the CDVP to accurately measure velocities according to Equation 17. Missing pump samples were due to pump nozzles being located within the bed, or due to no sample being collected.